Università degli Studi di Padova

Dipartimento di Astronomia
DOTTORATO DI RICERCA IN ASTRONOMIA
CICLO XX

SEMI-ANALYTICAL MODELS OF GALAXY FORMATION AND COMPARISON WITH OBSERVATIONS

Coordinatore: Ch.mo Prof. Gianpaolo Piotto
Supervisore: Ch.mo Prof. Alberto Franceschini

Dottorando: Elena Ricciardelli

DATA CONSEGNA TESI: 31 luglio 2008

Riassunto

In questa Tesi abbiamo cercato di dare risposta ad alcune fondamentali domande riguardanti l'evoluzione delle galassie. In particolare, quando e come le galassie hanno formato la loro massa attuale e come questo processo dipende dalla loro massa finale.

Al fine di affrontare questa fondamentale questione, abbiamo sviluppato un nuovo modello semi-analitico di formazione delle galassie (GECO, Galaxy Evolution COde). Il nostro modello e' suddiviso in un algoritmo Monte Carlo (MC) per la rappresentazione del merging gerarchico degli aloni di materia oscura e in un insieme di ricette analitiche per il trattamento della fisica barionica. Il merger tree MC e' basato sul formalismo della teoria Press-Schecter estesa (EPS), che permette di partizionare un alone a $z = 0$ in un certo numero di progenitori esistenti ad alto redshift, quindi con un procedimento che va indietro nel tempo. Diversamente, la formazione delle galassie e' modellata con un approccio che va avanti nel tempo, iniziando dagli aloni "foglia" del tree, vale a dire quegli aloni i cui progenitori cadono al di sotto di una certa massa di risoluzione scelta e la cui gerarchica non e' piu' seguita nel tempo. I barioni sono inseriti all'interno di questi aloni, in accordo con la frazione barionica osservata, e sono quindi soggetti a processi dissipativi. Abbiamo considerato il raffreddamento del gas, il processo di formazione stellare, attraverso il meccanismo quiescente e quello starburst, diversi modi di feedback o autoregolazione della formazione stellare (esplosioni di SN, fotoionizzazione, AGN) e, chiaramente, i merger tra galassie all'interno dello stesso alone.

I risultati del modello sono stati testati con osservazioni dell'universo locale. Diversamente da altri modelli di formazione delle galassie, abbiamo fissato i parametri liberi del modello confrontando osservabili riguardanti la massa stellare piuttosto che la luminositá, essendo infatti la massa un output diretto del codice. Il confronto a redshift zero ci mostra un alto livello di accordo con i dati. Il vincolo più forte e' dato dalla funzione di massa stellare. GECO predice il corretto numero di galassie in ogni intervallo di massa a $z = 0$ e anche l'abbondanza relativa di galassie ellittiche e spirali e' ben riprodotto. Allo stesso modo, la relazione tra la massa del buco nero centrale e quella del *bulge* e' in perfetto accordo con i dati.

Anche ad alto redshift le galassie del nostro modello evolvono in buon accordo con le osservazioni. La densitá di formazione stellare integrata mostra un alto tasso di formazione stellare ad alto redshift, un picco a $z \sim 1.5 - 3$ e poi un drastico declino, come osservato. Ugualmente, l'assemblaggio di massa e' avvenuto molto rapidamente in epoche primordiali ed e' poi rallentato in epoche piú recenti. Studiando la formazione stellare e l'assemblaggio in funzione della massa, si osserva che i sistemi di massa maggiore formano il grosso delle loro stelle rapidamente ad alto redshift, mentre gli oggetti meno massivi continuano a formare stelle fino a basso redshift. Nonostante questo *downsizing* nella formazione stellare sia ben riprodotto nel modello, il *downsizing* nell'assemblaggio di massa risulta più difficile da riprodurre, almeno da un punto

di vista quantitativo. Infatti, sebbene il redshift di assemblaggio, vale a dire il redshift a cui metà della massa attuale è assemblata, sia in media più alto per gli oggetti di grande massa, il rapporto tra l'evoluzione della *faint-end* e quella della *bright-end* della funzione di massa stellare non è del tutto consistente con quanto osservato. Ulteriori sforzi sia verso una maggiore comprensione sul versante teorico, sia verso una maggiore attendibilità dei dati, soprattutto ad alto redshift, da un versante osservativo sembrano essere necessari.

Alcuni controlli sulla robustezza dei risultati del codice sono stati fatti usando differenti modelli ottenuti variando alcuni dei parameteri liberi dal modello fiduciale. La forma della funzione di massa stellare locale risulta essere molto sensibile alla scelta esatta di tali parametri. Ad ogni modo, i cammini evolutivi delle galassie e il relativo *downsizing* trovati nel modello fiduciale sono approssimativamente riprodotti in tutti gli altri modelli.

Infine, abbiamo affrontato un'altra questione fondamentale riguardante le proprietà delle galassie da un punto di vista osservativo. Abbiamo sfruttato il dataset fornito dalle *surveys* COSMOS/zCOSMOS per studiare la formazione della relazione colore-massa in funzione di redshift e ambiente. Abbiamo tovato che le galassie sono ben separate in una sequenza rossa e una blu fino al più alto redshift indagato, $z \sim 1$. Alcuni cambiamenti nella distribuzione dei colori delle galassie sono comunque osservati. La *faint-end* della sequenza rossa appare progressivamente popolata al crescere del tempo cosmico. Contemporaneamente, la pendenza della sequenza blu si appiattisce al diminuire del redshift. Abbiamo interpretato questi risultati in termini di un'evoluzione differenziale delle galassie con la massa stellare. Le galassie massive sono le prime ad abbandonare la sequenza blu e a raggiungere la sequenza rossa, in seguito all'esaurimento della formazione stellare, depauperando la parte alle alte masse della sequenza blu e popolando la sequenza rossa a masse progressivamente sempre più piccole. Dal momento che il colore misura il tasso di formazione stellare rispetto alla massa stellare totale in una certa galassia, sarà estremamente interessante, nell'immediato futuro, cercare di riprodurre la distribuzione dei colori delle galassie del modello, una volta che il codice sarà interfacciato a un modello di sintesi spettrofotometrica.

Abstract

In this Thesis we attempted to answer to some of the fundamental questions concerning galaxy evolution. In particular when and how galaxies got their present-day stellar content and how this process depends on their mass.

In order to address this key issues, we developed a new semi-analytic model of galaxy formation (GECO, Galaxy Evolution COde). Our model is divided into a Monte Carlo (MC) algorithm, for the representation of the merging hierarchy of DM haloes, and a set of analytical recipes for the treatment of baryonic physics. The MC merger tree is based on the Extended Press-Schecter (EPS) framework, which allows to split a given halo at $z = 0$ in a number of progenitors existing at higher redshift, through a backwards in time approach. On the contrary, galaxy formation is modelled forwards in time, starting from the "leaves" of the tree, namely those haloes whose progenitors fall below a certain mass resolution chosen and their hierarchy is no more followed. Baryons are put inside these haloes, according to the baryonic fraction observed, and then they are subject to dissipative processes. We consider the cooling of the gas, the star formation process, through a quiescent and a starburst mechanism, different kind of feedbak which regulate star formation (SN explosions, photoionization, AGN) and of course mergers between galaxies inside a common halo.

The model's results are tested against observations of the local universe. At variance with other models of galaxy formation, we set the free parameters of the model matching observables involving stellar mass more then luminosities, because mass is a direct output of the code. The zero-redshift comparison shows an high level of agreement with data. The strongest constraint comes from the local stellar mass function. GECO predicts the correct number of galaxies in each bin of masses at z=0, and even the relative abundance of early and late type systems is correctly recovered. As well, the relation between the bulge and the black-hole mass results in perfect agreement with data.

Even at high-redshift our modelled galaxies evolve in nice agreement with observations. The integrated star formation rate density shows an high level of star formation at high redshift, a peak at $z \sim 1.5 - 3$ and then a sharp decline, as observed. In the same way, the mass assembly has proceeded faster at early epochs, followed by a slow down at recent times. When the star formation and assembly processes are studied as a function of the mass, it is observed that high mass systems formed the bulk of their stars at a fast rate at high redshift, while less mass objects continue to form stars down to lower redshift. Although this *downsizing* in star formation is well recovered in the model, the *downsizing* in mass assembly resulted more difficult to be reproduced, at least from a quantitative point of view. Although the redshift of assembly, namely the redshift when the galaxy has assembled half of its present-day stellar mass, on average is higher for high mass systems, the ratio between the evolution of the faint-end

and that of the bright-end of the mass function are not completely consistent with the observations. Major efforts in the improvement of both the understanding from a theoretical background, and of the reliability of observations, mainly at very high redshift, seem to be needed.

Some checks of the robustness of the results of the code are done using different models obtained from a variation of some of the free parameters from the fiducial model. The shape of the local stellar mass function results to be highly sensitive to the exact choice of the parameters. Anyway, the evolutionary paths of galaxies and its *downsizing* nature found in the fiducial model are roughly reproduced in all the other models.

Finally, we addressed another major issue of galaxy properties, that is the colour distribution of galaxies, from an observational point of view. We exploit the COSMOS/zCOSMOS data set, in order to study the build-up of the colour-mass relation with redshift and environment. We found that galaxies segregate in a red sequence (RS) and a blue one (BS) up to the highest redshift probed, namely $z \sim 1$. Nevertheless, some changes in the colour distribution of galaxies with redshift are observed. The faint-end of the red sequence appears to be increasingly populated as cosmic time increases. Simultaneously, the blue sequence slope flattens at low redshift. We interpret this findings in terms of a differential evolution of galaxies with stellar mass. High-mass galaxies are the first to leave the BS and to move to the RS, once their star formation stops, depauperating the high-mass end of the BS and populating the RS at progressively lower masses. Since colour measures the ratio of the present star formation rate over the total stellar mass in a given galaxy, it will be extremely interesting, in the next future, to try to recover the colour distribution of our modelled galaxies, once the code will be interfaced with a spectro-photometric model.

Contents

1

Observational Overview

In this chapter we review some basic results concernig galaxies in the nearby universe as well high redshift galaxies, such as stellar mass function, color-magnitude relations, star formation rates. We mainly focus on results which give strong constraints about the epoch at which galaxy formed and assembled their stars. Most of them point to the so called *downsizing* scenario of galaxy formation, which, as we want to show in this Thesis, can be fairly reproduced even in hierarchical models of galaxy formation.

1.1 Classification of galaxies

Following Hubble (1936), we still classify galaxies as ellipticals, spirals and irregulars according to their morphology. The Hubble morphological scheme is often called "tuning-fork diagram", and we can see one of its representations in Figure 1.1. Elliptical galaxies are arranged in a unique sequence on the left part of the diagram, while spirals are ordered in two branches on the right side, according to the precence or absence of bars in the disk. Lenticular galaxies form an intermediate class between ellipticals and spirals and lie at the bifurcation of the diagram.

The morphological classification, which is based on their external aspect, indeed well correlates with other global galaxy properties, such as colours and ages. Typical elliptical galaxies are redder than spirals and show purely absorption-line spectra with no or very weak emission-lines, typical of old stellar populations. For these reasons, it is common use to refer to ellipticals as early-type galaxies (ETG) and to spirals as late-type systems. Often, even the bulges of spirals are included under the same category of ellipticals, since they show very similar morphology and spectral features, and they are usually referred to as spheroids.

Beyond this general correlation, it is found that different sample selections do not always overlap. For example out of the morphologically-selected ETG, 70% satisfy also the color selection criteria, that is they have red colours, and 81% satisfy the

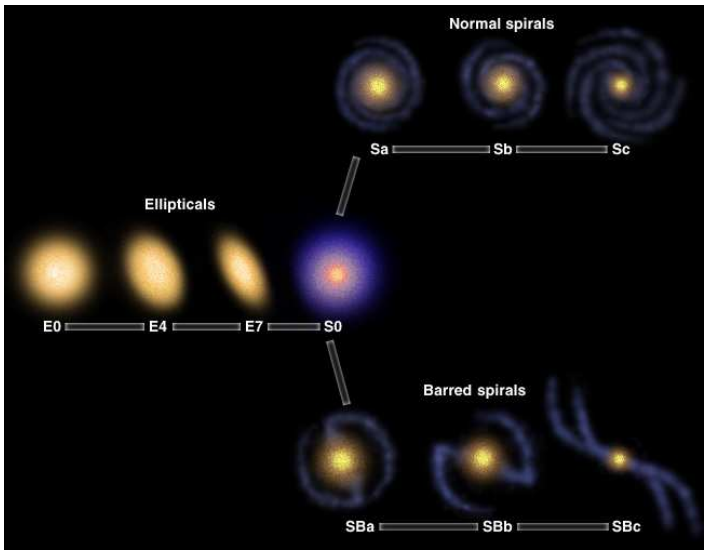

FIGURE 1.1— The tuning fork diagram devised by Hubble. The ellipticals are arranged in one branch while the spirals and the barred spirals form two parallel branches.The ellipticals are arranged in order of increasing ellipticity from left to right while the spirals and barred spirals become less tightly wound with smaller nuclei. The amount of interstellar dust in the galaxies increases from left to right in the diagram while the effect of rotation becomes more important. There is a S0 galaxy at the junction of the three arms of the diagram. S0 galaxies are disc-shaped like spirals but without the spiral structure and interstellar gas. They look like flat ellipticals.

spectral selection. On the contrary, among the colour-classified ellipticals, only 58% are still considered ETG in a morphology selection (Renzini, 2006). Even at higher redshift the correlation between color and morphological type holds, Bell et al. (2004) show that at $z \sim 0.7$ about 85% of red galaxies are also morphologically early-type.

1.2 Local observations

Even if observations at high redshift are the most direct way to look at galaxies during their formation process, galaxies at these redshifts are very faint and only a few of their properties can be directly observed. Galaxies in the local universe can instead be studied in much greater detail, and they can not only provide the basis for comparison with high redshift galaxies, but can also provide fossil evidence, that is the result of the integrated past star formation activity. For this reason we will first discuss observations in the nearby universe, and then high-redshift galaxies will be analysed on the basis of these findings.

1.2.1 Stellar mass function

Tha stellar mass function is a fundamental tool used in interperting the evolution of galaxies. It is usually defined as the number density of galaxies per logarithmic mass interval. In Figure 1.2 we show a comparison between published stellar mass func-

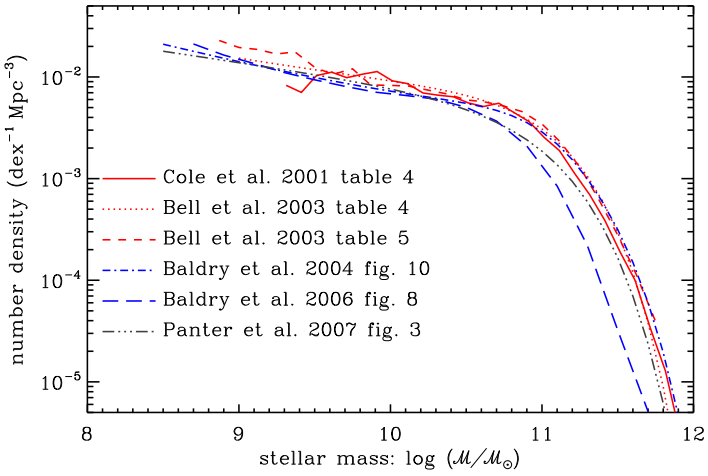

FIGURE 1.2— Comparison between different published local galaxy stellar mass function ($z \leq 0.1$). Taken from Baldry et al. (2008).

tions. Except for the Baldry et al. (2006) stellar mass function, that is shifted by about 0.2 dex, because it underestimates the mass of luminous red galaxies, the agreement among this recent determinations of the mass function is encouraging. It is observed to have a flatten faint-end slope and an exponential cut-off at high masses, and is often modelled with a Schechter function, even if recent results claim that it can be only fitted with a double Schechter function, because of a low-mass upturn (Baldry et al. 2008; Pozzetti et al. 2008).

It is now widely accepted that the majority of stars belong to spheroids: about 75% of the total mass in stars in the local universe is in spheroids and the remaining 25% is in disks. Although they dominate the mass content, they are quite rare compared to the late-type galaxies, as it is shown by the comparison of the mass functions of the two components. In Figure 1.3 it is shown the mass function from Baldry et al. (2004) of early-type (red crosses in the figure) and late-type (blue squares) populations, selected according to a color selection criterion, for Sloan Digital Sky Survey (SDSS hereafter) data. The authors defined an optimal color divider on the *u*-*r* vs. *r* color-magnitude diagram which varies from about 2.3 at bright magnitudes to 1.8 at the faint-end. Their findings show that at the bright-end red sequence galaxies dominate the mass function: at masses above the transition mass $\sim 3\times10^{10}M_\odot$, they start to outnumber blue galaxies by a factor that exceed 10 above $\sim 3\times10^{11}M_\odot$. On the contrary, the red distribution has a shallower faint-end slope than the blue distribution. Hence blue galaxies dominate the mass function at low masses and red galaxies dominate the bright end of the mass function. The transition mass, observed here, is close to the transition in galaxy properties noted by Kauffmann et al. (2003) and it is not only related to a change in dominance from the blue to the red distribution but also to a change in the properties of the red and blue distribution separately. Related results have been found dividing

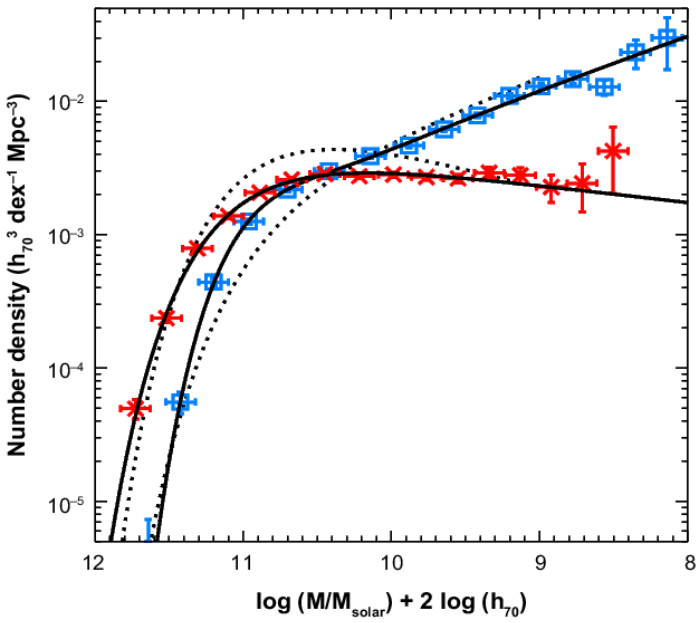

FIGURE 1.3— Mass function of local early-type (red crosses) and late-type (blue squares). The solid lines represent the best fit Schechter function to these data, while dotted lines are the Shecter mass functions of Bell et al. 2003. Taken from Baldry et al. 2004.

galaxies into classes according to different criteria (Madgwick et al. 2002; Blanton et al. 2001)

The dominance of early-type galaxies in the mass content is highlighted in Figure 1.4. It shows the contribution to the total stellar mass and to the number of galaxies by the two populations of galaxies defined as above. While ETG represent only 17% of galaxies in the sample, they contribute $\sim$ 57% of the total mass, and $>$ 80% of the stellar mass in ETG belong to galaxies more massive than $\sim 3\times10^{10}M_{\odot}$. This mass, called transition mass, also marks a sharp transition in several physical properties of galaxies: galaxies less massive than this mass show low surface mass densities, low concentration indices typical of disks and young stellar populations, while more massive systems have high surface mass densities, high concentration indices typical of bulges and old stellar populations (Kauffmann et al. 2003).

It is worth noting that the relative contribution from a given morphological type depends also on the environment where the galaxy lives, such as clusters of galaxies, which have a mass of $\sim 10^{14}-10^{15}M_{\odot}$, groups, with a mass of $\sim 10^{13}M_{\odot}$, and the field, where we find isolated galaxies. Early-type galaxies greatly dominate in high-density environments, such as cluster and groups of galaxies, while low-density environment are mainly populated by galaxies with a late-type morphology (see Chapter 6).

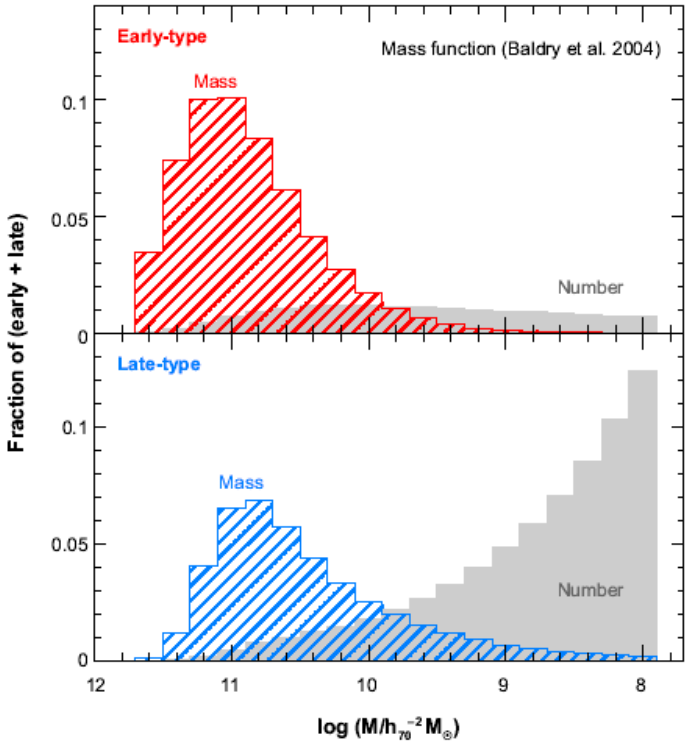

FIGURE 1.4— *Upper panel*: contribution to the total stellar mass (red, shaded area) and to the number (grey area) by early-type galaxies. *Lower panel*: the same but for late-type galaxies. The relative areas are proportional to the contribution of the early and late-type galaxies to the total stellar mass and to the number of galaxies. (From Renzini, 2006)

1.2.2 Galaxy bimodality

In recent years it has become clear that galaxies tend to segregate in a rest-frame optical colour-magnitude (CM) diagram. It is possible to distinguish two peaks in the color distribution separated by a shallow valley, as can be seen from Figure 1.5, taken from Baldry et al. (2004). Galaxies in the blue peak mainly belong to later morphological types and show a scattered but systematic variation of color with magnitude, in the sense that luminous galaxies tend to be somewhat less blue (Hogg et al. 2002). These color changes are due to changes in the mean ages, metallicities, and dust content of galaxies with luminosity, such that brighter galaxies tend to be older, dustier and more metal-rich. On the contrary, galaxies in the red peak are preferentially of the earlier types and form a tighten and well defined relationship between colour and magnitude, the so called red sequence (RS), such that brighter galaxies are typically redder. This RS is well established in overdense and cluster environment, where early-type are much more common (Dressler, 1980), but it is demonstrated to hold also in present-day field environment (Strateva et al 2001; Blanton et al. 2003; Baldry et al. 2004), although with considerably more scatter than in the cluster.

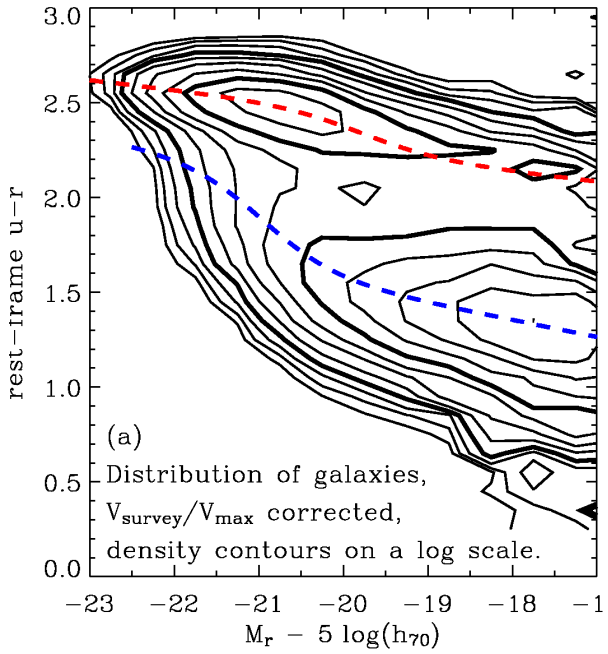

FIGURE 1.5— Rest-frame colour-magnitude relation. The contours are on a logarithmic scale in number density, doubling every two levels. The dashed lines represent the color-magnitude relations of the red and blue sequences. (From Baldry et al., 2004)

Even if it has been known qualitatively for some time that early and late type galaxies occupy different regions in the CM diagram, (Tully et al., 1982) it was only with the advent of large spectroscopic redshift surveys, such as the Sloan Digital Sky Survey in the local universe, that it is now possible to precisely quantify this colour bimodality as a function of absolute magnitude. The galaxy distribution in the CM plane can be modelled with the sum of two normal Gaussian function (Strateva et al., 2001), that is a *bimodal* function, from which the name bimodality, referring to the separation of galaxies into the red and the blue regions.

A bimodal division among the two populations is also seen in others parameters, such as spectral class (Madgwick et al., 2002, 2003), morphologies, metallicities and star formation rates (Kauffmann et al., 2003), but color is by far the easiest one to measure.

A natural explanation for the bimodality is that the two classes represent different populations of galaxies that are produced by two different set of processes. The widely accepted interpretation of the RS in galaxy clusters is that brighter red-sequence galaxies are more metal rich and that star formation in this objects happened and ceased early enough in cosmic time that the effect of possible spread in formation epoch are not detactable through broad band colors. The most convincing evidence in support of this interpretation is the redshift evolution of the red sequence, in fact its almost

constant slope with redshift shows directly that is not an age-mass sequence (Kodama et al., 1998). Galaxies in the blue cloud are more probably an eterogeneous population, whith a larger spread in age and dust extincion, giving rise to the larger scatter in colour observed.

1.2.3 Star Formation Histories

Even though high redshift observations are the most direct way to look at galaxies in their primeval stages, this kind of data naturally have lower quality and are more difficult to interpret. An alternative approach is the detailed investigation of stellar populations of nearby galaxies, studying the fossil evidence, the observables not related to the ongonig star formation but with the past star formation history of the galaxy. This is also called *archeolgical approach*, and allow us to achieve a view of galaxy formation and evolution fully complementary to that given by the study of high redshift galaxies. A commonly used diagnostic tool in this field is represented by the Lick system, a set of absorption-line indices, first introduced by Burnstein (1994), which, when compared with theoretical models, can provide a lot of useful informations about the distribution of stellar ages, metallicities and abundance ratios.

One of the major goal of this kind of approach is to constrain the formation epoch of early-type systems. A key-role is played by the α/Fe ratio. In fact the α elements are delivered by the explosion of Type II Supernovae of massive progenitors scale, while Iron mainly comes from the delayed explosion of Type Ia Supernovae, hence the α/Fe ratio is connected to the relative importance of SN II and SN Ia and can give fundamental informations about the timescale over which star formation occurs. A key study of the derivation of formation epoch of early-type galaxies as a function of their mass and environment was carried out by Thomas et al. (2005). They found a strong correlation between α/Fe and velocity dispersion. In particular they found that in less massive systems there is evidence for the precence of intemediate-age stellar population, while massive systems appear to be dominated by old stellar populations. Comparing elliptical systems in field and clusters they argue that in high-density environment star formation is delayed by 2 Gyr with respect to low density environment, with the bulk of star formation in cluster occuring between z=5 and z=2 and in the field between z=2 and z=1. This is illustrated in Figure 1.6, where smooth star formation histories are plotted as a function of mass for two environment. Note that this star formation histories have to be taken as probability distribution rather than the actual star formation activity of individual galaxies, which is likely to be much more bursty.

1.3 High-redshift galaxies

Observations of galaxies over a wide range of redshift allow us to compare their properities at different epochs in the history of the universe, in order to establish when and how galaxies become the systems that we know today, in particular understanding if galaxy formation is a steady process or if it took place more vigorously at some earlier epoch. In the last few years, many surveys, with high-quality data both from

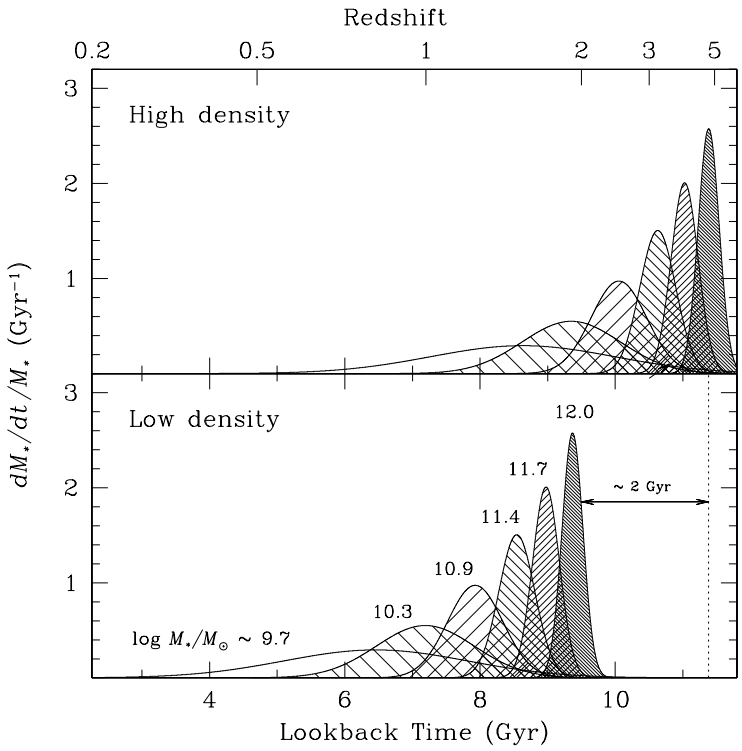

FIGURE 1.6— Star formation histories of early-type galaxies as a function of stellar mass for high density (*upper panel*) and low density (*lower panel*) environments. Taken from Thomas et al. (2005).

space and from ground-based telescopes at different wavelenghts, deeply spanned the redshift range from $z \sim 1$ to $z = 0$, and in some cases even beyond, that accounts for roughly half of the age of the universe. Clearly the combination of both pieace of information - local and high redshift observations - is what provide the most stringent conclusions.

1.3.1 Mass function evolution

One of the most direct way to constrain galaxy evolution is to derive luminosity and mass function from deep and unbiased surveys, tracing the volume density of galaxies as a function of mass and redshift. This has been done with both an UV-optical selection (Lilly et al. 1996; Madau and Pozzetti 2000) or with near-IR surveys, which are preferred for high-redshift studies because less affected by dust extinction and because the near-IR band are good indicators of the stellar mass content of galaxies. Several studies (Fontana et al. 2004; Franceschini et al. 2006 among others) found that the mass function at $z \sim 1$ shows little evolution compared with its local counterpart. Moreover the decline in number density with redshift is more significant for

lower mass galaxies ($M < 10^{11} M_{\odot}$), with the bright-end consistent with no evolution. In Figure 1.7 it is shown the Palomar-DEEP2 galaxy stellar mass function over $0.4 < z < 1.4$ by Bundy et al. (2006). It is clearly visible the bright-end already in place in the highest redshift bin. Galaxies are splitted into two populations according to their colors. A clear trend is observed in which the number density of massive blue galaxies declines with cosmic time, while red galaxies increasingly populate the faint end of the mass function, continuing dominating the brighter part of the mass function. The two populations seem to exchange members so that the total number density of galaxies at a given stellar mass keeps constant. The transitional mass, that is the mass above which passive galaxies dominate the number density, decreases with redshift.

Concerning the very high-redshift universe, very deep suveys have been exploited to describe the shape of the mass function at these early times (Drory et et al. 2005; Fontana et al. 2006). Berta at al. (2007), taking advantage of the shape of the near-IR spectral energy distribution (SED) of galaxies, identified high-z objects on the basis of IRAC (Infrared Array Camera onboard the Spitzer telescope) colours, where the $1.6\mu m$ stellar peak is redshifted at $z \sim 2 - 3$. They probe with unprecedented detail the massive tail of the mass function at these redshifts, finding a significant evolution, by a factor of 10, of the number density of these objects, having stellar masses of $10^{11} - 10^{12} M_{\odot}$. Moreover, the existence of such massive objects at very high redshift was already confirmed from several studies, with the identifications of massive and old galaxies at $z \gtrsim 2$ (Franx et al. 2003; Cimatti et al. 2004).

1.3.2 Evolution of the CM diagram

Several studies indicate that the bimodal nature of galaxies that we have seen to hold for nearby galaxies is already established up to $z \sim 1$ (Bell et al. 2004; Tanaka et al. 2005; Franzetti et al. 2006). Both red and blue sequence are fairly well visible up to this redshift. We show in figure 1.8 the colour-mass relation observed within the COSMOS survey, up to $z \sim 1$. We will discuss such investigation in Chapter 7. We plot points according to the density interval they belong to: blue for the highest density region, followed by red, magenta, green and then cyan for the less density bin.

There is some debate on a possible differential evolution of the red sequence, in the sense of a delayed formation of the faint red sequence with respect to the brighter end, which is clearly visible at $z = 1$. This is observed both in galaxy clusters (De Lucia et al. 2004 and 2007; Koyama et al. 2007), and in the field (Tanaka et al. 2005). Actually, even in figure 1.8, the faint-end appears to be in place only at the lowest redshift bins. We will discuss the related selection effects on Chapter 7. A likely scenario for this build-up is that blue galaxies settle to red sequence once they stop to form stars, and this truncation starts from massive galaxies and subsequently occurs for less massive systems as redshift decreases.

Galaxy bimodality is a strong function of mass, because massive galaxies tend to be early-type systems which lay on the red sequence, while less massive objects are preferentially late blue galaxies. It is interesting to ask if it is also a function of the en-

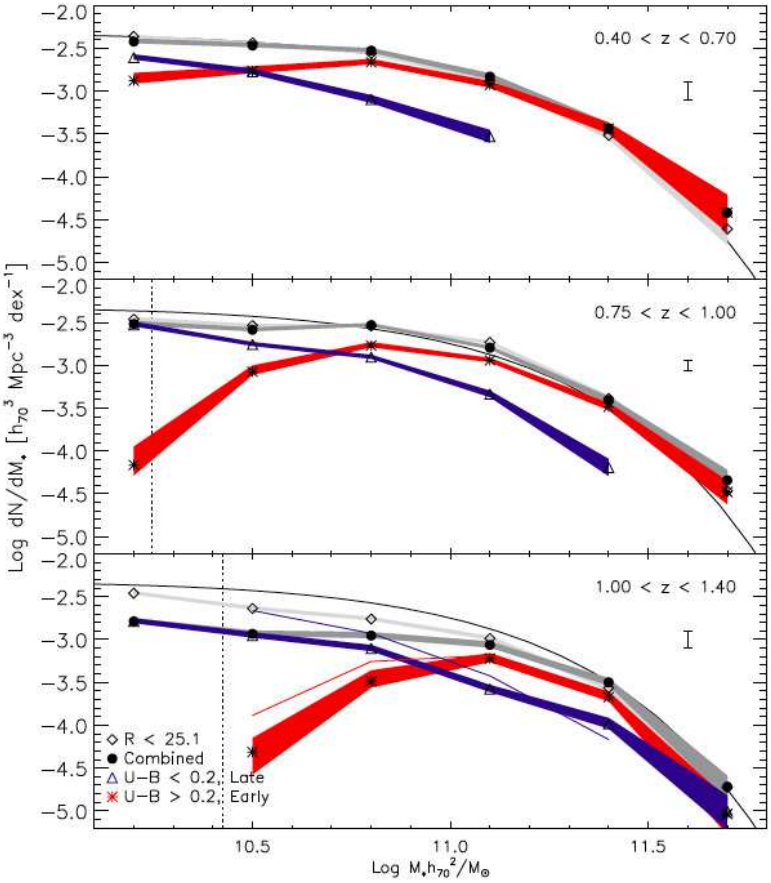

FIGURE 1.7— Stellar mass function in three redshift intervals. Grey shaded region shows the mass function for all galaxies. Red and blue shading indicates the mass functions for the population splitted according to the rest-frame U-B colour. The solid black curve in each panel is the Schechter fit to the mass function in the first redshift interval. Taken from Bundy et al. (2006).

vironment in which the galaxy lives. A bimodality is fairly seen in every environment, from field to cluster, but the two peaks of the distriubution are populated in a different way depending on the environment, with the red sequence becoming more evident in the highest density environment. This behaviour clearly reflects the morphology-density relation (Dressler, 1980), red ealry-type galaxies are preferentially located in high-density regions and blue late-type galaxies generally live in low-density environment. It is interesting to note that when the two morphological classes are taken separately, their color depends only weakly on the environmet (Cassata et al. 2007; Balogh et al. 2006), indicating the stellar mass as the main driver of galaxy evolution, more than the environment in which the galaxy lies.

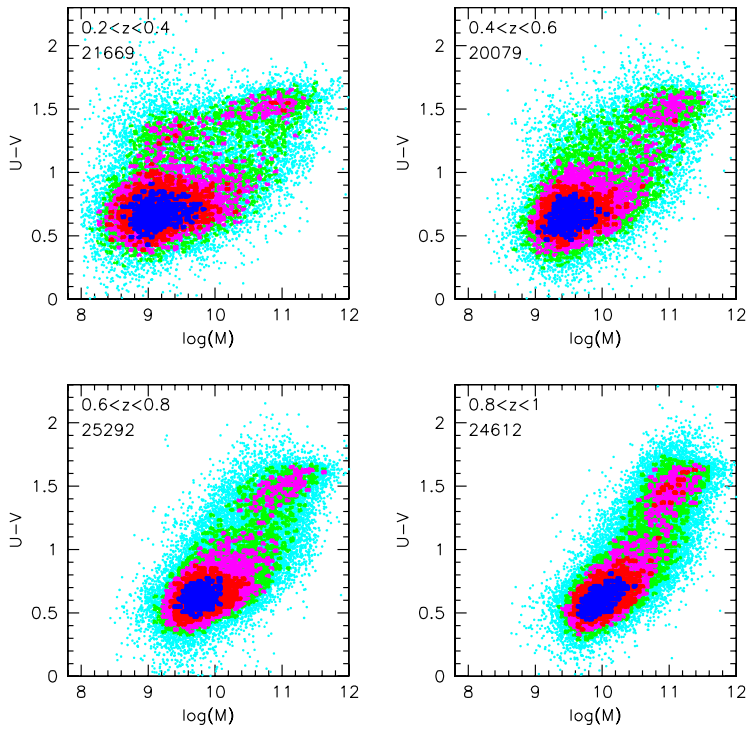

FIGURE 1.8— Rest-frame colour-mass relation observed in COSMOS for 4 redshift bin, ranging from $z = 0.2$ up to $z = 1$. Points are coloured according to the level in the number density they belong to. Further details are given in Chapter 7.

1.3.3 Star Formation Rate

The star formation rate per unit comoving volume as a function of redshift from observations extending from redshift zero to a redshift of about 4 was first compiled by Madau et al. (1996), and it is the Madau plot. It maps the history of star formation from a very early epoch, when galaxies were probably still forming until the present day. It is filled with data from different redshift surveys, using different selection techniques and SFR tracers (UV continuum, optical recombination lines, far-IR emission, submillimeter light). For all these reasons the calculation of a derived quantity, that is the star formation rate density, is not straighforward and has not always been consistent among different authors. Nevertheless, originally, with only few points in the diagram it was clearly visible that in the last 8 Gyr, the universe experienced a significantly decrease, of about a factor 10, in the star formation rate. The emerging picture was that the universe has experienced an enhanced phase of star formation in the past, peaked at $z \sim 1 - 2$, with a subsequent decline to the present time. Now the number of points in the diagram has greatly increased and the picture at low redshift ($z \leq 1$) is clearer,

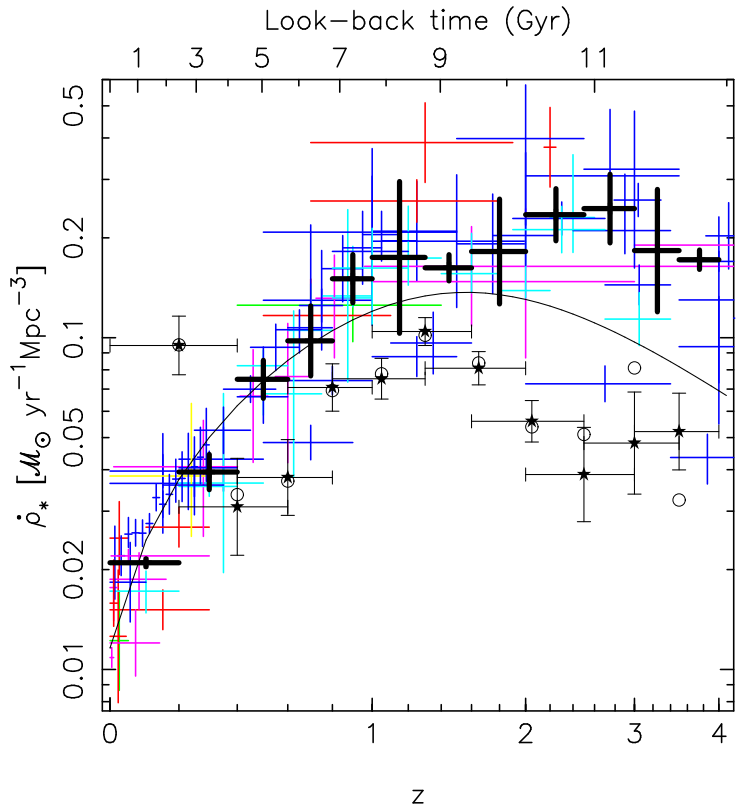

FIGURE 1.9— Evolution of the comoving SFR density of the universe. Different coloured point refers to different literature data from redshift surveys. The black line shows the SFR density evolution parametrized by Cole et al. (2001). Taken from Perez-Gonzalez et al (2008).

even if a factor of 2 in the scatter among different estimates still exists, while at $z \geq 1$ the uncertainties are still quite large. A recent compilation of the Madau plot was done by Perez-Gonzalez et al. (2008) and it is shown in Figure 1.9. The decrease in the star formation rate density by an order of magnitude between z=1 and the present time is clearly visible in spite of the differencies between different data. At higher redshift the uncertainties are larger, but seem to indicate an approximate constant value between $z \sim 1$ and $z \sim 4$.

1.4 Galaxy "Downsizing"

An interesting characteristic of the star formation process has emerged from the observations that we have described so far, and it is the anti-correlation between the stellar mass of a galaxy and its formation epoch, that is commonly referred to as *downsizing*. In other words this is simply the fact that elliptical galaxies consist of old stellar population and tend to be more massive, while disk galaxies contain younger populations and are on average less massive. The term *downsizing* was first used by Cowie

et al. (1996) in order to explain the characteristic pattern of star formation in which the sites of active star formation shifts from increasingly massive systems as cosmic time increases. Evidences of this differential evolution were also observed by Gavazzi et al. (1996) and Franceschini et al. (1998). Now the evidences for the *downsizing* of star formation activity are quite extensive. We already mentioned the behaviour of the quenching mass, the mass separating active star forming galaxies from passive ones, that moves towards lower masses as redshift decreases. The late build-up of the faint-end of the red sequence goes in the same direction, as the cosmic time increases, the mass of the objects which stop to form stars and rapidly move to the red sequence decreases. Another way to view this is through the measure of the evolution with redshift of the specific star formation rate (SSFR), the ratio between the star formation rate and the stellar mass. As demonstrated by several authors (e.g. Perez-Gonzalez et al. 2008), it increases continously moving to higher redshift, showing the top-down evolution of galaxies, where the most massive galaxies formed the bulk of their stars at high redshift, showing high values of the specific star formation that would correspond to double their stellar mass in a very short period of time. On the contrary less massive systems form their stellar content more slowly, presenting SSFR that would double their mass in timescales comparable with the look-back time of the universe at each redshift.

However, *downsizing* seems not to be limited to star formation, but the concept has to be extended even to mass assembly, as the build-up of most massive galaxies occurs before the one of smaller objects. At any redshift there is a characteristic mass above which the bright-end of the mass function is already in place (Cimatti et al., 2006), indeed the bright-end of the stellar mass function evolves very little in the range of redshift considered, as we already mentioned in the previuos section. Hence, massive galaxies are the first to form stars, but also the first to assemble their mass. The galaxy formation process appears to be divided into two major phases. A phase at very high redshift ($z > 2$) when the most massive objects that we find nowadays formed and assembled the bulk of their stellar content very rapidly, and a second phase at low redshift ($z < 1$), where the star formation process occurs in less massive systems, at slow rate.

Finally, we have discussed the evidence of *downsizing* in nearby elliptical galaxies, where the measure of absorption features lead to the conclusion that star formation in massive galaxies proceeds more rapidly than in less massive systems. It is worth to note that this last evidence in favour of *downsizing* is better referred to as *archeological downsizing*, which is to be interpreted in a slightly different manner. The analysis of present-day galaxies highlights the formation epoch of the majority of stars, which at least for ellipticals, form at high redshift, $z \geq 2$. In contrast, the *downsizing* envisaged from high redshift galaxies focuses on the early phases of star formation and may involve only a small fraction of stars (Neistein et al., 2006).

1.5 Galaxy Formation Scenarios

Theoretical formation scenarios are often grouped into two categories, broadly referred to as *monolithic collapse* and *hierarchical clustering formation*. In the first picture, the traditional one, early-type galaxies assembled their mass and formed their stars in a rapid event, of much shorter duration than their avarage age (Lynden-Bell & Sandage, 1962; Larson, 1975). According to this scenario, the process of galaxy formation took place at very high redshift and the evolution continued in a passive way. On the other hand, in the hierarchical scenario early-type galaxies formed by mergers of disk galaxies and the formation process happened at relatively recent times. According to this scheme, the formation process is continous: mass is accreted over time, and both major and minor mergers can trigger star formation that rejuvenates the stellar content of galaxies. There are a lot of observational evidences in favour of each scenario, both of them holding part of the truth. The dominant old stellar population of spheroids and their α-enhancement, together with the fact that they constitute a very homogeneous class, populating very tight color sequences and lying in a very tight fundamental plane, suggest that they were formed in a monolithic fashion. Moreover, the evidences in favour of *downsizing* in mass assembly suggest that the epoch of the formation of the bulk of star of an elliptical and its assembly epoch coincides, according to the monolithic collapse view.

Nevertheless, both theory and observations point out to a more complex situation. The detection at low redshift of a large population of ultraluminous infrared and sub-millimeter galaxies, whose emission is triggered by major mergers event, implies that mergers invoked in the hierarchical scenario do occur. Even the size-evolution at a given stellar mass supports the hierarchical paradigm. At a given stellar mass, objects were much smaller, and hence denser, in the past than at the present time (Trujillo et al., 2007). The fact that the small-sized, high-mass objects that are observed at high redshift are not observed in the nearby universe, suggest that this population merge with other galaxies over several billion of years, forming the larger galaxies that we see today. From a theoretical point of view, a number of N-body simulation (Toomre & Toomre, 1972; Toomre, 1977) of mergers of disk-like galaxies, show that the end-product of such process is a spheroids.

Reality, most likely, is a combination of both hierarchical and monolithic, with the former driving the formation of disk galaxies and the latter controlling the spheroids formation. Nowdays, one of the major effort of theoretical in the field of structure formation is to reconcile the *downsizing* phenomenon, or the monolithic-like appearence of spheroids, in the context of the current scenario of cosmic structure formation, called ΛCDM scenario, that, as we will see in the next chapter, has a number of verifications. This makes one of the motivations of the present Thesis work.

2

Hierarchical Structure Formation

In this chapter we review some basics concepts of modern cosmology and of structure formation, upon which our approach of galaxy formation modelling is based. We describe our current vision of the universe, and the current theory of hierarchical structure formation, in the linear and non-linear regime. Finally, the framework of Press-Schecter and Extendend-Press Schechter theories, which provide fundamental informations about the statistical quantities of haloes, are described.

2.1 Introduction

The basic picture of modern "Big Bang" cosmology is of a universe which began from a hot and homogeneous state. Overdense regions which are believed to arise from quantum fluctuations and were amplified during a period of rapid inflation, become more overdense with respect to their suroundings as the universe expands. Eventually the self-gravity acting on these regions becomes larger than the pressure of the expansion and they "turn-around" and collapse to form bound structures. This structure formation scenario is termed "hierarchical structure formation" because smaller objects collapse first and are then incorporated to larger structures that collapse later. These dense, gravitationally bound structures are the environment where galaxies form and evolve. In this Chapter we intruduce the basic concepts upon which this hierachical scenario is based, in order to justify the approach we followed in building our model of galaxy formation.

2.2 Matter Content in the Universe

One of the fundamental problem in modern astrophysics is to understand what kind of matter fills the universe. In the past few decades, there has been a lot of evidences accumulating that suggest that the universe is not enirely made by baryonic matter, i.e. the ordinary visible matter such as protons, but it is dominated by some form of matter that we can not see. One of the major breakthrough in understanding the component of our universe came with the Wilkinson Microwave Anisotropy Probe (WMAP) mis-

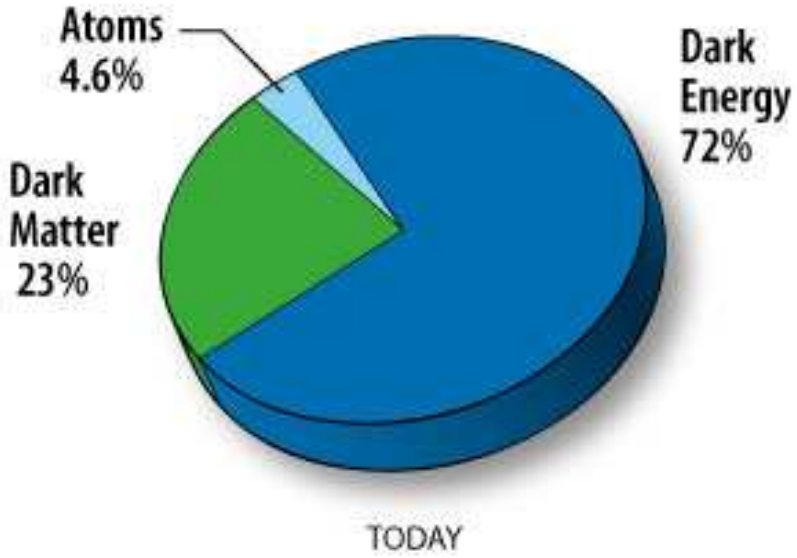

FIGURE 2.1— Schematic representation of the matter content of the universe as recovered by WMPA3 data.

sion (Spergel et al. 2003, 2007) which reveals the conditions of the early universe by measuring the properties of the cosmic microwave background (CMB) radiation over the full sky. This microwave radiation was released approximately 380,000 years after the birth of the universe. WMAP creates a picture of the microwave radiation using differences in temperature measured from opposite directions (anisotropy). By making accurate measurements of these anisotropies WMAP was able to measure the basic parameters of the Big Bang model including the density and composition of the universe, in particular measuring the relative density of baryonic and non-baryonic matter to an accuracy of better than a few percent of the overall density. The universe is observed to be filled with the following components:

- 4.6% baryonic atom
- 23% Dark Matter
- 72% Dark Energy

how it is shown in Figure 2.1. In the following we give a bief summary of what each component means.

2.2.1 Baryons

The different probes of baryon abundance in the Universe (primordial nucleosynthesis of light elements, the ratios of odd and even CMBR acoustic peaks heights, absorption

lines in the Lyα forest) have been converging in the last years towards the same value of the baryon density: $\Omega_b \approx 0.046$.

The present-day abundance of baryons in virialized objects (normal stars, gas, white dwarfs, black holes, etc. in galaxies, and hot gas in clusters) is $\Omega_B \approx 0.0037$, which accounts for $\approx 9\%$ of all the baryons at low redshifts. The gas in not virialized structures in the Intergalactic Medium accounts for $\approx 73\%$ of all baryons. Instead, at $z > 2$ more than 88% of the universal baryonic fraction is in the Lyα forest composed of cold HI clouds.

2.2.2 Dark Matter

Several evidences seem to indicate the need to introduct some form of hidden mass, called *Dark Matter* (DM), which manifests itself only through gravity. Historically, the first detection of Dark Matter was made in 1933 by Zwicky. He looked at the dispersion of velocities in the Coma cluster and deduced a mass-luminosity ratio $\sim$ 300, from the application of the virial theorem, which implies that light does not track mass at these large scales. More recent measurements end up with a value very close to the one observed by Zwicky.

Several evidences lead to the conclusion that Dark Matter is present even in the neighbourhood of individual galaxies under the form of dark haloes. The need of such haloes was first suggested on the basis of theoretical arguments. In fact N-body simulations demonstrated that disks are prone to dynamical instability unless they develop a bar in the central region (Ostriker et al. 1974). The fact that most spirals does show any bar suggested the possible existence of some form of invisible matter surrounding galaxies.

The most stringent test on Dark Matter perhaps comes from the rotation curves of spiral galaxies. Assuming that disks are in centrifugal equilibrium and that the orbits are circular (both are reasonable assumptions for non-central regions), the measured rotation curves are good tracers of the total (dynamical) mass distribution. The mass distribution associated with the luminous galaxy (stars+gas) can be inferred directly from the surface brightness (density) profiles. For an exponential disk of scalelength R_d (=3 kpc for our Galaxy), the rotation curve beyond the optical radius ($R_{opt} \approx 3.2R_d$) decreases as in the Keplerian case. The observed HI rotation curves at radii around and beyond R_{opt} are far from the Keplerian fall–off, implying the existence of some hidden mass and the fraction of this DM increases with radius (Rubin et al. 1980; Bosma 1981). The exploitation of rotation curve as DM tracers can be used tipically up to $2 - 5R_{opt}$. In order to probe the dynamics of galaxies at much larger radii satellite galaxies can be used if their statistics is sufficient. Another more recent and direct technique, is the technique of gravitational lensing. Here we differentiate between ‘strong lensing’, where the foreground lensing mass density is often sufficient to create multiple images of the background source, and ‘weak lensing’, the statistical distortion of the background population by large-scale structure. While strong lensing is likewise effective in providing important constraints on the distribution of DM on small scales

(<100 kpc), the weak lensing tecnique offers a unique probe of dark matter mass at lareger radii. The results show that a typical L_* galaxy (early or late) with a stellar mass of $M_s \sim 6 \times 10^{10} M_\odot$ is surrounded by a halo of $\sim 2 \times 10^{12} M_\odot$ (Mandelbaum et al. 2005). The extension of the halo is typically $\approx 200 - 250$kpc. These numbers are very close to the determinations for our own Galaxy.

There are a number of plausible speculations on the nature of the dark matter. The simplest hypothesis about this is that Dark Matter is baryonic, but not incorporated to visible stars. Brown Dwarfs have been proposed as a possible source of invisible matter. These are stars having mass which is less than one twentieth of our Sun, hence its core is not hot enough to burn either hydrogen or deuterium, so it shines only thanks to its gravitational contraction. Brown Dwarfs and similar objects have been called MACHOs (MAssive Compact Halo Objects). The other possible form of baryonic Dark Matter comes from Supermassive Black Holes (SMBH), whose existence in the central region of most galaxies, has been confirmed, but they have to existe in a copious number in order to account for the Dark Matter content of the universe. Both MACHOs and BHs are potentially detectable through gravitational lensing experiments. Actually, the balance of cosmological evidences favour a non-baryonic nature of Dark Matter. These evidences come from the measurements of the baryonic contribution to the density parameter, from primordial nucleosynthesis and from WMAP data, as already mentioned. Although perhaps the most natural species of non-baryonic matter is the massive neutrino, it is far from being the only candidate. A common way to refer to all particles that are plausible candidates to being Dark Matter, is WIMP (Weakly Interacting Massive Particle).

The main distinction among different Dark Matter candidates is between Hot Dark Matter (HDM) particles and Cold Dark Matter (CDM) ones. In the former case, particles decouple from radiation when relativistic, that means that particles can not be too massive, of the order of $\sim 10eV$, a natural candidate for this kind of DM is the neutrino. In the latter case, particles decouple while they are nonrelativistic, and their mass can apparently be as large as desired. In the HDM scenario, perturbations on scales as large as galaxy clusters are damped out by free streaming, while in the other case, the CDM one, perturbations of all scales of cosmological interest, from galaxies to clusters, can survive free streaming and a hierarchical scenario of structure formation is likely to occur.

2.2.3 Dark Energy

As implied by a variety of recent measurements, in particular CMB anosotropy measurements by WMAP (Spergel et al. 2007) and observations of high-redshift type-Ia Supernovae (Riess et al. 1998; Perlmutter et al. 1999), Dark Energy makes up a large majority of the total content of the universe, but its nature still remains a mystery in modern astrophysics. This term corresponds to a “cosmological constant”, perhaps related to the quantum vacuum energy. It was first proposed by Einstein, in order to correct the equation of general relativity such that a static universe could be obtained.

After the expanding universe model, introduced by Friedmann, became the current view of the universe, this term was canceled. In recent years, the cosmological constant has become again popular since the observations of distant Supernovae indicate that the universe is now in a phase of accelerating expansion. This requires the inclusion of a term acting as a negative pressure in the equation of cosmic expansion. Various theoretical models are being developed in order to take into account dark energy, and it is possible that large scale structure studies may help in discriminating among them (Guzzo et al. 2008).

2.3 Backgound Cosmology

The simplest cosmological model that describes, in a sufficient coherent manner, the evolution of the universe, from $10^{-2}s$ after the initial singularity to now, is the so called *Standard Cosmological Model* (or Hot Big Bang model). In this model the space-time geometry is described by the Friedmann-Robertson-Walker (FRW) metric, which is given by:

$$ds^2 = c^2dt^2 - a(t)^2\left[\frac{dr^2}{1-kr^2} + r^2(d\theta^2 + sin\theta^2 d\phi^2)\right] \tag{2.1}$$

where c is the light velocity, a(t) a function of time, or a scale factor called "expansion parameter", t is the time coordinate, r, θ and ϕ the comoving space coordinates. The evolution of the universe is described by the parameter a(t) and it is fundamentally connected to the value ρ of the average density.

The equations that describe the dynamics of the universe are the Friedmann's equations (Friedmann, 1924) that we are going to introduce in a while. These equations can be obtained starting from the equations of the gravitational field of Einstein:

$$R_{ik} - \frac{1}{2}g_{ik}R = -\frac{8\pi G}{c^4}T_{ik} \tag{2.2}$$

where now, R_{ik} is a symmetric tensor, also known as Ricci tensor, which describes the geometric properties of space-time, g_{ik} is the metric tensor, R is the scalar curvature and T_{ik} is the energy-momentum tensor. These equations connect the properties of space-time to the mass-energy. In other terms they describe how space-time is modeled by mass. Combining Einstein equations to the FRW metric leads to the dynamic equations for the expansion parameter, a(t). These last are the Friedmann equations:

$$d(\rho a^3) = -pd(a^3) \tag{2.3}$$

$$\frac{1}{a^2}\dot{a}^2 + \frac{kc^2}{a^2} = \frac{8\pi G}{3}\rho \tag{2.4}$$

$$2\frac{\ddot{a}}{a} + \frac{\dot{a}^2}{a^2} + \frac{k}{a^2} = -8\pi G\rho \tag{2.5}$$

where p is the pressure of the fluid of which the universe is constituted, k is the curvature parameter and a(t) is the scale factor already introduced. Only two of the three

Friedmann equations are independent, because the first connects density, ρ, to the expansion parameter, a(t). The character of the solutions of these equations depends on the value of the curvature parameter, k. It is possible to rielaborate the first Friedmann equation (Eq. 2.4) and rewrite it in term of the Hubble parameter, defined as:

$$H(t) = \frac{\dot{a}}{a} \tag{2.6}$$

obtaining:

$$H^2\Big(1 - \frac{\rho}{\rho_c}\Big) = -\frac{kc^2}{a^2} \tag{2.7}$$

It is clear that the solution to the equation now written depends on the value of ρ with respect to the critical density, defined as:

$$\rho_c = \frac{3H^2}{8\pi G} = 2.775 \times 10^{11} h^2 M_\odot Mpc^{-3} \tag{2.8}$$

where $h = H/(100 km/sMpc)$ is the dimensionless Hubble parameter.

If $\rho > \rho_c$ space-time has a closed structure ($k = 1$) and equations show that the system goes through a singularity in a finite time. This means that the universe has an expansion phase until it reaches a maximum expansion after which it recollapses. If $\rho < \rho_c$, the expansion never stops and the universe is open, $k = -1$ (the universe has a structure similar to that of an hyperboloid, in the two-dimensional case). If finally, $\rho = \rho_c$ the expansion is decelerated and has infinite duration in time, $k = 0$, and the universe is flat (as a plane in the two-dimensional case). The concepts discussed can be expressed using the density parameter Ω which is the ratio between the density of the universe and the critical density:

$$\Omega = \frac{\rho}{\rho_c} \tag{2.9}$$

In this case, the condition $\Omega = 1$ corresponds to a flat universe ($k = 0$), $\Omega < 1$ means open universe ($k = -1$) while $\Omega > 1$ holds for a closed universe ($k = 1$).

The density parameter Ω is usually expressed as the sum of the component of the universe:

$$\Omega = \Omega_m + \Omega_\Lambda + \Omega_r \tag{2.10}$$

where Ω_m is the density parameter of matter, Ω_r refers to radiation, and Ω_Λ to the cosmological constant term, that we introduced in the previous section. Since in the matter dominated era the radiation term is negligible, a flat universe implies:

$$\Omega_m + \Omega_\Lambda = 1 \tag{2.11}$$

According to the recent WMAP three-years results (Spergel et al. 2007), the geometry of the universe is flat, with $\Omega_m = 0.28$ and $\Omega_\Lambda = 0.72$.

2.4 Linear Growth of Perturbations

We would like to derive expressions for the evolution of perturbations on this background universe. In the standard paradigm, primordial density fluctuations grew during an epoch of cosmological inflation and the primordial density contrast is a statistically homogeneous and isotropic Gaussian random field. It is worth to note that although the gaussianity of the random field is the simplest assumption, there are other variants that predict non-Gaussian fluctuations, but hereafter we will consider only the Gaussian case. We consider fluctuations in the density field $\rho(\vec{x})$ described by the density contrast

$$\delta(\vec{x}) = \frac{\rho(\vec{x}) - \rho_b}{\rho_b} \tag{2.12}$$

where ρ_b is the mean mass density in the universe and $\vec{x}$ is a comoving spatial coordinate.

At any given time, we can distinguish between the regime in which the proper wavelenght of the perturbation modes $\lambda(t)$ is much smaller than the horizon, and that in which this scalelenght is greater. In the former regime, the evolution of inhomogeneities may be studied in the simple Newtonian approximation, while in the latter case the full general relativistic treatment is needed. In the context of structure formation, we are interested in scales much smaller than the horizon, hence the Newtonian approximation holds. We can assume that matter is a collisionless, non-viscous fluid, where gravitation dominates over the interactions between particles (Peebles, 1980). Applying the continuity, Euler and Poisson equations to this fluid

$$\frac{\partial \rho}{\partial t} + \frac{\nabla \cdot (\rho \mathbf{u})}{a} = 0 \tag{2.13}$$

$$\frac{\partial u}{\partial t} + \frac{1}{a}(\mathbf{u} \cdot \nabla)\mathbf{u} = -\frac{\nabla p}{\rho} - \frac{1}{a}\nabla\phi \tag{2.14}$$

$$\nabla^2\phi = 4\pi G\rho a^2 \tag{2.15}$$

$$\tag{2.16}$$

where $\mathbf{u}$ is the velocity field. Assuming that we are in the linear regime, so that $\delta << 1$ and the equations can be linearized, we can obtain the equation for the evolution of overdensity:

$$\frac{\partial^2\delta}{\partial t^2} + 2\frac{\dot{a}}{a}\frac{\partial\delta}{\partial t} = 4\pi G\rho_b\delta \tag{2.17}$$

In the simple case of an Einstein-De Sitter universe ($\Omega_m = 1$ and $\Omega_\Lambda = 0$) equation 2.17 has solution:

$$\delta(\vec{x}) = A_+(\vec{x})D_+(t) + A_-(\vec{x})D_-(t) \tag{2.18}$$

The perturbation is then done of two parts: a growing one (which shall be denoted with $D_+(t)$), becoming more and more important with time and a decaying one, $D_-(t)$ becoming negligible with respect to the growing one as time increases. Focusing on

the growing mode, that is the only one to survive with time, we obtain that in the linear regime the growth of pertubations scale as:

$$\delta(t) = \delta(t_0)\frac{D_+(t)}{D_+(t_0)} \tag{2.19}$$

where t_0 is the time at present. Therefore all the information that we need to know about the growth of perturbations in the linear regime is contained in the term $D_+(t)$, also called the *linear growth factor*, that in the Einstein-De Sitter cosmology has the form

$$D(t) \propto a(t) \propto t^{2/3} \tag{2.20}$$

In the case of a ΛCDM universe, the analytic expression is more complex (Peebles, 1993). A useful approximation is given by Carroll 1992 and gives the ratio between the growth factor at a given time t to the present-day one:

$$\delta_0 = \frac{D(t)}{D(t_0)} = \frac{5}{2}\Omega_m\Big[\Omega_m^{4/7} - \Omega_\Lambda + \Big(1 - \frac{1}{2}\Omega_m\Big)\Big(1 + \frac{1}{70}\Omega_\Lambda\Big)\Big]^{-1} \tag{2.21}$$

2.5 The Spectrum of Perturbations

We also need to describe the spatial dependence of fluctuations. As we have already mentioned, inflation predicts that the perturbations field should be described by a Gaussian random field. In this case it is convenient to represent them in Fourier series, as a superposition of plane waves, indipendently evolving:

$$\delta(\vec{x}) = \frac{1}{2\pi^3}\int d^3k\delta_k e^{-ik\vec{x}} \tag{2.22}$$

where $k = 2\pi/\lambda$ and δ_k are the complex Fourier coefficients.

For a Gaussian random field any statistical quantity of interest can be specified in terms of the power spectrum

$$P(k) = \frac{1}{V} < |\delta_k|^2 > \tag{2.23}$$

which measures the amplitude of the fluctuations at a given scale k. Here V is a volume, which can be thought of as a "realization" of the universe.

A choice often made for the primordial spectrum is $P(k) = Ak^n$, where A is only a normalization constant, which in the case $n = 1$ gives the scale invariant spectrum of Harrison-Zeldovich (Kolb & Turner 1990) and it is the one predicted by the simplest inflationary theories. A particular case of the scale invariant spectrum is the white-noise case, for which $n = 0$, i.e. the power is the same on all scales.

During the evolution of the universe and after perturbations enter the horizon, the spectrum is subject to modulations because of physical processes characteristic of the

model itself. These effects are taken into account by means of the transfer function $T(k;t)$ which connects the primordial spectrum $P(k;t_p)$ at time t_p to the final time t_f:

$$P(k;t_f) = \left[\frac{D(t_f)}{D(t_p)}\right]^2 T^2(k;t_f)P(k;t_p) \tag{2.24}$$

where D(t) is the law of grow of perturbations, in the linear regime. In the case of CDM models the transfer function is:

$$T(k) = \left\{1 + \left[ak + (bk)^{1.5} + (ck)^2\right]^{\nu}\right\}^{\frac{-1}{\nu}} \tag{2.25}$$

(Bond e Efstathiou 1984), where $a = 6.4(\Omega h^2)^{-1}Mpc$; $b = 3.0(\Omega h^2)^{-1}Mpc$; $c = 1.7(\Omega h^2)^{-1}Mpc$; $\nu = 1.13$.

A more intuitive quantity than $P(k)$ is the *mass variance* of the fluctuations:

$$\sigma^2 =< \left(\frac{\delta M}{M}\right)^2 > \tag{2.26}$$

its physical meaning is that of an *rms* density contrast on a given sphere of radius R associated to the mass $M = \rho V_W(R)$, where $W(R)$ is a window smoothing function. The window function can have different shapes (see Lacey & Cole 1993, hereafter LC93), the most common choices are the top-hat window in the Fourier space, or the Gaussian window. The mass variance can be also expressed in terms of the power spectrum:

$$\sigma^2 = \frac{1}{(2\pi)^3}\int P(k)W(k,R)d^3k \tag{2.27}$$

In the following we will often refer to the mass variance as S, which is simply defined as the square of the mass variance: $S = \sigma^2$.

2.6 Spherical Collapse

Linear evolution for the growth of perturbations is valid only in the case of small amplitude fluctuations, i.e. when $\delta << 1$ or similarly, when the mass variance, σ, is much less than unity. When this condition is no longer verified it is necessary to develope a non-linear theory. For example in regions smaller than $8h^{-1}$ Mpc the measured value of the mass variances is close to unity, as derived for example by WMAP measurements, which give $\sigma_8 = 0.74$. At this scales galaxies are not a Poissonian distribution but they tend to cluster.

If one wants to study the properties of galactic structures or clusters of galaxies, it is necessary to introduce a non-linear theory of clustering. Such a theory is too complicated to be developed in a purely theoretical fashion. The problem can be faced, by using N-Body simulations of the interesting system or assuming certain approximations that simplifies it.

Spherical symmetry is one of the few cases in which gravitational collapse can be solved exactly (Gunn & Gott 1972; Peebles 1980). In fact, as a consequence of

Birkhoff's theorem, a spherical perturbation evolves as a FRW Universe with density equal to the mean density inside the perturbation.

The simplest spherical perturbation is the top-hat one, i.e. a constant overdensity δ inside a sphere of radius R; to avoid a feedback reaction on the background model, the overdensity has to be surrounded by a spherical underdense shell, such to make the total perturbation vanish. The evolution of the radius of the perturbation is then given by a Friedmann equation.

The evolution of a spherical perturbation depends only on its initial overdensity. In an Einstein-de Sitter background, any spherical overdensity reaches a singularity (collapse) at a final time:

$$t_c = \frac{3\pi}{2}\left(\frac{5}{3}\delta(t_i)\right)^{-3/2} t_i. \tag{2.28}$$

where t_i is the initial time. By that time its linear density contrast reaches the value:

$$\delta(t_c) = \delta_c = \frac{3}{5}\left(\frac{3\pi}{2}\right)^{3/2} \simeq 1.69. \tag{2.29}$$

In an open Universe not any overdensity is going to collapse: the initial density contrast has to be such that the total density inside the perturbation overcomes the critical density.

Of course, collapse to a singularity is not what really happens in reality. It is typically supposed that the structure reaches virial equilibrium at that time. In this case, arguments based on the virial theorem and on energy conservation show that the structure reaches a radius equal to half its maximum expansion radius, and a density contrast of about 178. In the subsequent evolution the radius and the physical density of the virialized structure remains constant, and its density contrast grows with time, as the background density decays. Hence, structures which collapse before are denser than the ones which collapse later.

Spherical collapse can describe the evolution of underdensities. A spherical underdensity is not able to collapse but behaves as an open universe, always expanding unless its borders collide with neighboring regions. At variance with overdensities, underdensities tend to be more spherical as they evolve, so that the spherical model provides a very good approximation for their evolution.

From Equation 2.28 one can note that initially denser regions collapse before than less dense regions. This means that, at any given epoch, there is some critical value for the density which must be exceeded, and this value, that now is 1.69 (see Eq. 2.29) does not depend on the mass. We will see in the next section that is no more true if a more complex model for the collapse is considered.

2.7 Ellipsoidal Collapse

Despite the simplicity of the spherical collapse model it was argued that it does not give a realistic description of the formation of real structures and a more accurate treatment

can be done with the ellipsoidal collapse model (Bond & Myers 1996). In this case the time of virialization is chosen as the time when the third axis collapses. Some freedom is assumed in how each axis is supposed to evolve after the turn-around. In some cases (Sheth & Tormen 2001) it is assumed that each axis is frozen once it has reached some critical value.

In the ellipsoidal collapse model, less massive objects must initially have been denser than more massive objects which collapse at the same time, since smaller systems have had to hold themselves together against strong tidal forces (Sheth et al. 2001).

Hence, if we think at the perturbation collapse as an upcrossing of the barrier, whose height is given by the density contrast to be reached, in the spherical collapse model this height is fixed, and it depend only on time, while in the ellipsoidal collapse case the barrier shape depends on mass, and it is higher for smaller masses.

2.8 Press-Schechter Theory

Press & Schechter, 1974 (PS heareafter) derived a relation for the mass function of virialized objects from the hierarchical density field. The counting of the umber of collapsed objects can be traced back to the linear theory by considering Their theory was based upon these hypotheses:

- the linear density field is described by a stochastic Gaussian field. The statistics of the matter distribution is Gaussian.
- the counting of the number of collapsed objects can be traced back to the linear theory by considering the structures formed in those regions where the overdensity linearly evolved and filtered with a top-hat filter exceeds a threshold δ_c ($\delta_c = 1.69$, obtained from the spherical collapse model, see Eq. 2.29).
- for $\delta \geq \delta_c$ regions collapse to points.

The haloes mass function is then computed assuming that the probability that an object forms at a certain point is proportional to the probability that the point is in a region with $\delta \geq \delta_c$.

A problem of this kind of approach is the so called “cloud-in-cloud” problem, namely the fact that a fluctuation on a given scale can contain substructures on smaller scales and the same fluid element can be assigned, in the PS approach, to haloes of different mass. Moreover, in a hierarchical scenario, one expects to find all the mass collapsed in objects of some scale, while the PS model can account only for half of it: this problem is intimately related to the fact that in a Gaussian field only half volume is overdense. Press and Schechter faced the problem by simply multiplying their result by a fudge factor of 2.

A more general approach in order to derive the mass function of virialized objects is the excursion-set approach, developed by Bond et al. (1991). Their approach is to smooth the linear density field δ over spheres of successively larger masses, and

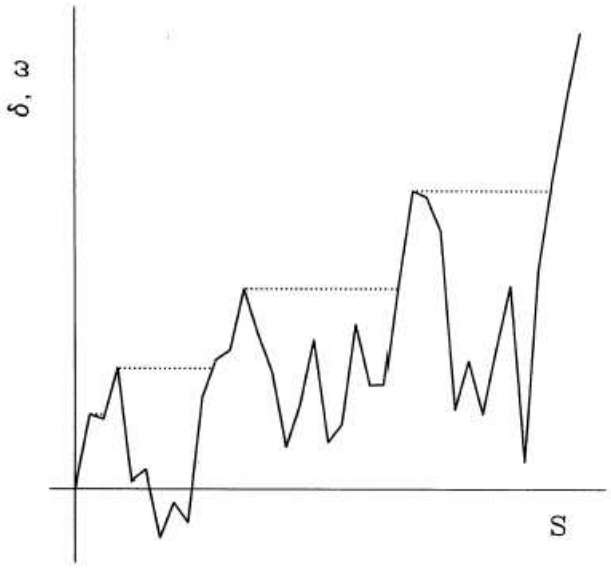

FIGURE 2.2— The solid line shows the trajectory of the density contrast δ as the smoothing scale is varied. Taken from LC93.

then to assume that the mass of the halo containing a given particle at time t equals the mass M of the largest sphere, placed around the initial position of that particle, within which the average δ exceeds the threshold for collapse $\delta_c(t)$, i.e. the barrier, calculated as described in Section 2.7. This method ensures that the halo so identified will not have been engulfed in a still larger structure, since the surrounding region, when avereged on all larger scales will have a mean density below the critical value and will not yet have collapsed according to this criterion. Smoothing the density field over larger and larger field is equivalent to consider trajectories in the plane (S, δ), where S is the square of the mass variance, already introduced (see Figure 2.2).

The value of δ executes a random walk as the smoothing scale R (or M) is changed. We can consider the trajectories in the plane (S, δ_c) and associate the fraction of matter in collpased objects in the range dM around M at the time t with the fraction of trajectories that make the first upcrossing through the threshold δ_c in the interval $S, S + dS$ and this results in the well-known PS mass function:

$$f(S, \delta_c)dS = \frac{1}{\sqrt{2\pi}} \frac{\delta_c}{S^{3/2}} exp\Big(- \frac{\delta_c^2}{2S}\Big)dS \tag{2.30}$$

This expression represents the fraction of mass in the range dM around M corresponding to a given S, through the power spectrum chosen. The comoving number density of haloes of mass M present at time t is therefore given by:

$$\frac{dn}{dN}(M, t) = \frac{\rho_0}{M} f(S, \delta_c) \Big| \frac{dS}{dM} \Big| dM \tag{2.31}$$

2.9 Mass Function in the Ellipsoidal Collapse Model

Although the analytical framework of the PS model has been greatly refined and extended, it has been shown that the PS mass function, while qualitatively correct, disagrees with the results of high resolution N-body simulations. In particular, the PS formula overestimates the abundance of haloes near the characteristic mass M_* and underestimates the abundance in the high mass tail (Efstathiou et al. 1988; White, Efstathiou & Frenk 1993; Lacey & Cole 1994). The quoted discrepancy is not surprising since the PS model, as any other analytical model, should make several assumptions to get simple analytical predictions. One of this approximation is the assumption of the spherical collapse model which ignores the effect of tides.

Incorporating the effects of the ellipsoidal collapse model, namely the moving barrier model, in the excursion set approach lead to the derivation of mass functions that are in better agreement with N-body simulations. Analytic approximation for the mass function was given by Sheth & Tormen (2002), hereafter ST, who derived the first upcrossing of random walks in the case of a moving barrier, whose shape is given by:

$$B(S,\delta_c) = \sqrt{a}\delta_c\Big(1+\beta\Big(a\frac{\delta_c^2}{S}\Big)^{-\alpha}\Big) \tag{2.32}$$

where $\alpha = 0.615$, $\beta = 0.485$, $a = 0.75$. The relative mass function (the analogous of eq. 2.30) is:

$$f_{ST}(S,\delta_c)dS = \frac{1}{\sqrt{2\pi}S^{3/2}}|T(S)|exp\Big(-\frac{B(S)^2}{2S}\Big)dS \tag{2.33}$$

where $B(S)$ is the barrier of equation 2.32 and $T(S)$ denotes the sum of the first few terms in Taylor series expansion of $B(S)$:

$$T(S) = \sum_{n=0}^{5}\frac{(-S)^n}{n}\frac{\partial^n B(S)}{\partial S^n} \tag{2.34}$$

In Figure 2.3 we show the comparison between the mass function derived in different formalism with the one resulting from N-body simulations. While the PS may explain the gross features of the mass function recovered by N-body simulations, it fails in its details, predicting too many low-mass haloes and too few high-mass haloes. The halo mass function derived in the context of ellipsoidal collapse model results in a better agreement with the N-bodt one even in the low-mass and high-mass limits.

2.10 Extendend Press-Schechter

One of the beautiful aspects of the excursion-set approach described so far is that it allows to extend the above derivations and to compute, in a very natural way, the conditional mass function of haloes, that is the fraction of trajectories in haloes with mass M_1 at z_1 that are in haloes with mass $M_0 > M_1$ at $z_0 < z_1$. This approach was first developed by Lacey & Cole (1993) and it is commonly known as *Extended*

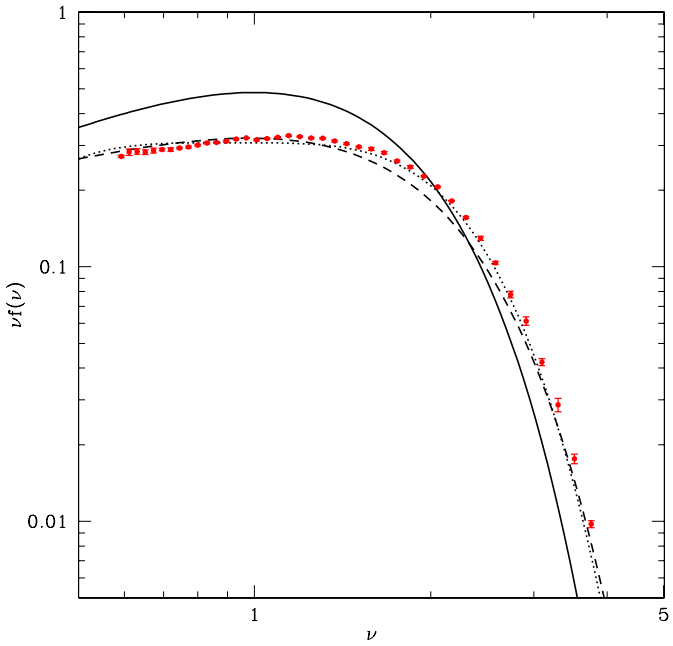

FIGURE 2.3— Mass function in terms of the rescaled variable $nu = \delta_c/S$. Red dots are the results from N-body simulations (ref?), solid line is the mass function derived in the PS approach. Dashed and dotted lines represent, respectively, the improved model of ST and Jenkins et al. (2001). Taken from Zentner (2006).

Press-Schecter model (EPS). The issue concerns the problem of finding that subset of trajectories that make their first upcrossing of a barrier whose height is δ_{c0} at S_0 (the mass variance corresponding to M_0) and then continue until they eventually cross a second barrier of height $\delta_{c1} > \delta_{c0}$ at various value of S_1. These trajectories represent haloes which at the time corresponding to δ_{c1} have masses corresponding to S_1 and that at later times corresponding to δ_{c0} have merged to form a bigger halo with mass corresponding to S_0. The conditional probability that one of these walks will make its first upcrossing in the interval S_1 to $S_1 + dS$ can be obtained directly from equation 2.30 noting that this is the same situation as before but with the source of trajectories moved from the origin to (S_0, δ_{c0}), and leads to:

$$f(S_1, \delta_{c1}|S_0, \delta_{c0})dS = \frac{1}{\sqrt{2\pi}} \frac{(\delta_{c1} - \delta_{c0})}{(S_1 - S_0)^{3/2}} exp\Big[- \frac{(\delta_{c1} - \delta_{c0})^2)}{2(S_1 - S_0)} \Big] dS_1 \qquad (2.35)$$

Converting from mass weighting to number weighting we obtain the average number of progenitors at z_1 in the mass interval dM_1 around M_1 which at redshift z_0 has merged to form an M_0 halo:

$$\frac{dP}{dM_1}(M_1, z_1|M_0, z_0)dM_1 = \frac{M_0}{M_1} f(S_1, \delta_{c1}|S_0, \delta_{c0}) \Big| \frac{dS}{dM} \Big| dM_1 \qquad (2.36)$$

As for the global mass function (also called *unconditional mass function*), it is possible to derive conditional mass functions (CMF) even for the case of a moving barrier, in the ellipsoidal model (ST).

The framework described so far, in particular the EPS formalism, constitutes the basis to generate merger tree algorithms, i.e. actual realizations of the merging history for a large set of haloes, that we are going to describe in the next Chapter.

3

The Merger tree

In this Chapter we describe the methods employed in order to build the merger tree that we used for the semi-analytic model. After a brief overview of the algorithms existing in literature we describe our method, valid for both spherical and ellipsoidal collapse model. We test the algorithm comparing conditional and unconditional mass functions with theoretical expectations and with N-body simulations.

3.1 Introduction

In the hierarchical structure formation scenario, dark matter haloes grow by accreting and merging with other haloes. The modelling of halo merger histories is the first step towards the building of a semi-analytic model of galaxy formation. Once we set up the environment where galaxies form and evolve we can implement processes involving baryon physics as we will discuss in the next Chapter.

In order to study the framework of structure formation two different approaches are feasible. The first one is through the use of N-body simulation. Although they can give us a lot of useful information about the detailed merging histories of haloes they are computationally expensive and it is not possible to implement them on standard computers. Moreover they have a limited mass resolution which is given by the particle mass. With the Millennium Simulation carried out by the Virgo Consortium (Springel et al. 2001) which is by now the highest resolution simulation, a minimum halo mass of $1.7 \times 10^{10} M_{\odot}/h$ is achieved.

On the other side, the most frequently used framework for studying the build-up of dark haloes is the PS formalism, with its extensions, that we have described in the previous Chapter. The great advantage of this approach, apart from being computationally very fast and flexible, is the fact that it is possible to compute merging histories down to arbitrary low mass resolution. Since the EPS model does not specify explicitly how to group progenitors into parents, for the aim of a semi-analytic model, it is necessary

to build a merger tree, that provides the hierarchical link among progenitor and parent haloes.

Although the PS theory is simple and works remarkably well, it is known that it does not provide a perfect fit to the number density of haloes found in the simulations and to the conditional mass function. The reason is that the spherical collapse model upon which PS formalism is based gives an inadequate description of the collapse of haloes. Sheth & Tormen (2002) show that the theory of ellipsoidal collapse can lead to more reliable predictions for that quantities. Sheth et al. (2001) incorporate the moving barrier model into the excursion set approach, giving analytic expressions for conditional and unconditional mass function in almost perfect agreement with the N-body ones, at least in the range of masses probed by numerical simulations.

In this Chapter we describe a new algorithm for building a merger tree which is an extension of the one of Sheth & Lemson 1999 (SL99) to ΛCDM power spectrum. This algorithm is easily implementable in the case of moving barrier, in order to produce progenitor distributions which are in a better agreement with N-body simulations. Before describing the existing algorithms of such kind we want to describe the terminology used hereafter for the hierarchy of the tree. We call *parent* the massive haloes which exist at low redshift and from which other haloes are generated and we call *progenitors* the smaller objects that derive from it at higher redshift.

In the following we assume a ΛCDM cosmology, with $\Omega_m = 0.3$, $\Omega_\Lambda = 0.7$, $h = 0.7$ and $\sigma_8 = 0.9$. We keep the same cosmological parameters throughout the rest of the Thesis.

3.2 Previous methods for merger trees

In Monte Carlo (MC) merger trees the progenitor haloes are generated through the use of random number generators. In literature a number of different algorithms for building trees exists. In fact the process to assign progenitors to a given parent halo is not unique and it is subject to a lot of subtleties.

A good algorithm is required to satisfy two major characteristics. First of all it has to reproduce the mean quantities predicted by analytic theory and secondary it has to preserve mass, i.e. the sum of the mass of all progenitors must be equal to the parent halo mass. Even if they appear obvious requirements, it is not always trivial to satisfy both at the same time.

The first merger trees in literature were done using the binary approximation, in which each halo mass is splitted in two progenitors, and the same is done with the new progenitors. This is the simplest way to draw progenitors, however, it will intrinsically fail to reproduce the progenitor mass function as demonstrated by Somerville & Kolatt (1999), hereafter SK99. The reason of the failure lies in the property of asymmetry of the progenitor mass function $f(M|M_0)$. In fact, as demonstrated by Zhang et al. (2008), this function is not symmetric around $M_0/2$, in the sense that there are slightly fewer progenitors with mass below $M_0/2$ than above and hence, it is not possible for all the progenitors wit $M > M_0/2$ to have a binary counterpart with mass $M_0 - M < M_0/2$.

Even if this asymmetry is typically small, an accurate algorithm must take this into account, in order to avoid an excess of progenitors (see SK99).

In the following we describe four algorithms existing in literature for building merger tree. Although much more algorithms exist, we focus our attention on these because they are the most commonly used, especially in the semi-analytic modelling.

3.2.1 Lacey & Cole 1993 (LC93)

The algorithm proposed by LC93 makes two important assumptions: all mergers are binary (before mass resolution is imposed), and the parent mass M_0 is the sum of the two progenitor masses M_1 and M_2 (where $M_1 \geq M_2$). For each small look-back time step and for each parent, a progenitor mass is randomly chosen according to the mass-weighted conditional mass function eq. (2.35), and the mass of the other progenitor (which can be larger or smaller) is simply set to be the difference between M_0 and the first chosen progenitor mass. An easy way to generate random progenitor masses makes use of the parameter transformation:

$$x = (\delta_{c1} - \delta_{c0})/2(S_1 - S_0) \tag{3.1}$$

The parameter x has a uniform probability distribution between 0 and 1 and can be quickly generated using any random-number generator. A simple inversion then yields progenitors distributed according to the mass-weighted conditional mass function. This approach is commonly used in several MC algorithms based on the EPS approach. If the less massive progenitor M_2 falls below a chosen mass resolution $M_{\rm res}$, or equivalently, $M_1 > M_0 - M_{\rm res}$, then M_1 is kept but M_2, being a sub-resolution progenitor, is discarded and results in single-progenitor haloes. Because of the binary approximation, this algorithm produces close agreement with the EPS expectations for small look-back times, but produces an excess of progenitors at larger look-back times, because the discrepancies due to the asymmetry of the CMF are amplified after many timesteps.

3.2.2 Kauffmann & White 1993 (KW93)

For each timestep in the KW93 algorithm, a large number of progenitors are generated across many progenitor mass bins for a fixed number of parent halos of the same mass. The number of progenitors in each mass bin is determined by the progenitor mass function of the parent halo mass, and rounded to the nearest integer value. These progenitors are then assigned to the parent halos in order of decreasing progenitor mass. The target parent halo is chosen with a probability proportional to its available mass (i.e. the mass not yet occupied by progenitors), and with the restriction that the total mass of the progenitors in a parent halo cannot exceed the parent mass. This procedure allows one to work out all the merger configurations and their frequencies for one time step and for different parent halo masses. This information is then stored and used repeatedly for determining the progenitors of a halo at each time step.

This algorithm produces CMF consistent with the EPS expectations. Its major drawback is that it does not guarantee mass conservation, in fact it is possible a situation in which a progenitor is not assigned to any realization because most massive than the remaining mass. It is also computationally expensive because it requires a big amount of memory in order to store all the information about different realizations.

3.2.3 Somerville & Kolatt 1999 (SK99)

SK99 point out that the assumptions of binary mergers and $M_0 = M_1 + M_2$ made in LC93 lead to an overestimate of the progenitors abundance at high redshift. They first attempt to remedy this problem by preserving the binary assumption while allowing the mass below the resolution limit $M_{\rm res}$ to be counted as diffusely accreted mass ΔM. They show, however, that this "binary tree with accretion" method fails in the opposite direction, underproducing the progenitor mass function relative to the spherical EPS prediction. This discrepancy arises partly because whenever two progenitors are chosen in this method, the remaining mass is assigned to ΔM regardless of whether it is above or below $M_{\rm res}$. Thus the EPS $f(M_1, \delta_{c1}|M_0, \delta_{c0})$ is not faithfully reproduced: the binary tree with accretion method yields an excess of accreted mass and a corresponding lack of low-mass halos.

SK99 then consider a natural extension of this method, in which both assumptions made in LC93 are relaxed. In this "N-branch tree with accretion" algorithm, each parent halo is allowed to have more than two progenitors for every simulation timestep. To guarantee that the total mass of the progenitors does not exceed that of the parent, each subsequent progenitor mass is randomly chosen from the mass-weighted conditional mass function truncated to the maximally possible progenitor mass. This procedure is repeated until the parent halo cannot contain any more progenitors with masses above $M_{\rm res}$, and the remaining mass deficit is assigned to diffuse accretion ΔM. The parameter transformation of eq. (3.1) is also applicable for SK99. The probability distribution of x is still uniform, but the upper limit of x can now take on any value between 0 and 1 depending on where the conditional mass function is truncated.

Although they show to be able to reproduce the gross features of the EPS conditional mass function it was shown that they fail in reproducing the low-mass end of the distribution, especially at small timesteps (Zhang et al. 2008). Moreover, in order to get a reasonable agreement with the theoretical expectations they have to fine-tune the grid of timesteps used, that is particularly uncomfortable when this merger tree has to be used for semi-analytical modelling, and one wants to choose the grid in arbitrary way. Besides this last feature does not satisfy the requirements for a "good" merger tree to reproduce the EPS progenitor distribution at any redshift as we have mentioned above.

3.2.4 Cole et al. 2000 (C00)

Similar to SK99, C00 treats the mass in progenitors smaller than the mass resolution $M_{\rm res}$ in the Monte Carlo simulation as accreted mass, but unlike the N-branch tree

model in SK99, only a maximum of two progenitors are allowed per parent. The amount of accreted mass gained in one timestep, ΔM, is fixed to a single value and is calculated by integrating the mass-weighted conditional mass function from 0 to $M_{\rm res}$:

$$\Delta M = \int_0^{M_{\rm res}} M f(M_1, \delta_{c1}|M_0, \delta_{c0}) dM \,, \tag{3.2}$$

where M_0 is the parent mass. The progenitors are drawn from the *lower* half of the progenitor mass function between $M_{\rm res}$ and $M_0/2$ according to the average number of progenitors in that range:

$$p = \int_{M_{\rm res}}^{M_0/2} f(M_1, \delta_{c1}|M_0, \delta_{c0}) dM \,. \tag{3.3}$$

The simulation timestep is chosen to be small enough so that $p \ll 1$

The C00 merger tree is generated with the following steps: a random number x between 0 and 1 determines whether a parent halo has one progenitor (if $x > p$) or two progenitors (if $x \leq p$). In the case of a single progenitor, its mass is $M_1 = M_0 - \Delta M$. In the case of two progenitors, the mass of the smaller progenitor, M_2, is chosen randomly between $M_{\rm res}$ and $M_0/2$ according to the progenitor mass function. The larger progenitor is then assigned a mass of $M_1 = M_0 - M_2 - \Delta M$. Since $p \ll 1$, most parents form via $1 \rightarrow 1$ events rather than $2 \rightarrow 1$ events.

This algorithm works fairly well, but significantly underestimates the CMF at the high-mass end, particularly for high look-back time, mainly because of the wrong binary assumption.

3.3 Sheth & Lemson approach

To generate Monte Carlo realizations of the merging history of dark matter haloes we use the partition algorithm described by Sheth & Lemson, 1999 (hereafter SL99). It is based on the assumption that in a Poisson or white-noise Gaussian distributions, mutually disconnected regions are mutually independent. In the Appendix of SL99, the authors give a detailed demonstration of the above statement, here we summarise only the major points:

- Given an initially Poisson distribution, the probability that a clump of particles has m particles associated is given by the Borel distribution (Borel, 1941):

$$\eta(m, b) = \frac{(mb)^{m-1} e^{-mb}}{m!} \tag{3.4}$$

  where $m \geq 1$ and b is a pseudotime variable related to the overdensity threshold: $b = 1/(1 + \delta_c)$. For an initially Poisson distribution δ_c decreases as the universe expands in such a way that $b \rightarrow 0$ initially and $b \rightarrow 1$ as the clustering develops, hence $0 \leq b < 1$.

- The probability $f(m,b)$ that a randomly chosen particle belongs to an m-clump is given by $\eta(m,b)$ multiplied by m and divided by the mean clump size $1/(1-b)$:

$$f(m,b) = m(1-b)\eta(m,b) \tag{3.5}$$

  with $\sum_{m=1}^{\infty} f(m,b) = 1$, since all matter is in clumps.

- The application of the excursion-set description helps in solving the two-barrier problem with this particular distribution and leads to the derivation of the probability that a randomly chosen particle of a clump having M_0 particles at the time corresponding to b_0 was a member of a M_1-clump at the time corresponding to b_1 (with $b_1 < b_0$, i.e. b_1 is an earlier time), that is the derivation of the conditional probability $f(M_1, b_1|M_0, b_0)$ (Sheth 1995) and hence the average number of progenitor M_1-subclumps identified at b_1 that are later in an M_0-clump:

$$N(M_1, b_1|M_0, b_0) = \frac{M_0}{M_1} f(M_1, b_1|M_0, b_0) \tag{3.6}$$

  (conversion from mass-weighting to number weighting).

- Since the equation above does not provide a complete description of the entire merging history tree, one needs to compute the probability that an M_0-clump at the epoch b_0 was previously in n subclumps at the epoch b_1, of which there were n_1 single particle subclumps, n_2 with two particles, n_j with j particles and so on. This joint probability distribution $p(\vec{n}, b_1|M_0, b_0)$ was derived by Sheth (1996) in the particular case of Poisson distribution.

- In SL99 it was demonstrated that the above probability can follow from the assumption that mutually disconnected regions within a Poisson distribution are mutually independent. This means that if we associate a certain volume V_{M_1} to the first subclump within V_{M_0}, the remaining particles $R = M_0 - M_1$ must be randomly distributed within the remaining volume $V_{M_0} - V_{M_1}$. In the next section we will see how this condition reflects on a correction to be applied to the overdensity at which the new progenitors are drawn. The above argument can be generalised to partition haloes associated with Gaussian initial fluctuations, and this is the starting point of our algorithm.

3.4 Our algorithm

The algorithm of SL99, following from the above considerations, was demonstrated to be exact for a white-noise power-spectrum, but needs some modifications in order to be applied to a more realistic ΛCDM spectrum.

Suppose to partition an halo of mass M_0 into subclumps by choosing first one subclump and then another one from the remaining mass and so on until the remaining mass falls below a certain minimum mass that is our mass resolution M_{res}. Therefore the halo of mass M_0 is the parent and the subclumps are the progenitors, note that in

this terminology the parent is younger than its progenitors. We have a probability of finding the first progenitor of mass M_1 given by $f(M_1, \delta_{c1}|M_0, \delta_{c0})$ (equation 2.35) and we choose a mass drawing a random number from this distribution. We can consider the halo M_0 as a region of size $V_{M_0} = M_0 b_0/\bar{n}$, where $b_0 = 1/(1 + \delta_{c0})$ and $\bar{n}$ is the average density. If the first progenitor has mass M_1 it occupies a volume $V_{M_1} = M_1 b_1/\bar{n}$. The remaining mass $R = M_0 - M_1$ is distributed in the volume $V_R = R b_R/\bar{n}$ and for the conservation of the volume the density in this region is given by

$$\delta_{cR} = \delta_{c1} - \frac{(\delta_{c1} - \delta_{c0})}{1 - (M_1/M_0)} \tag{3.7}$$

(see equation 5 of SL99). Now, the second progenitor must be chosen from the remaining mass R and the probability that it has mass M_2 is given by $f(M_2, \delta_{c1}|R, \delta_{cR})$. Note that we are updating the initial overdensity and not the final one, but for the case of a constant barrier, only the difference between the two barriers is important, hence updating the initial or the finale overdensity does not change results. Therefore we chose a random number from this new distribution. Then we iterate the process continuing to find progenitors until the remaining mass is below the mass resolution.

The assumption that disconnected volumes are mutually independent is right only for white noise power spectrum, but we want to build merger trees for a ΛCDM spectrum. SL99 show that applying the same algorithm for scale-free spectra with $n \neq 0$ leads to inconsistencies in the excursion set mean values. Since we know that all the excursion set quantities are independent on the power spectrum when they are expressed in terms of the variance rather than the mass we run the algorithm for the white-noise case. Then we consider each chosen M_{wn} not as a progenitor with mass M_{wn}, but as a region populated by some number ν of objects having mass $M_{\Lambda CDM}$. The value of $M_{\Lambda CDM}$ is obtained requiring that $S(M_{\Lambda CDM}) = S(M_{wn})$, where $S(M_{wn}) = S_0 M_0/M_{wn}$ and $S_0 = S_{\Lambda CDM}(M_0)$ is the mass variance corresponding to the parent halo mass in the ΛCDM power-spectrum. In this way we normalise the white-noise power spectrum in such a way that the mass variance of the two spectra is the same in M_0. As shown in Figure 3.1 the white-noise masses for a given S are much greater than the ΛCDM ones, so once we have normalised the white-noise power spectrum to the ΛCDM one at M_0 we obtain a number of progenitors $\nu > 1$. Although ν is a real number, we approximate it to the nearest integer value, in order to obtain an integer number of progenitors. This is particularly helpful when we will generate the complete merging history of a given halo, and we will split each new progenitor in further progenitors.

In order to generate a Gaussian random variable we choose to build a random walk starting from (S_0, δ_{c0}). To construct a trajectory we compute the value of δ_c at a discrete value of S, computed using a step ΔS which must be small enough that an upcrossing of the barrier is rare in this step (see section 3.6 for a discussion on the effects of walk resolution). We have found that for obtaining a good accuracy in the conditional mass functions at any given redshift we have to use $\Delta S = 1\times10^{-4}(\delta_{c1}-\delta_{c0})$. Then we draw a random variable δ_c from a Gaussian distribution with zero mean and variance equal to $\sqrt{S}$. Steps on the S-axis and δ-axis are hence correlated. In the

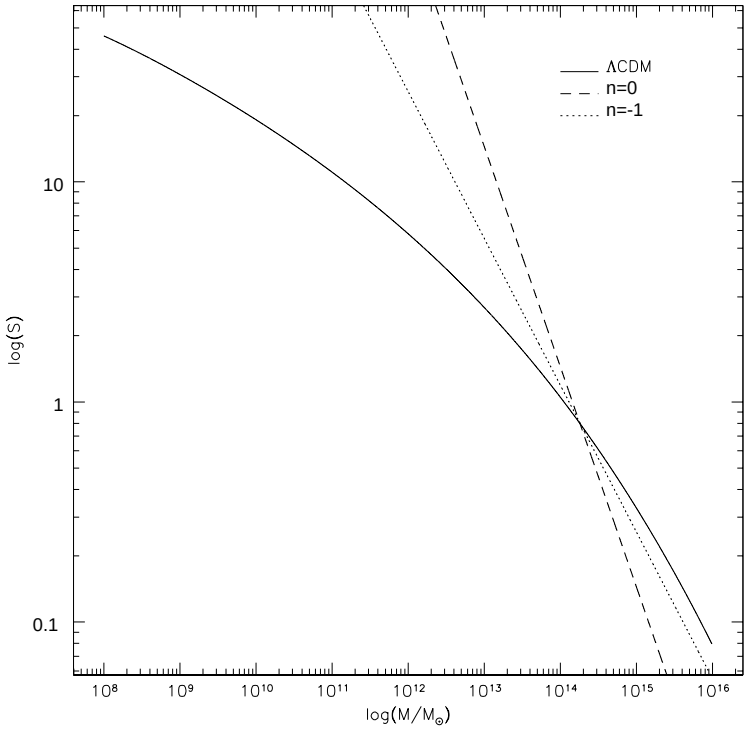

FIGURE 3.1— Mass variance as a function of mass for different power spectra: ΛCDM (solid line), white-noise (dashed line) and scale-free with $n = -1$ (dotted line). The normalisation is such that the curves cross at M_0, that is the parent halo mass for which progenitors are needed.

case of the spherical collapse the form of the barrier is constant and is equal to δ_c and the value of S at the first upcrossing of the barrier is the mass variance of the new progenitor, from which using a ΛCDM power-spectrum we extract the mass. In Figure 3.2 we show some examples of random walks which upcross the barrier, the left hand panels are for a constant barrier. In the top panel the final barrier height is fixed $\delta_c = 1.675$ while in the bottom one it is the final barrier to be fixed. In the case of constant barrier fixing the initial or final barrier lead to identical results because the interval of δ_c is constant.

With the same algorithm we also treat the ellipsoidal collapse where the shape of the barrier is no more constant but it depends on the mass variance. We adopt the barrier shape proposed by Sheth et al. (2001):

$$B(S, \delta_c) = \sqrt{a}\delta_c(1 + \beta(a\nu)^{-\alpha}) \tag{3.8}$$

where $\nu = \delta_c^2/S$ (note that this is a different variable from the number of progenitors defined above with the same symbol). The parameters α, β, a determine the shape of the barrier. For ellipsoidal collapse we use: $\alpha = 0.615, \beta = 0.485, a = 0.75$. We

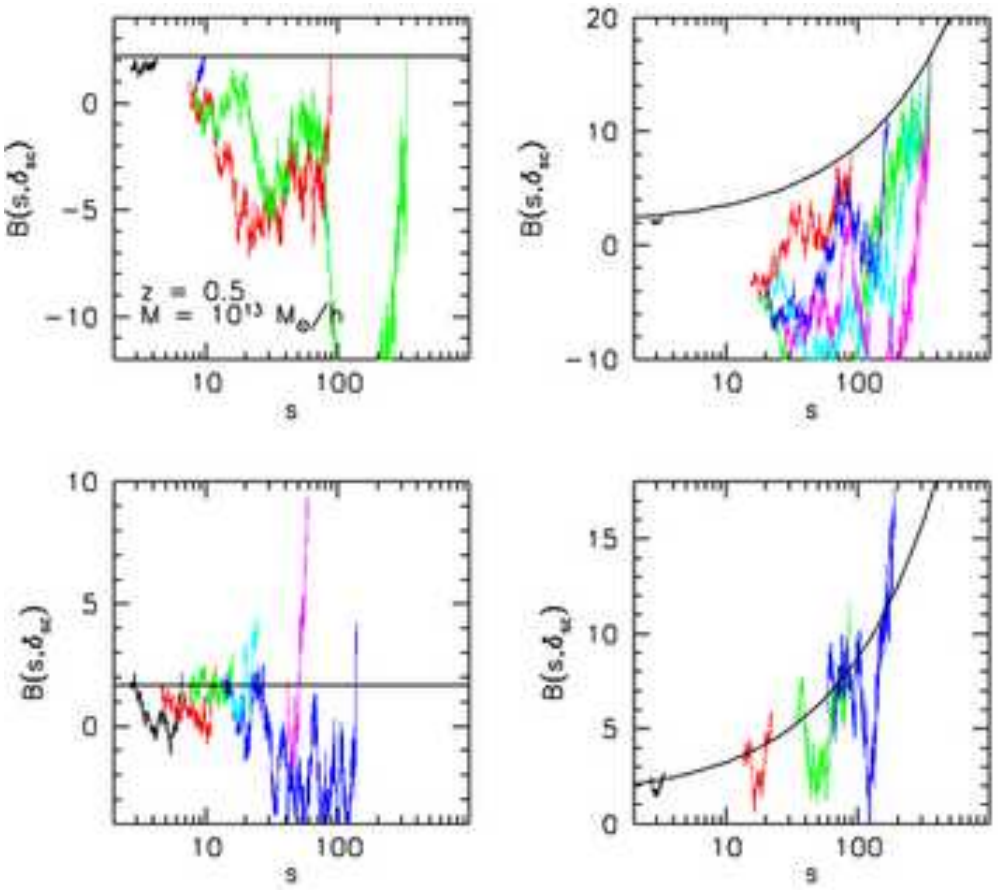

FIGURE 3.2— Examples of random walks which upcross the barrier in the case of spherical collapse (*left panels*, constant barrier) and ellipsoidal collapse (*right panel*, moving barrier).

compute the upcrossing of the barrier in two ways. In the first approach we do exactly the same as spherical case, so we fix the final height of the barrier and we change the initial one according to $\delta_{c0} = \delta_{cf} - (\delta_{c1} - \delta_{c0})/(R/M)$. We have found that this method is not successful in reproducing the correct number of progenitor for all the progenitor masses. So we tried with a second approach, that is to fix the initial barrier and to move the final one: $\delta_{cf} = \delta_{c0} + (\delta_{c1} - \delta_{c0})/(R/M)$. We have find that while for the constant barrier case the two methods are identical, in the case of moving barrier (that is barrier dependent on the mass) they lead to very different results. In the right-hand panels of Figure 3.2 we show random walks for a moving barrier, which show a strong dependence on the mass variance. We notice that fixing the initial or the final barrier can lead to very different path of the trajectories, since the height of the barrier for different values of S is very different in the two cases.

3.5 Conditional Mass Functions

In this sections we compare the resulting Conditional Mass Functions (CMF) from our algorithm with the analytical predictions. As a criterion to test the consistency of our merger tree, we check if it reproduces the EPS conditional mass function $f(M_1, z_1|M_0, z_0)$ exactly for any set of M_1, z_1, M_0, z_0. Both shape and normalisation are required to fit to the theoretical expectations. It was demonstrated by Zhang et al. (2008), that this is a necessary and sufficient condition to reproduce the desired CMF at any look-back time. In fact the progenitor mass function can be written as:

$$f(M, z|M_0, z_0) = \int_M^{M_0} dM' f(M, z|M', z') f(M', z'|M_0, z_0) \tag{3.9}$$

If we take $z' = z_0 + \Delta z$ and $z = z_0 + 2\Delta z$, that is, $z0$ and z' are two consecutive timesteps and the same for z' and z, we see that equation 3.9 implies that if each progenitor mass function is in perfect agreement with the EPS predictions for two consecutive timesteps, even the CMF with timestep $z - z_0$ should give the same good agreement with theoretical EPS.

For this reason we verified that our algorithm correctly reproduces the progenitor distributions for different parent halo masses and for different redshift, using only one time-step. In Figure 3.3-3.4 we show results for the spherical collapse case for two parent halo masses, $M_0 = 5 \times 10^{12} M_\odot$ and $M_0 = 10^{11} M_\odot$, and for different timesteps as indicated. The histograms are the average over 10000 Monte Carlo realizations and solid lines are the Extend Press-Schecter predictions. In some cases we need to run more realizations for the smaller timesteps, because the distributions, mainly in the low-mass part, are more noisy.

The mass resolution is taken as $M_{res} = 10^{-4} M_0$, but we checked that the consistency holds even for much lower mass resolution. Our Monte Carlo realisations produce CMF that are in well agreement with the theoretical expectation up to very high look-back times. Only in some cases, we do not have a perfect match of the mass function at masses very close to the parent mass. We argue that this small discrepancy may be due to the approximation done in transforming the white-noise mass in a discrete number of ΛCDM masses.

With the same algorithm we also treat the ellipsoidal collapse model where the shape of the barrier is no more constant but it depends on the mass variance. We adopt the barrier shape proposed by Sheth et al. (2001), equation 3.8.

We show the resulting CMFs in figure 3.5-3.6 and we compare them with the ST predictions:

$$f(S_1, \delta_{c1}|S_0, \delta_{c0}) = \frac{\left|T(S_1|S_0)\right|}{\sqrt{2\pi(S_1 - S_0)}} \exp\Big(- \frac{(B(S_1) - B(S_0))^2}{2(S_1 - S_0)}\Big) \frac{dS_1}{S_1 - S_0} \tag{3.10}$$

where

$$T(S_1|S_0) = \sum_{n=0}^{5} \frac{(S_0 - S_1)^n}{n} \frac{\partial^n (B(S_1) - B(S_0))}{\partial S_1^n} \tag{3.11}$$

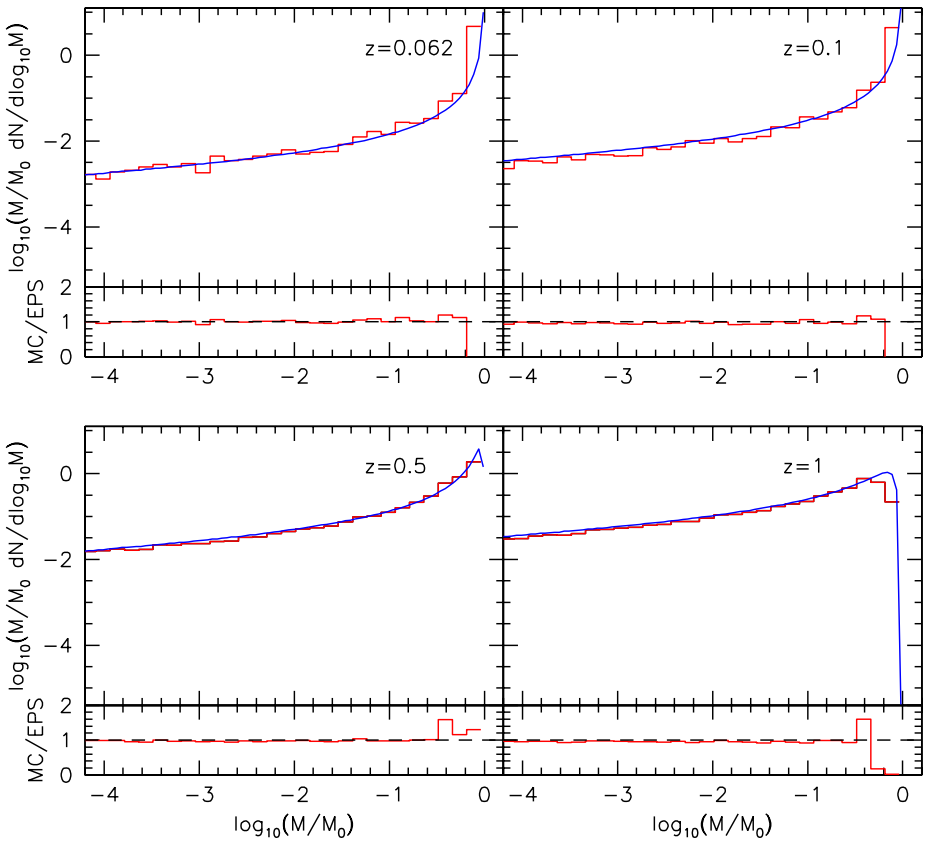

FIGURE 3.3— Conditional Mass Function for a parent halo mass $M_0 = 5 \times 10^{12} M_\odot$ for 4 redshifts as labelled. Red histograms represent the Monte Carlo trees, averaged over 10000 realisations, while the blue lines are the EPS predictions. In the small boxes of each panel, it is shown the ratio between the Monte Carlo CMF and the theoretical one.

and B is the barrier as given in equation 3.8.

Even in this case we achieve an overall well agreement, except for low-mass progenitors at very low redshift (see panel (a)). We check that the underprediction of the low-mass end does not depend on resolution of the walk or of the tree.

As shown by Zhang et al. (2008), hereafter Z08, the Taylor-series-like approximation for the ellipsoidal CMF given by ST is valid and works very well only for large timesteps, but is invalid for small timesteps, with $\Delta z \lesssim 0.1$, because it overpredicts the number of progenitors at small look-back times.

The authors derived a new analytic expression for the progenitor mass function of

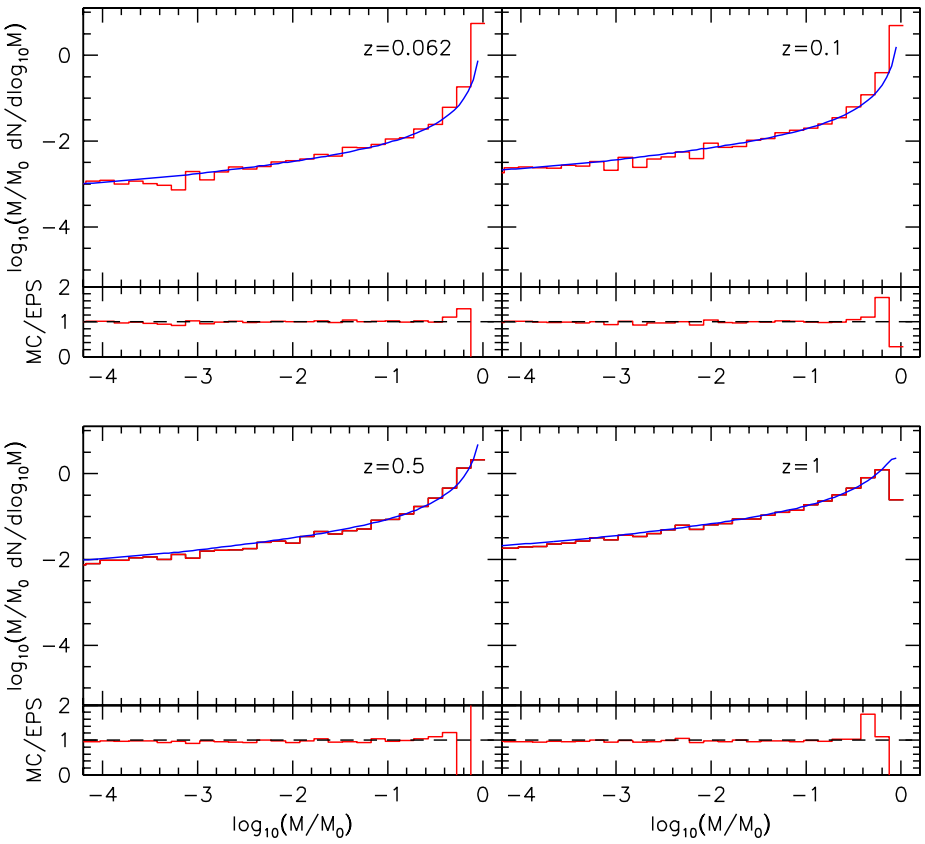

FIGURE 3.4— The same of figure 3.3 but for a parent halo mass $M_0 = 10^{11} M_\odot$

ellipsoidal model for small timestep using the same shape of the barrier used by ST (eq.3.8) obtaining the following expression:

$$f(S_1, \delta_{c1}|S_0, \delta_{c0}) = \frac{b_0}{(S_1 - S_0)\sqrt{2\pi(S_1 - S_0)}} \exp\left[-\frac{(b_0 + b_1(S_1 - S_0))^2}{2(S_1 - S_0)}\right] - \frac{b_0 b_2}{4} \exp\left(-\frac{b_1^2(S_1 - S_0)}{2}\right)\left[1 + \frac{b_1\sqrt{(S_1 - S_0)}}{\Gamma(3/2)}\right] + O(b_0^2)\,. \quad (3.12)$$

where $b_0 = (\delta_{c1} - \delta_{c0}A_0$, $b_1 = A_1/\sqrt{S_0}$, and $b_2 = -4A_2/[2\pi S^3(M_0)]^{1/2}$, whith $A_0 = 0.866(1 - 0.133\nu_0^{-0.615})$, $A_1 = 0.308\nu_0^{-0.115}$, $A_2 = 0.0373\nu_0^{-0.115}$, $\nu_0 = \delta_{c0}^2/S_0$. The second term on the right hand side of eq. (3.12) is a new term that is absent in the Taylor series approximation proposed by ST.

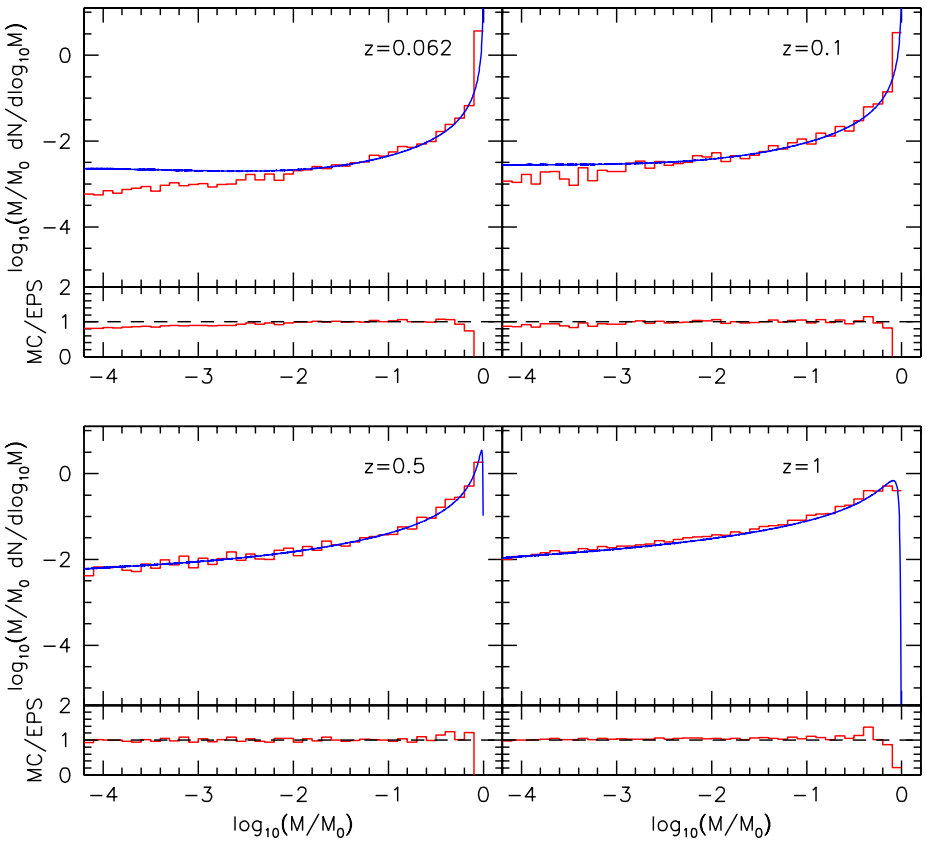

FIGURE 3.5— Conditional Mass Function in the ellipsoidal case for a parent halo mass $M_0 = 5\times10^{12} M_\odot$. Solid lines are the ST predictions (eq. 3.10).

Actually, the discrepancy between our MC and the ST model rise exactly in the timesteps with $\Delta z \lesssim 0.1$, where the analytical predictions fail. In figure 3.7 we compare the CMF resulting from the MC tree with both ST and Z08 predictions, in the first two timesteps. We note that the Z08 approximation leads to a smaller contribution to the conditional mass function by low-mass progenitors, and lies closer to our Monte Carlo CMF, although a discrepancy is still present.

3.6 Effects of the resolution

Although we demonstrated that our merger tree works extremely well, it is worth to note that a great caution has to be taken in imposing the mass resolution limit in the random walk. There are two limits that are to be chosen. The first one is the amplitude

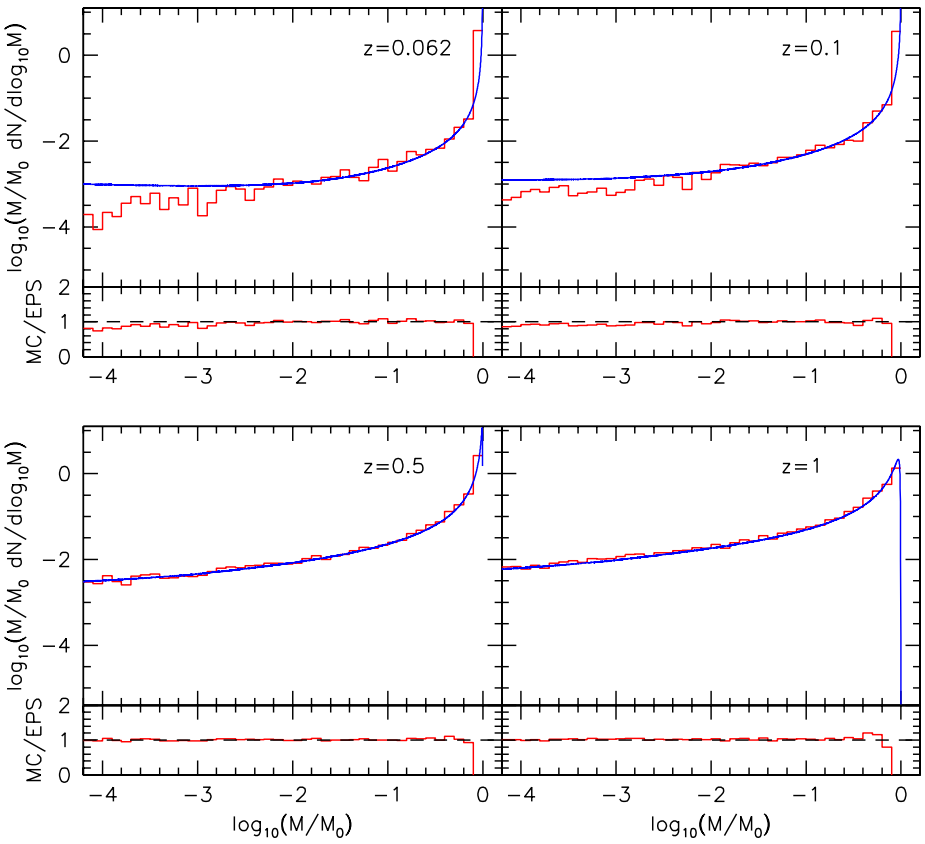

FIGURE 3.6— The same of figure 3.5 but for a parent halo mass $M_0 = 10^{11} M_\odot$.

of the step in the x direction, that is in the mass variance axis. This value has to be fixed to the lowest value possible, in order to avoid an overestimation of the mass variance at which the walk upcrosses the barrier, leading in that case to an underestimation of the mass. Of course, smallest the amplitude of the step, greater is the time spent by the walk before the upcrossing, increasing the computational time. The second limit to be chosen is the maximum number of steps to be done by the walk before the upcrossing. The maximum number of walks determines the maximum S that can be reached, or in other words, the minimum progenitor mass. This has to be taken as high as possible, in order to avoid a overabundance of progenitors of that mass, and to an underestimation of the remaining mass, that is updated at each random walk upcross.

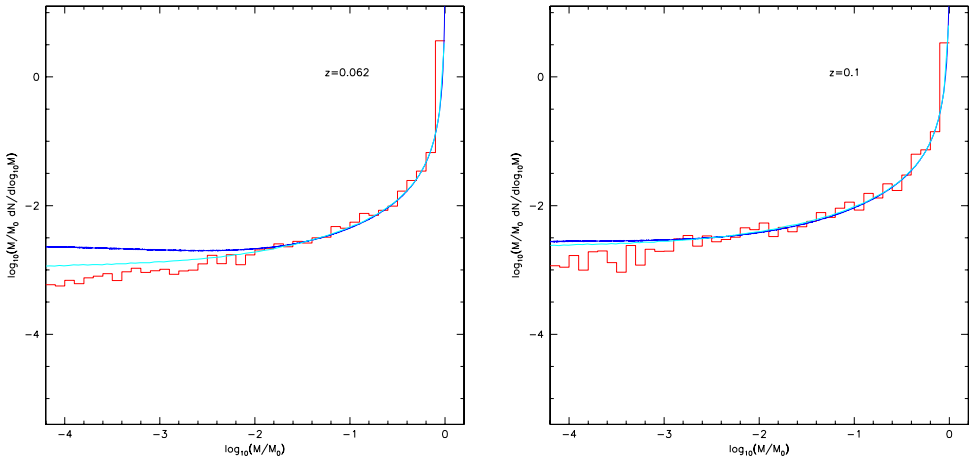

FIGURE 3.7— Comparison between the CMF from our MC merger tree (red histogram)and two analytical predictions: ST (blue line) and Z08 (cyan line) for the the ellipsoidal model, for two timesteps and for $M_0 = 5 \times 10^{12} M_\odot$.

3.7 Comparison with N-body simulations

We compare the results from Monte Carlo predictions with cosmological N-body simulations. We make use of the GIF2 simulation, from Gao et al. (2004), having a periodic cube of size $110 Mpc/h$, with the same ΛCDM cosmology that we used for the MC tree. The simulation contains 400^3 Dark Matter particles, with mass $1.73 \times 10^9 M_\odot$. Halo finder and tracking of the merging history tree are described in Giocoli et al. (2008). Haloes are resolved with a minimum of 10 particles, that means that the minimum resolved mass is $1.73 \times 10^{10} M_\odot$.

In figure 3.8 we show the comparison between conditional mass function of the MC trees for both barrier models (histograms), the analytic predictions (solid lines) and the one from N-body simulations (squares) for a parent halo mass equal to $5 \times 10^{12} M_\odot$).

Of course, the N-body simulations can not probe the progenitor mass function down to our mass resolution (that is $5 \times 10^8 M_\odot$), and are complete only down to $\sim 10^{10} M_\odot$. In the mass range well probed by N-body simulations we can see that the ellipsoidal model better reproduces the progenitor mass function, for all the redshift probed, while the spherical collapse model (EPS) always gives an overabundance of low-mass progenitors.

3.8 Unconditional Mass Function

In order to implement a semi-analytical model on our merger tree, we need to build a complete tree. So far we have described how to partition a halo into progenitors at a chosen redshift, but in order to implement a semi-analytic model of galaxy formation,

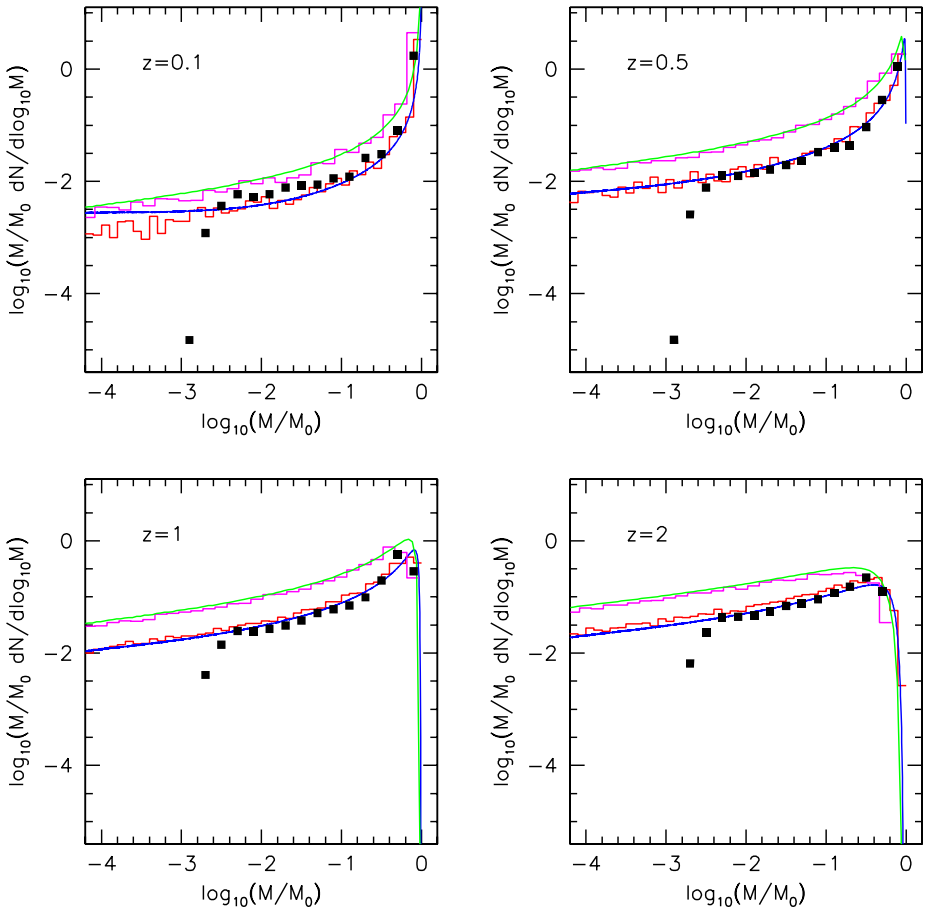

FIGURE 3.8— Comparison between progenitor mass function computed in different ways. Black squares show the N-body simulation CMF, histograms the MC tree results (red for the ellipsoidal collapse model and magenta for the spherical model), while solid lines show the analytic predictions, blue for ST and cyan for EPS expressions.

we need to know the complete hierarchy of a given parent halo, and, hence, to split each progenitor into new progenitor until all of them fall below the mass resolution chose.

For this reason, we need to create a grid in redshift and to track back the merging history of the present-day halo, at any chosen redshift. We consider a grid of 52 redshift, ranging from $z = 0$ to $z = 49$, with a variable time interval of $100 - 300 Myr$. We chose this grid in time, because is the same at which we have the snapshots of the N-body simulations described in the previous Section . Actually, we usually don't track the hierarchy of a given halo up to the highest redshift possible because the progenitor

mass falls below the mass resolution at much lower redshift. Progenitors which fall below the resolution are considered accreted mass, their merging history is no more followed, but they are stored.

After that we chose a grid of 35 parent halo mass, ranging from $3^{10}M_{\odot}$ to $10^{15}M_{\odot}$, with masses logarithmic spaced, and we generate 100 realizations of the tree for each parent. In this case we fix the mass resolution to $M = 10^{10}M_{\odot}$ for all the parent involved.

As a further test for our algorithm we compute the unconditional mass function for our grid of merger trees. In order to compute it we first compute the progenitor mass function at a given redshift for a certain halo, and weight it for the number density of haloes existing at $z = 0$, according to the analytical expectations (PS or ST), and then summing over all the spectrum of parent halos chosen. This gives the global mass function at a given redshift, and it has to be compared to the PS predictions (eq. 2.30) or ST unconditional mass function (eq. 2.33). We show them in figure 3.9: the MC mass function reproduce exactly the analytical one, for the spherical collapse as well for the ellipsoidal collapse. Note that in the previous section we saw that the CMFs for the ellipsoidal collapse case turn out to be in disagreement with the ST expectations for small progenitor mass and very small timesteps. Nevertheless, here we do not obtain any disagreement, when we integer over the full spectrum of masses. The reason is due to the fact that the underprediction of progenitors rises from masses $\sim 10^{-2} - 10^{-3}M_0$. According to our mass resolution we are able to find progenitors of 2 or 3 order of magnitude smaller than their parent, only for $M \gtrsim 10^{13}M_{\odot}$, that are haloes quite rare according to Press-Schecter number densities and the contribution to the low-mass end of the mass function mainly come from low-mass parent haloes. Hence, the underprediction of the CMF in the low-mass range does not affect the global mass function.

3.9 Summary

In this Chapter, we have presented our algorithm for partitioning a parent halo into progenitors. This is based on the approach proposed by Sheth & Lemson (1999), but it is build in a completely independent way. In particular it is successfully extended to the case of ΛCDM power-spectrum. It is further improved in order to be used for different shapes of the barrier, namely constant and mass-dependent, since it is based on the upcrossing of the barrier in the random-walk approach. We are able to reproduce the mean statistical quantities predicted by the theoretical predictions, in the case of spherical collapse (constant barrier) and ellipsoidal collapse (moving, or mass-dependent barrier) model. Some discrepancies in the low-mass end of the progenitor distribution with the theoretical one still exist, although we demonstrated that a recent computation of this quantity (Z08) lies closer to our Monte Carlo results than the "classical" Sheth-Tormen (2002) prediction, indicating that part of the problem may be due to a lack of a correct approximation for the analytical derivation of this quantity more than in the numerical algorithm. We have also generated the complete merger

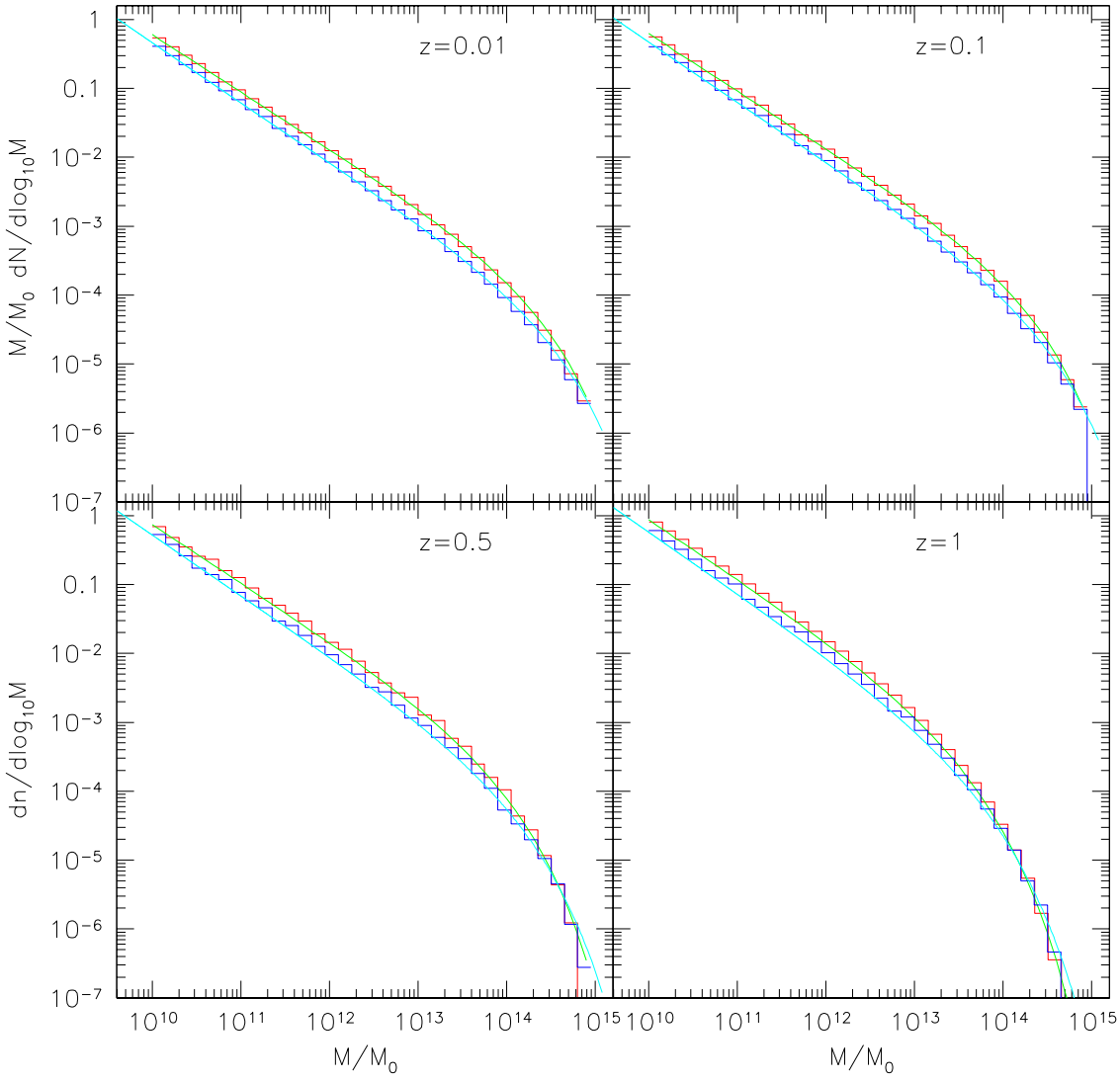

FIGURE 3.9— Unconditional mass function for different redshifts for spherical and ellipsoidal models. Histograms show 100 Monte Carlo realizations for the spherical (red) and ellipsoidal (blue) case, while solid lines represent the PS (green) and ST (cyan) predictions. Parent halo masses range from $10^{10} M_{\odot}$ to $10^{15} M_{\odot}$.

tree, splitting each progenitor into new progenitors, until all the progenitors fall below a given mass resolution, for a grid of parent halo masses. The resulting mass function is in perfect agreement with the theoretical expectations. In the following Chapter we

will refer to this merger tree in order to implement the semi-analytical model.

We will make use of the classical EPS-based merger tree, leaving for a future work the comparison between semi-analytical predictions based on different merger trees (spherical model, ellipsoidal model, and N-body trees).

4

GECO: Galaxy Evolution COde

In this Chapter we describe the prescriptions used to build the Galaxy Evolution COde (GECO) that we used to model galaxy formation. These are the cooling of the gas, the star formation process, which can occur in a quiescent mode or in a bursty mode, the feedback due to SN, reionization and AGN, and the mechanisms leading to galaxy mergers, namely dynamical friction and satellite collisions.

4.1 Introduction

Semi-analytic Models (SAM) of galaxy formation couple a Monte Carlo representation of the hierarchical clustering of dark matter haloes with analytical recipes for the physical processes involving baryons. In recent years, even SAM implemented on trees from N-body simulations have become popular, and are sometimes referred to as "hybrid" models. Although the hierarchical structure formation theory has a number of successes in predicting large scale structures in the universe and CMB observations, the physics of baryons is still highly uncertain, and requires the treatment of such process only through parametric form, with the introduction of some free parameters in the model, that can only be set through a comparison of the models with observational data in the local universe. They only represent our lack of knowledge in understanding the physics of galaxy formation, and even if they are set fitting results with observations, only a limited range of values is possible in order to give a reasonable agreement over a large set of observables.

The semi-analytic approach has its root in the work of White & Rees (1978), where it was proposed that galaxy formation is a two stage process, with dark matter haloes forming in a dissipationless gravitational collapse and galaxies forming inside them following the radiative cooling of baryons. Although WR78 and, after, White & Frenk (1991) based their work only on the analytic PS theory, predicting only average quantities, subsequently a number of works followed their prescriptions using Monte Carlo

merger trees (Kauffmann et al. 1993; Cole et al. 1994; Baugh et al. 1996; Kaufmmann et al. 1999; Cole et al. 2000; Menci et al. 2002, 2004, 2005 among others) and N-body simulation (Hatton et al. 2003; Croton at al. 2006; De Lucia et al. 2004, 2006).

In the following we will describe our new SAM model, that is based on a MC tree. At variance with other models of galaxy formation we tested our results directly on the observables involving stellar mass more then luminosities, with the aim of avoiding to introduce further uncertainties in the model due to the spectro-photometric synthesis, dust extinction and Initial Mass Function. This second, complementary approach will be deferred to a future work.

4.2 Linking Galaxies to Dark Matter Haloes

As described in the previous Chapter, the generation of the merger tree proceeds backwards in time. We start from the initial redshift (typically $z = 0$) and we split each halo in progenitors, existing at higher redshift. On the contrary, galaxy formation is modelled forwards in time, starting from the "leaves" of the tree, i.e. haloes at high redshift, whose progenitors fall below the mass limit resolution ($M_{res} = 10^{10} M_{\odot}$ in this case) and their hierarchy is no more followed in time. Starting from each of these haloes we put baryons inside them, according to the baryonic fraction observed by WMAP3: $f_b = \Omega_b/\Omega_m = 0.16$. (Spergel et al. 2007)

We use the grid of 35 parent halo mass, and 52 timestep, described in Section 3.8 and we generate several realizations for each tree. In order to derive statistical quantities such as mass function, or SFR density, we simply make a weighted sum over the model galaxies. Since we are dealing with an EPS merger tree, for consistency, we use as a weight, the number density of haloes given by the PS mass function. In some cases, we checked results using a ST number density, which fit the results of N-body simulations with higher accuracy, but we found that it makes little difference.

In the following section, we will describe the baryonic processes at work in driving the evolution of galaxies, starting from the cooling of the gas.

4.3 Cooling

The cooling of the gas is a fundamental process for galaxy formation, as it sets the rate at which gas becomes available for star formation. The first to invoke the need of some dissipative process occurring inside dark haloes were White and Rees (1978), in order to explain the difference between the luminosity function of galaxies, with a characteristic mass and size, and the halo mass function, resembling more a power-law, lacking any preferred scale. They argued that galaxy formation is a two stage process, with dark matter haloes forming through the dissipationless hierarchical clustering, and gas cooling inside them.

Gas is assumed to be heated by shocks during the violent relaxation to the virial temperature of the halo, given by:

$$T_{vir} = \frac{1}{2}\frac{\mu m_H}{k} V_c^2 \tag{4.1}$$

where μ is the mean molecular mass of the gas, m_H is the mass of a hydrogen atom and k is the Boltzmann's constant and V_c is the circular velocity of the halo.

The rate at which gas can cool depends upon this temperature, which determines its ionization state, and on the metallicity of the gas, that is the chemical composition. We take the cooling rate tabulated by Sutherland and Dopita, 1993 (hereafter SD93). They considered several mechanisms through which gas can cool. The most important mechanism for galaxy formation are the emission of photons following transitions between energy levels. Collisions between partially ionized atoms and electrons excite the atoms to higher energy levels and the energy irradiated during the decaying allows the gas to cool. This process is important for haloes with intermediate masses, that is for $10^4K < T_{vir} < 10^6K$. The second mechanism is the free-free emission from electrons accelerated in an ionized plasma, and this is the dominant process for massive haloes ($T_{vir} > 10^6K$). We ignore the inverse Compton scattering of CMB photons by electrons in the hot halo gas because it is important only at very early times ($z > 10$) and also the excitation of rotational and vibrational energy levels in the molecular hydrogen because it is important only for low mass haloes ($T_{vir} < 10^4K$).

It is possible to define a cooling rate per unit volume, given by:

$$L = \Lambda(T, Z)\rho_{gas}^2 \tag{4.2}$$

where $\Lambda(T, Z)$ is the cooling function defined by SD93, shown in Fig. 4.1 as a function of temperature and for different value of metallicity. The two peaks of the function for primordial gas are due to the decay following the excitation of ionized atoms of Hydrogen ($T = 15000K$) and Helium ($T = 100000K$). In the case of enriched gas at intermediate temperature the cooling is enhanced, at $T \sim 100000K$ the strong peak is due to Oxygen, and the small peaks at higher temperatures are due to heavier elements. For high temperatures ($T > 10^6K$ for primordial gas and $T > 10^7K$ for enriched gas) the cooling rate increases as $T^{1/2}$ due to free-free radiation, that is the dominant cooling mechanism for a plasma. As we do not follow the chemical enrichment of the gas, in the following we assume that gas has subsolar metallicity: $Z = 0.3Z_\odot$.

The cooling time is defined as the thermal energy density divided by the cooling rate per unit volume:

$$t_{cool} = \frac{3}{2}\frac{\rho_{gas}kT}{\mu m_H}/\Lambda(T, Z)\rho_{gas}^2 \tag{4.3}$$

where ρ_{gas} is the gas density profile, which is assumed to be isothermal:

$$\rho_{gas}(r) = \frac{M_{hot}}{4\pi R_{vir} r^2} \tag{4.4}$$

where M_{hot} is the total gas mass in the hot component, which is assumed to extend to the virial radius. A cooling radius can now be defined as the point where the local cooling time is equal to the age of the universe:

$$t_{cool}(r_{cool}) = t_U(z) \tag{4.5}$$

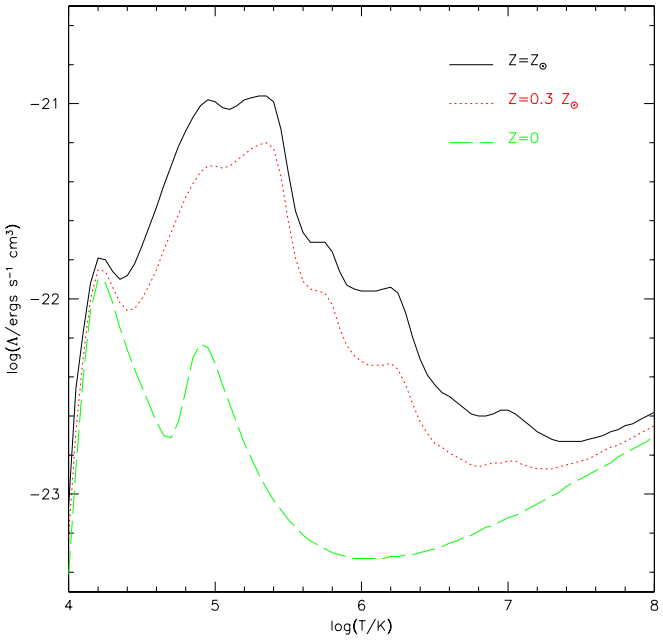

FIGURE 4.1— Cooling function as a function of virial temperature of the halo, as tabulated by SD93. Solid lines are for different values of the metallicity: $Z = Z_{\odot}$ (solid black line), $Z = 0.3 \times Z_{\odot}$ (dotted red line), $Z = 0$ (green dashed line).

We can now compute the rate at which gas accretes to the centre of the halo, becoming available for star formation. Following the standard paradigm of White & Frenk (1991) we distinguish two regimes of cooling, depending on the value of r_{cool}. In the first case, we consider $r_{cool} > R_{vir}$, hence the cooling radius lies outside the virialized region of the halo. The cooling is so rapid that the infalling gas never reaches hydrostatic equilibrium and the supply of cold gas for star formation is limited by the infall rate rather then the cooling rate. We assume that all the hot gas in the halo will settle to the centre in a timescale given by the halo dynamical time (R_{vir}/V_c):

$$\dot{M}_{cool} = \frac{M_{hot} V_c}{R_{vir}} \tag{4.6}$$

This regime of cooling was called by White & Frenk (1991) rapid cooling regime, also known as cold mode. As demonstrated by high-resolution simulations (Forcada-Mirò & White, 1997) the post-shock gas cools in less than one sound crossing time and cannot keep the pressure needed to support an accretion shock at large radius. At this point the gas moves inward, increasing the post-shock temperature and decreasing the mass of the atmosphere of hot gas.

The second way of infalling is the static hot halo regime, or hot mode, that occurs when the cooling radius lies inside the virial radius. In this case, the gas inside r_{cool}

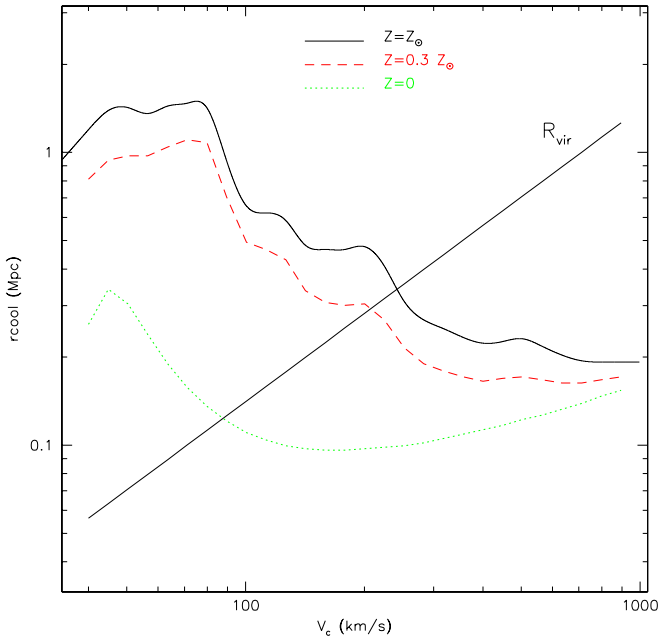

FIGURE 4.2— Cooling radius as a function of circular velocity of the gas. Color are encoded as in figure 4.1. Solid black line represents the behaviour of the virial radius with circular velocity.

will be pressure-supported and will contract quasi-statically toward the centre. Cooling will cause a flow of gas toward the centre in a way exactly analogous to the cooling flow occurring in galaxy clusters. A simple expression for the infall rate is given by:

$$\dot{M}_{cool} = 4\pi\rho_{gas} r_{cool}^2 \frac{dr_{cool}}{dt} \tag{4.7}$$

In Figure 4.2 the behavior of the cooling radius and the virial radius with the virial velocity are illustrated for different metallicities. For small haloes (that we find preferentially at early times), the cooling radius is greater than the virial radius, and we are in the cold mode regime, where equation 4.6 applies. At late times, for large values of the virial velocity, the cooling radius falls below the virial radius and we are in the hot mode regime. Hence, at high redshift we have a more efficient cooling.

In order to test the validity of the assumption at the basis of cooling recipes in SAM techniques, several authors in literature made a comparison of several properties of the gas distribution between SAM models and SPH (Smoothed Particle Hydrodynamics) simulations. For example Benson at al. (2001) compare SPH results with the one of a semi-analytic model that mimics the conditions of the SPH simulation as close as possible, using similar dark matter haloes distributions, the same resolution limit, and with star formation and feedback prescriptions stripped out. They found an high level of consistency in the statistical properties of the outcomes of the two models,

such as the fraction of gas in different phases, the gas mass function, and the spatial distribution of galaxies. In Yoshida et al. (2002) and Helly et al., (2003) an object-by-object comparison leads to similar conclusion, giving reasonable agreement between the cooling model described above and their SPH simulations.

4.4 Galaxy sizes

Since several time-scales involved in the analytic recipes (such as for example the star formation rate) that we are going to introduce in the following sections depend on the dynamical time of the disk ($t_{dyn} = r_{disk}/v_{disk}$), it is important to have an accurate description of the size of galactic disk. The disk size of course, will depend on the virial radius of the halo where the galaxy was born, and on its angular momentum. In fact, if the halo is asymmetric and surrounded by a clumpy distribution of matter, then it can acquire an angular momentum from a net tidal torque. To quantify its angular momentum, one often refers to the spin parameter, which is a dimensionless quantity, defined as follow:

$$\lambda = \frac{J|E|^{1/2}}{GM^{5/2}} \tag{4.8}$$

where J,E and M are the total angular momentum, energy and mass of the halo. The distribution of the spin parameter observed in N-body simulations (Warren et al., 1192; Cole & Lacey 1996) can be approximated with a lognormal distribution with $< \lambda >= 0.05$ and $\sigma_\lambda = 0.5$. Hereafter we will assume the mean value for λ. Mo, Mao and White (1998) related the disk radius to the spin parameter and to the virial radius assuming that the angular momentum of the disk is a fix fraction of that of the halo:

$$r_{disk} = \frac{1}{\sqrt{2}}\Big(\frac{j_d}{m_d}\Big)\lambda R_{vir} \tag{4.9}$$

where m_d is the ratio between the disk mass and the halo mass, and j_d is the ratio between the angular momentum of the disk and of the halo. Higher values for the spin parameter result in larger disks, because they contract less before reaching the centrifugal equilibrium. The above relation holds in the case of haloes approximated with isothermal profile and neglecting the gravitational effects of the disks themselves, but the authors also give the correct expression in the case of NFW profiles and self-gravitating disks. As shown by MMW98, it is a reasonable assumption to take $j_d = m_d$, which gives us:

$$r_{disk} = \frac{\lambda}{\sqrt{2}} R_{vir} \tag{4.10}$$

which leads to galactic disk that are over an order of magnitude less extended than their halo hosts. Under the assumption that we are considering negligible the self-gravity of the disk, the disk circular velocity is equal to the halo virial velocity.

4.5 Star Formation

One of the major uncertainties in modelling galaxy formation concerns the process of star formation. Understanding star formation proceeds on several fronts. The first one concerns the first generation of stars, the population III stars, formed in a gas with primordial composition, it is still to be understood when and how they formed, and which mass they had. Another issue to be resolved is to explain the nature of the dominant processes which determine the mass of stars. It is not clear yet if this occurs in a "top-down" scenario, in which a gas cloud fragments and the sub-clouds collapse to form stars, or in a "bottom-top" scenario, according to which low-mass stellar cores acquire gas from the cloud (Elmegreen & Scalo 2004).

For all this reasons the only way to model star formation is in a parametric way, inserting free parameters. As common use among SAM models, we consider two modes of star formation. The quiescent mode, which involves the whole life of a galaxy at a modest rate, and the starburst mode, that is a violent episode of star formation induced by galaxy mergers.

Although the process of star formation results to be extremely complex on small scales, on global scale it can be easily approximated according to the observed Kennicutt law (Kennicutt 1998), according to which the star formation rate per unit area of a galaxy ($\dot{\Sigma}_*$) scales with a power $n = -1.4$ of the surface density of the cold gas (Σ_{gas}): $\dot{\Sigma}_* \propto \Sigma_{gas}^{-1.4}$. Assuming as a timescale the dynamical time of the galaxy allows to obtain a parametric form for the star formation in the quiescent mode. In this case, the star formation rate is simply assumed to be proportional to the amount of cold gas available, divided by a timescale of star formation, that here is assumed to be the dynamical time of the disk: $t_{dyn} = r_{disk}/v_{disk}$. The efficiency of the star formation process is set by the free parameter α. Therefore, the resulting star formation rate is given by:

$$\dot{M}_* = \alpha \frac{M_{cool}}{t_{dyn}} \tag{4.11}$$

Stars formed in the quiescent mode are added to the disk component of the galaxy. The idea behind this expression is that the dynamical time of the disk should take into account for the time taken by the gas, which is moving at the circular velocity of the disk, to move into the dense central part of the disk.

In the burst mode, the star formation is induced by a merger between galaxies, that can occur between the central galaxy and one of the satellites, or a collision between satellites. Both mechanism are assumed to induce a starburst. In this case, gas sinks to the central region of the galaxy and the increased density leads to an enhanced level of star formation (according to the Kennicutt law). Indeed, strong correlation between galaxy interactions and starburst activity are observed in the local universe (Kennicutt 1998; Sanders & Mirabel, 1996). As shown by N-body simulations (Mihos & Hernquist 1994; 1996), mergers involving two equal-mass systems lead to much more violent episode of star formation than unequal-mass mergers, while in the former case about 80% of the total gas supply (summed over the two merging galaxies) is

converted in stars in a period of time of $50 - 150 Myrs$, in the latter case only up to 50% of the gas is consumed in $\sim 60 Myrs$. According to the prescription of Somerville et al. (2001) we assumed that the star formation in burst is given by:

$$\dot{M}_* = f_{burst} \frac{M_{cold}}{t_{burst}} \tag{4.12}$$

where t_{burst} is the dynamical time of the largest disk, while the efficiency of the burst is given by:

$$f_{burst} = f_b \frac{m_1}{m_2} \tag{4.13}$$

where m_1 and m_2 are, respectively, the smallest and the biggest galaxy, and f_b is a free parameter. We assume that star formed during a starburst event are added to the bulge component.

4.6 Feedback

Feedback processes are mechanisms which regulate the efficiency of galaxy formation. The need of some form of feedback in low-mass haloes, which suppresses cold gas accretion, was first recognized by White & Reese (1978), in order to flatten in some way the faint-end of the luminosity function, which turned out to be too steep compared to the observational data available at the time. SN feedback and photoionization are commonly implemented in reducing the faint-end slope.

Although initially the motivation for invoking feedback was to suppress cooling, hence star formation, in low-mass haloes, in recent years the focus is shifted to reproduce the bright-end of the luminosity function, which in the most classical models results in an excess of bright objects compared with the observations (again a manifestation of the basic problem to shape an essentially power-law form for the DM mass function into a Schechter function for the baryons). Although the behaviour of the cooling function implies that cooling time increases in high-mass haloes, this is not enough to explain the sharp cut-off observed in the galaxy luminosity (or stellar mass) function, and some mechanisms which prevent the cooling rate in high-mass haloes is also needed and is commonly recognized in the AGN effect.

4.6.1 SN feedback

The first form of feedback considered in our model is the one from SN explosions and high-mass stars outflows, which eject gas and energy into the surrounding Interstellar Medium (ISM). This is supported by several evidences of Supernova driven winds in dwarf galaxies (Martin 1999), which also suggest that the reheating rate is proportional to the SFR.

The parametrization of the SN feedback is based on simple energy arguments. The rate of reheating will be proportional to the SFR, to the number of Supernovae per solar mass of stars, given by $\eta_{SN} = 4 \times 10^{-3} M_\odot$ for a Salpeter Initial Mass Function (IMF), to the energy released by each SN, that is about $E_{SN} = 10^{51} ergs$, and to the efficiency

with which each SN energy is released into the ISM, ϵ_{SN}. This last parameter is highly uncertain, and is treated as a free parameter. The rate of reheating will be more efficient for galaxies living in low potential well, and hence low value of the circular velocity of the halo, and so it is assumed to be proportional to V_c^{-2}. This implies that galaxies living in low-mass haloes are affected by SN feedback effects, and their star formation will be self-regulated, while in high-mass haloes this kind of feedback is ineffective. Therefore the rate of reheating is given by:

$$\dot{M}_{heat} = \epsilon \frac{4}{5} \frac{\eta_{SN} E_{SN} \dot{M}_*}{V_c^2} \tag{4.14}$$

(Kauffmann et al. 1993; Somerville & Primack 1999).

We assume an "ejection" model of feedback, that means that the reheated gas is ejected from the halo and is unable to cool until is reincorporated into a more massive halo at a later step of the hierarchy. We found that this model, at variance with the "retention" model, in which the gas can subsequently cool, leads to a better match of the faint-end of the stellar-mass function, that otherwise is too steep compared with the observations.

4.6.2 AGN feedback

There is growing evidence of a tight relationship between galaxy evolution and the growth of supermassive black holes (SMBHs) powering nuclear activity. Supporting evidences come from the tight correlations between the black hole mass and the velocity dispersion of stars in the bulge (Ferrarese & Merritt 2000, Gebhardt et al. 2000) and that between the BH mass and the mass of the bulge (Haring & Rix 2005). The mutual feedback between galaxies and quasars may be the reason for such strong correlations.

We implement the accretion onto black holes in our model following the prescriptions of Croton et al. (2006) and Kauffmann & Haenelt (2000). We allow two different mode of feedbacks, one occurring during the whole life of the galaxy, that is the *radio mode* and a second one, the *quasar mode* triggered only during mergers of galaxies, together with the starburst. A third natural way of growth for SMBH is represented by coalescence of the BHs residing in the center of two merging galaxies. In this case after the merger of the host galaxies the new BH mass is simply the sum of the two progenitors and thus we ignore the existence of binary systems and gravitational wave losses.

We use as a starting point a seed mass for the BH in the galaxies on the bottom of hierarchy, i.e. living in the "leaves" haloes, equal to $1000 M_\odot$. We also checked the consistency of this choice using different mass of the seed, but we noticed that results do not depend on this choice, at least for small values of the seed. These seeds are believed to form at extremely high redshift from the direct collapse of pre-galactic gas discs.

As in Kauffmann & Haenelt (2000) we assume that during a major merger of

galaxy a certain fraction of cold gas is accreted on to the center of the black hole:

$$\Delta M_{BH}^{QSO} = \frac{f_{BH} M_{cold}}{1 + (280/V_c)^2} \tag{4.15}$$

where f_{BH} is an efficiency to be chosen in order to match the relation between black hole mass and velocity dispersion of the bulge. In this way QSO accretion of BHs is closely linked to the starburst activity of the galaxy, which is triggered during galaxy mergers as well as BH accretion, naturally producing BH masses which increase with the mass of the spheroidal component that is formed only during the starburst.

The second way of accretion is in a continuous and quiescent mode during the whole life of the galaxy, during which the black hole accretes gas directly from the hot halo. The accretion rate is described by:

$$\dot{M}_{BH}^{RADIO} = k_{AGN} \frac{M_{BH}}{10^8 M_\odot} \frac{f_{hot}}{0.1} \Big(\frac{V_c}{200 km/s} \Big)^3 \tag{4.16}$$

Croton et al. discuss two physical models which can justify the accretion of hot gas on to the black hole. The first is the one they call “cold cloud” accretion and it is due to the flow of cold clouds which during their infalling can reach the region of influence of the black hole and become available for fuelling. In order to have fuelling we require that $r_B H > 10^{-4} r_{sonic}$ and this translates in a condition on the mass of the black hole and consequently on the accretion rate onto it.

The second model assumes that the dominant source of accretion is the hot gas which fills the space between these clouds, while the clouds are assumed to be lost to the star-forming disk. The rate at which the hot gas is accretes on to the black hole is given by the Bondi-Hoyle formula (Bondi, 1952):

$$\dot{M}_{BH} = 2.5 \pi G^2 \frac{m_{BH}^2 \rho_0}{c_s^2} \tag{4.17}$$

In both cases, the accretion rate derived is in perfect agreement with the phenomenological one given by equation 4.16.

The most important channel to build up the mass of the black hole is the quasar mode, in which the accretion rate can be much greater than the Eddington luminosity. The second way of accretion, the radio mode, is almost negligible for the formation of present-day black holes, being several order of magnitude below the Eddington rate. Nevertheless it is a fundamental source of feedback in high mass haloes because it suppresses cooling flow as well as the quasar mode mechanism, and it occurs for whole life of the galaxy, while the quasar mode acts only in a very short period of the galaxy life. For these reasons the feedback efficiencies of such processes are set by trying to match different observables. The efficiency of the quasar mode accretion is set requiring the model to match the $M_{BH} - M_{bulge}$ relation, while the radio mode accretion efficiency is set to reproduce the shape of the stellar mass function, and in particular the knee at characteristic stellar masses.

The injection of energy in the ISM due to the presence of AGN occurs in the following way. The mechanical heating generated by the the black hole accretion is given by

$$L_{BH} = \eta \dot{M}_{BH} c^2 \tag{4.18}$$

where η is an efficiency and it is set to 0.1, which is the standard efficiency with which mass is assumed to produce energy near the event horizon and c is the speed of light. Now, the gas cooling rate is corrected by this injection of energy:

$$\dot{M}_{cool}^{new} = \dot{M}_{cool}^{old} - \frac{L_{BH}}{V_{vir}^2/2} \tag{4.19}$$

In order to avoid the unphysical result of a cold gas mass which falls below zero, we enforce mass conservation assuming as new cold gas mass the maximum value between zero and $\dot{M}_{cool}^{new}\Delta\tau$, where $\dot{M}_{cool}^{new}$ is given by 4.19. Hence, the cooling rate can not only be reduced, but also stopped in the case of strong BH accretion rate.

4.6.3 Reionization

It is now known that the hydrogen in the intergalactic medium (IGM), that became neutral at $z \sim 1000$, must have been ionized at later epochs, although the redshift at which this reionization occurred is still quite uncertain, ranging from $z = 6$, as imposed by the lack of a Gunn-Peterson trough in quasar spectra at that redshift (Fan et al. 2000), up to $z = 30$, as imposed by the bound on the optical depth to the last scattering surface measured from CMB (Netterfield et al. 2002). If a large population of galaxies and quasars exist at very high redshift, as predicted by galaxy formation models and confirmed up to $z \sim 6$ by observations (Fan et al. 2000), then reionization could have occurred through photoionization, since both young galaxies and quasars emit UV photons, able to ionize the IGM. This photoionizing background may also act to inhibit galaxy formation in two ways. It can heat the IGM to temperatures of the order of $10^4 K$, increasing the thermal pressure of the gas and preventing it to collapse into the dark matter haloes. The second way is through a reduction of the cooling rate of the gas inside haloes, mainly reducing neutral atoms which can be collisionally excited. This results in a strong suppression of galaxy formation in haloes with $T \sim 10^4 K$, that is in galaxies belonging to the faint-end part of the stellar mass function.

Only a few studies faced the problem of including a self-consistent treatment of the photoionization in a galaxy formation model. An example is the model of Benson et al. (2002), which consider a semi-analytical model (Cole et al. 2000 model) modified to include the photoionization feedback effect, in terms of reducing the cooling rate and heating the IGM. They found that bright galaxies (brighter that L_*) are mostly unaffected by this form of feedback, but it reduces the abundance of galaxies at faint luminosities.

In our model, instead of including a photoionization model, we mimic its effects suppressing gas cooling in haloes with $V_c < 50 kms^{-1}$. As demonstrated by Benson

et al. (2003), this has similar effects to the more complete treatment of Benson et al. (2002).

4.7 Dynamical Friction

Dynamical friction plays a crucial role in the formation and evolution of galaxies. During the merger of two dark matter halos, the baryonic cores they contain, being more compact and less subject to tidal effects, may avoid merging with each other, and end up orbiting within the new combined halo, so that an halo formed by many mergers may contain many distinct galaxies, with the galaxy in the most massive halo becoming the central galaxy and all the others becoming the satellites. These satellite galaxies gradually loose their energy and angular momentum under the action of dynamical friction until they sink to the center of the halo and merge with the central galaxy.

Dynamical friction operates through the gravitational interaction of galaxies with background dark matter particles which slow down their orbital velocities. The case of a rigid object moving in a sea of collisionless particles was originally calculated by Chandrasekhar (1943) for star clusters and can be applied to the case of a satellite galaxy moving in a dark matter halo. The orbit of dark matter particles are deflected by the galaxy and this produces an enhancement of dark matter density behind it. The satellite therefore feels a stronger gravitational pull from the region of the halo that it has just passed through compared with the region that it still has to enter. As a result the orbital energy of the galaxy decays and it spirals in towards the center, eventually merging with the central galaxy if the dynamical friction timescale is shorter than the lifetime of the halo.

The merger timescale, that is the time elapsing between entering the virial radius of the dark matter halo and the final coalescence of the satellite with the central galaxy, can be derived using Chandrasekhar's approach. As demonstrated by Binney and Tremaine (1987) we can consider the frictional force on an object of mass m moving at speed V_c at radius r given by:

$$F = -0.428 \ln \Lambda \frac{Gm^2}{r^2} \tag{4.20}$$

where $\ln \Lambda$ is the Coulomb logarithm, which can be approximate with $\ln \Lambda = \ln(m/M)$ where M is the mass of the halo.

The force is tangential and thus causes the galaxy to loose angular momentum:

$$\frac{dL}{dt} = \frac{Fr}{m} \tag{4.21}$$

where $L = rV_c$ is the angular momentum per unit mass. This leads to the differential equation for the distance of the satellite from the center of the halo as a function of time:

$$r\frac{dr}{dt} = -0.428 \frac{Gm}{r} \ln \Lambda \tag{4.22}$$

that can be integrated from $r = 0$ to $r = r_{ci}$ giving the timescale of dynamical friction:

$$t_{df} = 1.17 \frac{r_{ci}^2 V_c}{GM \ln \Lambda} \tag{4.23}$$

Taking into account the dependence on the orbital circularity, Lacey & Cole (1993) found:

$$t_{df} = 1.17 f(\epsilon) \frac{r_{ci}^2 V_c}{GM \ln \Lambda} \tag{4.24}$$

where ϵ is the circularity parameter of the satellite's orbit, given by $\epsilon = J/J_c$, with J the angular momentum of the actual orbit and J_c the one of the circular orbit with the same energy. A good approximation for the factor $f(\epsilon)$ given by LC93 is $f(\epsilon) = \epsilon^{0.78}$ for $\epsilon > 0.01$. Equation 4.24 can be rewritten as in Cole et al. (2000):

$$t_{df} = 1.17 \Theta \frac{\tau_d}{\ln \Lambda} \left(\frac{m}{M} \right) \tag{4.25}$$

where $\Theta = f(\epsilon)(r_{ci}/R_v)^2$ includes the dependencies on the orbital parameters and we take an average value as found by Tormen (1997): $< \log_{10} \Theta >= -0.14$. We notice the dependence of the dynamical friction timescale on the ratio between the mass of the satellite and the one of the halo the galaxy is moving in. Note that the timescale increases as the halo mass increases, so that at high redshift, when the halos are less massive we find an high rate of merging, whereas it decreases at low redshift and we have an accumulation of subhalos inside the parent halo.

An important consideration concerns the mass m used to compute the dynamical friction timescale. As it is shown by Navarro et al. (1995) using the dark matter mass of the satellite leads to a good match between dynamical friction timescale and merging timescale found in numerical simulation, whereas using only the baryonic mass of the satellite results in too big timescales. Nevertheless also tidal stripping may have effect on the satellite mass. Initially most of the mass of a satellite comes from its dark matter, but as it plunges into the center a large fraction of the dark halo is stripped away, while the mass of the gaseous core is too dense to be stripped. Thus the effective mass of the satellite decreases with time and the dynamical friction timescale should increase. In this work we did not take into account this effect, but since we realized that the timescales for merging were too small, leading to an overmerging, mainly at low redshift, we tried to mimic the effect of tidal stripping assuming that each satellite retains its dark halo only for the first lifetime of their host halo and loose it at the next timestep. Different authors include the effect of tidal stripping in SAM models (Benson et al. 2002, Menci et al. 2002) and we plan to model this effect in a more realistic way in a future work.

Recent estimates of the dynamical friction timescale from numerical simulations leads to expressions slightly different from the one described above and commonly used in SAM. Jiang et al. (2008) and Boylan-Kolchin et al. (2007) compared their derived timescales with the LC93 expression and found that, in contrast to Navarro et al. (1995), the theoretical merger timescales are not in agreement with the simulated

values. They conclude that LC93 timescale is underestimated for minor mergers and overestimate for major mergers. Since major mergers are one of the major driven of the galaxy assembly, it should be interesting to compare results even with this improved timescales.

4.8 Satellite Collisions

In addition to the mergers due to dynamical friction which involve only the central galaxy and one of the satellites, we include collisions between satellites.

In order to compute the cross section of this process we assume, as a first approximation, that the overall structure of the galaxies is not changed during a collision. Consider a galaxy of mass m_1 moving in the potential of a galaxy m_2 with initial velocity v_1 and impact parameter P. The final velocity will be v_1' and the radius of minimum approach is r_{min}. We make use of the conservation of energy and angular momentum:

$$\frac{1}{2}m_1 v_1'^2 = \frac{1}{2}m_1 v_1^2 - \frac{G m_1 m_2}{r_{min}} \tag{4.26}$$

$$P v_1' = r_{min} v_1 \tag{4.27}$$

Given that the cross section of the process is $\Sigma = \pi P^2$ and applying the condition for having a merger, we obtain (see Cavaliere et al. 1992):

$$\Sigma = \pi (r_1 + r_2)^2 \Big(1 + \frac{2G(m_1 + m_2)}{(r_1 + r_2)V_{rel}^2}\Big)\Big(\frac{v_{gal}}{V_{rel}}\Big)^{2/3} \tag{4.28}$$

where v_{gal} is the internal dispersion of the galaxy. The term $\frac{2G(m_1+m_2)}{(r_1+r_2)}$ is proportional to the internal dispersion of the galaxy, and V_{rel} is proportional to the circular velocity V_c of the halo hosting the galaxies, so that the cross section strongly increases with the decrease of the relative velocity of the two galaxies. For example in cluster of galaxies $V_{rel} \sim 1000$ km/s, while the internal velocity dispersions of the galaxies are $\sim 100 - 300$ km/s, and collisions are very unlikely.

Instead of this approximate cross-section we use the one of Mamon (1992), which is a simplified version of the cross-section derived from N-body simulation of Roos & Norman (1979):

$$\Sigma = \pi P^2 \tag{4.29}$$

with

$$P = \left\{ \begin{array}{ll} \alpha_p r_{gal}\Big(1 - \frac{v}{\alpha_v v_{gal}}\Big) & v < \alpha_v v_{gal} \\ 0 & v \geq \alpha_v v_{gal} \end{array} \right\} \tag{4.30}$$

where r_{gal} and v_{gal} are the radius and internal velocity dispersion of the two colliding galaxies, respectively, while $\alpha_p = 4$ and $\alpha_v = 5.4$ are dimensionless number.

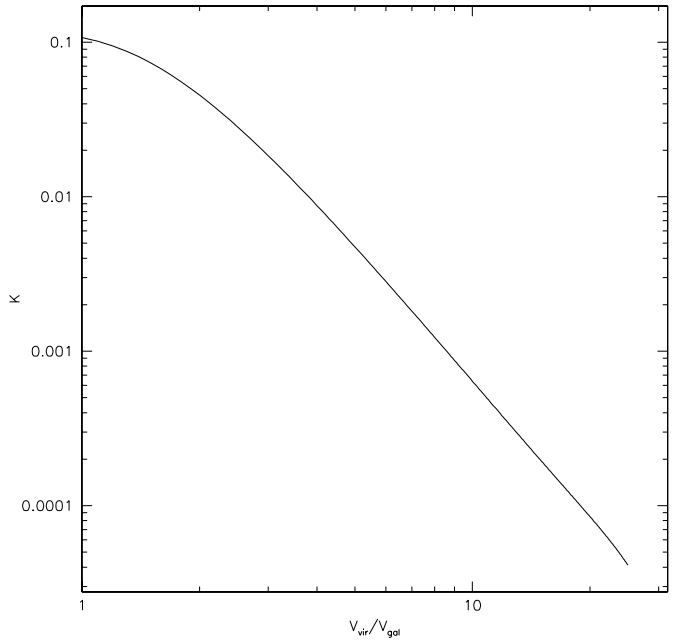

FIGURE 4.3— Dimensionless merger rate K as a function of the ratio of cluster to galaxy velocity dispersion (eq. 4.33).

The merger rate is obtained integrating the binary cross-section over the distribution of the relative velocities $f(v)$, which is assumed to be a Maxwellian with dispersion $\sqrt{2}V_c$

$$k = \int_0^\infty \Sigma(v) f(v) v dv \tag{4.31}$$

$$= 2\sqrt{\pi}\alpha_p^2 \alpha_v R_h^2 v_{gal} K(V_c/v_{gal}) \tag{4.32}$$

where K is a dimensionless merger rate given by:

$$K = \left[\frac{1}{x} + \frac{2}{x^3} - \frac{2\exp(-x^2)}{x^3} - \frac{3\sqrt{\pi}}{2}\frac{erf(x)}{x^2}\right] \tag{4.33}$$

$$x = \frac{\alpha_v v_{gal}}{2V_c} \tag{4.34}$$

As illustrated in figure 4.8, for realistic values of the ratio V_c/v_{gal} the merger rate decreases with this ratio and becomes very low for galaxy clusters.

Given the merger rate we can compute the collision time as:

$$t_{coll} = \frac{1}{kn} \tag{4.35}$$

where n is the number densities of galaxies in the halo. We obtain shorter merger timescale at high redshift, when the number density of galaxies is higher. The probability for having a merger for a satellite with another one, randomly chosen, will be $P = \Delta t/t_{coll}$, where Δt is the lifetime of the halo. We consider only binary merger, and we assume that such event occurs when $P > 1$.

After the merger, the total mass of the remnant (dark matter and baryons) is the sum of the two merging satellites, while the new radius and circular velocities are computed from applying the conservation of energy and the virial theorem. According to the virial theorem, the total internal energy is given by $E_{int} = -T$. By applying conservation of energy:

$$T_{new} = T_1 + T_2 - E_{orb} \tag{4.36}$$

where T denotes the kinetic energy and E_{orb} is the mutual orbital energy:

$$E_{orb} = -f_{orb}\frac{Gm_1m_2}{r_1 + r_2} \tag{4.37}$$

(r_1 and r_2 are the radius of the two progenitors and f_{orb} is a parameter which weakly depends on the density profile, we assume $f_{orb} = 0.5$). These considerations yield to:

$$R_{new} = \frac{(m_1 + m_2)^2}{m_1^2/r_1 + m_2^2/r_2 - f_{orb}m_1m_2/(r_1 + r_2)} \tag{4.38}$$

During a collision between two satellites we allow a burst of star formation in the same way of the one occurring during a merger between a satellite and the central galaxy.

The effect of including such process in addition to the mergers involving the central galaxy due to dynamical friction, is to decrease the fraction of low-mass galaxies in favor of intermediate-high mass objects, and to slightly modify the shape of the mass function.

4.9 Morphology

In our model the morphology of the galaxy is determined by the relative importance of the bulge component over the disk component. The only way of formation of disks is through the quiescent mode of star formation, while bulges can grow in two ways: through star formation occurring in a starburst event, hence triggered by any event of merger, and through the disruption of disks following a major merger. We define a merger to be major when the ratio between the stellar mass of the smallest and of the biggest galaxy are greater then $1/3$. In this case all the stars belonging to the disks undergoing merger are added to the bulge of the remnant galaxy. Such galaxy may eventually form a new disk if some fraction of cold gas is still present.

As a proxy for the morphologies of the simulated galaxies we use the ratio between the bulge mass and the total stellar mass: $r = M_{bulge}/M_*$ Using the prescription of Bertone et al. (2005), we classify as ellipticals galaxies with more than 70% of their stars in bulge, as Spirals galaxies having $0 < r \leq 0.7$, and as Irregulars galaxies without any bulge.

4.10 Differential equations

Summarizing the procedure described in the previous sections, we have to solve differential equations over time for the three components involved: hot gas mass M_{hot}, cold gas mass M_{cool}, and stellar mass M_*. As time-step of integration we choose a small time interval $\Delta\tau$ given by 1/100 of the life-time of the halo where we are computing the baryons evolution. This turns out to be of the order of some *Myrs*.

We start from the "leaves" haloes, i.e. haloes without progenitors, assigning them as initial values:

$$M^0_{hot} = f_{bar} M_{DM} \tag{4.39}$$

$$M^0_{cool} = 0 \tag{4.40}$$

$$M^0_* = 0 \tag{4.41}$$

$$M^0_{BH} = 1000 M_\odot \tag{4.42}$$

We compute the values at the end of time-step in the following way:

$$M_{cool} = M^0_{cool} + \dot{M}_{cool}\Delta\tau - \dot{M}_*\Delta\tau - \dot{M}_{SN}\Delta\tau - \dot{M}_{AGN}\Delta\tau \tag{4.43}$$

$$M_* = M^0_* + \dot{M}_*\Delta\tau \tag{4.44}$$

$$M_{hot} = M^0_{hot} - \dot{M}_{cool}\Delta\tau + \dot{M}_{SN}\Delta\tau + \dot{M}_{AGN}\Delta\tau + f_{bar}\dot{M}_{acc}\Delta\tau \tag{4.45}$$

$$M_{BH} = M^0_{BH} + \dot{M}_{BHradio}\Delta\tau + \dot{M}_{BHqso}\Delta\tau \tag{4.46}$$

where $\dot{M}_{cool}$ is given by equation 4.6 in the case of cold mode ($r_{cool} > R_{vir}$) and by equation 4.7 in the opposite regime ($r_{cool} < R_{vir}$); $\dot{M}_*$ is given by 4.11 for the quiescent mode and by 4.12 for the starburst mode of star formation; $\dot{M}_{SN}$ is the reheating from SN expressed in equation 4.14 and $\dot{M}_{AGN}$ is the reheating due to the AGN feedback, from 4.19;$\dot{M}_{BHradio}$ and $\dot{M}_{BHqso}$ are, respectively the accretion rate onto black-hole in the radio mode (eq. 4.16) and in the QSO mode (eq. 4.15). $f_{bar}\dot{M}_{acc}$ is the rate of accretion of hot gas from outside the halo and $\dot{M}_{acc}$ is simply given by the Dark Matter mass which is not resolved in a halo but is accreted onto the main progenitor halo. In fact, when we build the merger tree we keep track of the amount of diffuse dark matter mass accreted by the halo at every step, M_{acc}. This is simply the difference between the parent halo mass and the sum of all its progenitors. We assume here, that the mass of hot gas accreted over the entire timestep between two level of the hierarchy is $f_{bar}M_{acc}$ and that the mass accretion rate is constant over the timestep.

5

GECO's first Results: fitting the zero-redshift data and predicting the high-redshift evolution

In this Chapter we present the results derived with our semi-analytic model of Galaxy formation. We first compare our results for the local universe with observations in order to set the free parameters. After that we compare our predictions for the distant universe, mainly focusing on the star formation and mass assembly of galaxies.

5.1 Setting the free parameters

In the previous Chapter we have introduced several free parameters in the analytical prescriptions which model galaxy formation. Now we summarize them:

- α: efficiency of star formation in quiescent mode
- f_b: efficiency of star formation in starburst
- ϵ: efficiency of SN feedback
- f_{BH}: efficiency of AGN feedback in the QSO mode
- k_{AGN}: efficiency of AGN feedback in the radio mode

We derive them by comparing results from the model, obtained for different sets of parameters, with observations of the local universe. In particular we want to focus on the build-up of stellar mass, and we require our model to fit the local stellar mass function, as well as the relationship between the black-hole mass and the bulge mass. The stellar mass function is influenced by all the parameters: the star formation efficiency in the quiescent mode α affects the overall shape and normalization of the function, ϵ affects

TABLE 5.1— Free parameters

Parameter	Meaning	Best-fit value	Range
α	star formation	0.01	0.01-0.1
f_b	burst efficiency	0.75	0.5-1
ϵ_{SN}	SN feedback efficiency	0.5	0.01-1
f_{BH}	AGN feedback efficiency in QSO mode	0.005	0.001-0.1
k_{AGN}	AGN feedback efficiency in radio mode	1×10^{-6}	$10^{-7} - 10^{-6}$

the faint-end (or low-mass end), f_b determines the contribution of the bulge on the total stellar content, and we require that at the bright-end bulges dominate over disks, and the AGN efficiencies, f_{BH} and k_{AGN} shape the bright-end of the mass function. Moreover, the AGN efficiency in the quasar mode, i.e. the one triggered by the starburst episode, determines the relationship between the mass of the black-hole and the bulge mass, affecting mainly the normalization of the relation, while the slope turns out to be very close to the one observed almost independently on the value of this efficiency. In table 5.1 we report the value of these parameters in our best-fit model and the range allowed. Unless otherwise stated, in the following we always will refer to this best-fit model.

5.2 The Local Stellar Mass Function

A key prediction of any model of galaxy formation is the number density of galaxies as a function of their stellar mass in the nearby universe. Indeed, the most important constraint for setting the free parameters in the model is to reproduce the observed stellar mass function (SMF) in the local universe. We refer to two measurements of the local SMF. The first is that observed by Cole et al. (2001), hereafter C01, produced combining data from the Two Micron All Sky Survey (2MASS) and the 2dF Galaxy Redshift Survey. The second estimate, is taken from Bell at al. (2003). They use a large sample from the Two Micron All Sky Survey (2MASS) and the Sloan Digital Sky Survey (SDSS). We choose to show their *g*-selected sample (taken from their table 5). Both estimates use near-infrared data to compute stellar masses and hence are highly reliable. In fact, they are the best suited to the determination of this quantity, because infrared light is dominated by old stellar populations and it reflects the integrated star formation history of a galaxy. Moreover, correction for dust extinction and k-correction are much smaller in the near-IR than in the optical bands. As shown in figure 1.2 the C01 mass function lies very close to other determinations, except for a possible underestimation of the number densities at very low masses ($\lesssim 10^9 M_\odot$). Note that here both mass functions have been converted to Salpeter IMF. As shown in figure 1.2 the C01 and B03 mass functions lie very close to other determinations, except for a possible underestimation of the number densities at very low masses ($\lesssim 10^9 M_\odot$) in

the case of C01.

In Figure 5.1 we show the stellar mass function at $z = 0$, resulting from the model and compared with the C01 and B03 observations. The model is able to reproduce with good accuracy the shape and normalization of the SMF, especially in the bright-end ($log(M) > 10.5$). Compared to the C01 mass function, the model shows an excess of galaxies at the faint-end. However, the B03 estimate presents a steeper faint-end, resulting closer to our prediction. A slight excess of intermediate masses ($log(M) \sim 10$) with respect to both data is still present.

The contribution to the total stellar content from disks and bulges is also shown, with blue short-dashed and red long-dashed lines, respectively. As expected, the bright-end is dominated by bulges, meaning that objects with very high-mass ($log(M) > 11$) do not essentially contain any disks, that have been presumably destroyed during a major merger. On the contrary, disks overcome the number densities of bulges at low masses, and start to be dominant in the mass range $log(M) = 10 - 10.5$. Note that this value is close to the transition mass, equal to $3 \times 10^{10} M_{\odot}$ at z=0, observed by Baldry et al. (2004), defined as the mass at which early-type galaxies start to outnumber late-type ones (see section 1.2.1).

So far we have considered only the contribution the the total stellar mass density from the disk and bulge components. In figure 5.2 we show the mass function of early-type and late-type galaxies. As defined in the previous Chapter early-type galaxies are defined as galaxies whose bulge forms at least the 70% of the total stellar mass. We include in the definition of late-type systems both spiral galaxies and irregulars. We compare in figure 5.2 the resulting mass function with the results of B03. With this definition of morphologies the agreement with data is quite good, and in particular we reproduce exactly the transition mass at which the number density of ellipticals equals the one of late-type galaxies.

It is worth to make a consideration about the different shape of the halo mass function and the luminous (or stellar) mass function, here presented. The generic shape of the dark matter halo mass function, as predicted by any theoretical model, is in the form of a pure power-law with a steep faint-end and no knee at the bright-end. A turn-off mass do exist, but it occurs at much higher masses than the characteristic stellar mass observed in the stellar mass function (see figure 3.9). In order to obtain a Schechter function for the luminous mass function two effects contribute. On the faint-end side, the feedback from SN and from photoionization suppresses star formation in small haloes, hence reducing the faint-end slope. On the bright-end, the difference between the exponential cut-off observed in the stellar mass function and the power-law shape of the halo mass function is explained with the dependence of the gas cooling from the halo mass. Indeed, the cooling time decreases with the halo mass. Moreover, in section 4.3, we have discussed that two mode of cooling exist. In the cold mode regime gas accretes towards the center in a timescale given by the free-fall time, while in the opposite regime, the hot mode, the accretion rate is governed by the cooling time, and is much less efficient than in the former case. Since in high-mass haloes the accretion occurs through this last mechanism, this may explain why in this haloes, gas

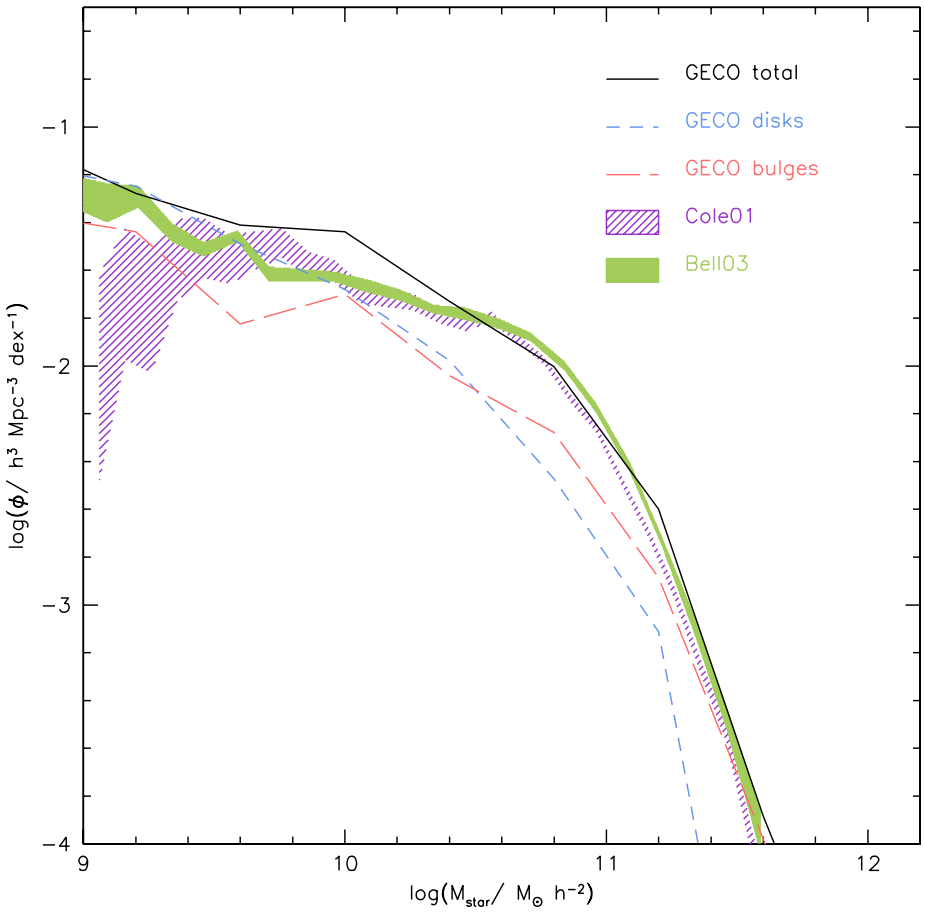

FIGURE 5.1— Stellar mass function at z=0. Black solid line and circles represent the SMF resulting from GECO, red line and squares stay for the C01 observed mass function. Also shown is the contribution to the total stellar mass content from bulges (red long dashed line) and disks (blue short dashed line).

is not able to cool efficiently, hence justifying the lack of galaxies more massive than $10^{12} M_{\odot}$.

5.3 BH-Bulge Relation

In order to set the efficiency of black-hole growth we require our model to match the relation between the black-hole mass and the mass of the stellar bulge in the local universe. We compare our model results with observations by Haring & Rix (2004), derived for a sample of 30 nearby galaxies.

Since the major channel for the growth of black-hole is given by the accretion during the quasar mode, that is triggered during a starbust event, in which all the stars

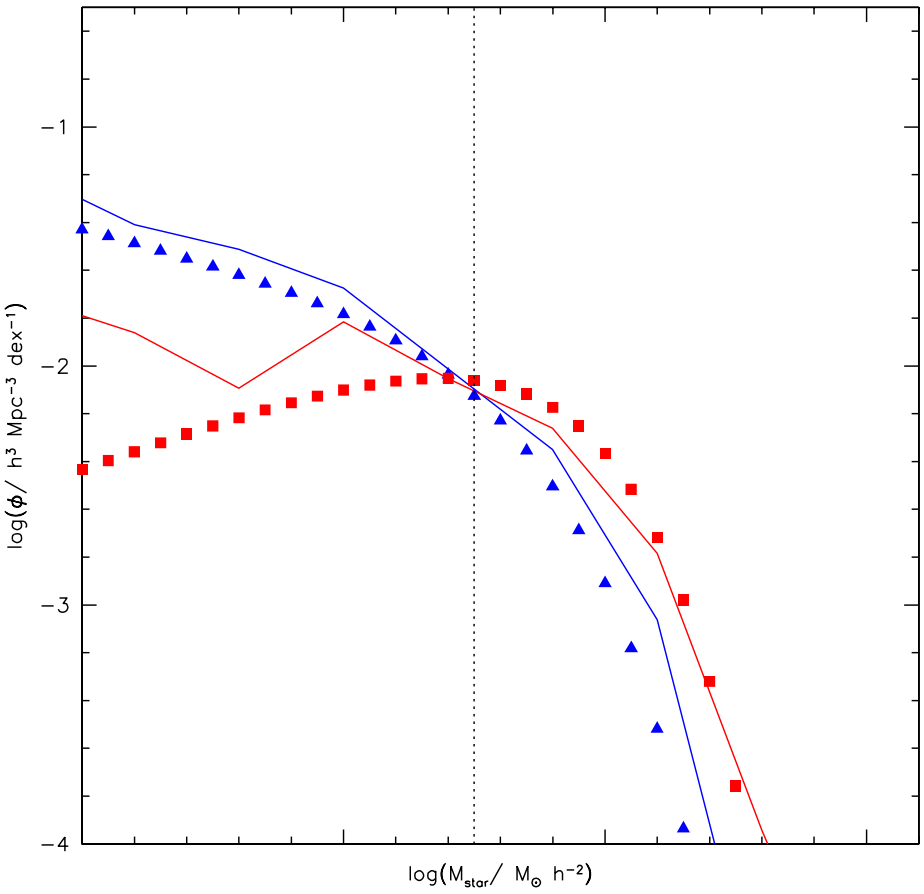

FIGURE 5.2— Stellar mass function at z=0 of early type (red solid line) and late-type galaxies (blue solid line) compared with the observed one by Bell et al. 2003: dashed red line for early-type and dashed blue line for late-type.

formed are added to the bulge component, it is not surprising that black-hole and bulge are closely linked. In any case, in order to obtain an acceptable model, where both the slope and the normalization of the relation are well reproduced, some optimizations were required. In Figure 5.3 we show the comparison between our derived relation (points: red for central galaxies and black for satellites) with the best-fit of Haring & Rix (2004), represented by the magenta line. The observed relation is well reproduced by our model over a large range of masses. Note that the Haring & Rix (2004) fit is derived only for bulge masses $M_b > 10^{10} M_\odot$.

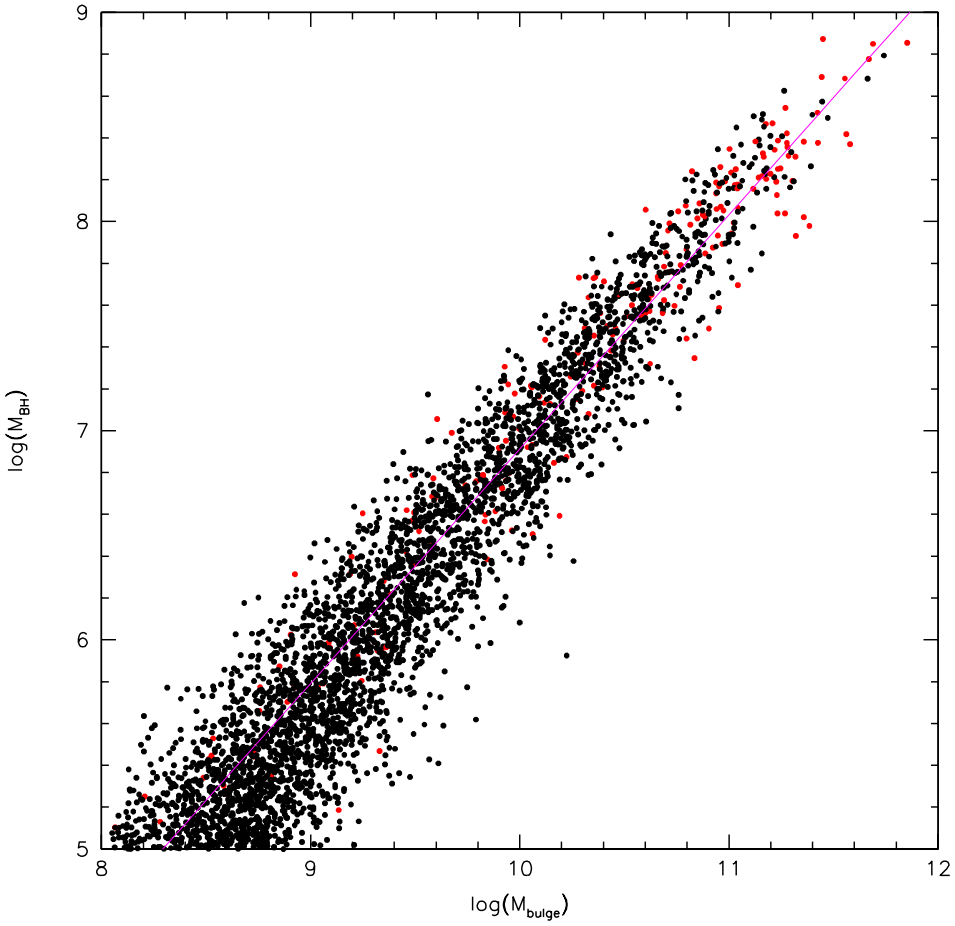

FIGURE 5.3— Black-hole versus bulge mass relation at z=0. Black points represent data for satellite galaxies, while red points are for central galaxies. The magenta solid line is the best fit relation derived in the local universe by Haring & Rix (2004).

5.4 Evolution of the Stellar Mass Function

Since we have set the model in order to match the global properties of the local universe, we can now attempt a first comparison of the model predictions for the distant universe without any further adjustment to the parameters. In this section we proceed to test the resulting mass function up to $z \sim 3.5$.

In figure 5.4 we show the comparison of the GECO's stellar mass functions for different redshifts, from $z \sim 3.5$ to the present time. Two behaviours can be noted. A steady increase of the characteristic stellar mass with cosmic time, by a factor of $\lesssim 2$ from $z \sim 1$ to $z = 0$ and by at least an order of magnitude from $z \sim 3.5$ to the present, and a a substantial evolution of the number density of massive objects ($log(M) \gtrsim 11$)

from $z \gtrsim 3$ to $z = 0$, while no evolution of the faint end is observed.

A first comparison of the GECO's mass functions with that observed is shown in figure 5.5 for intermediate redshifts, up to $z \sim 1$. Here we compare our model mass functions with results from Franceschini et al. (2006), hereafter FR06, who derived stellar mass functions from the analysis of multi-wavelenght data, from optical to the near-IR, in the GOODS-S field. Thanks to the use of near-IR Spitzer bands (up to $8\mu m$) and to an high spectroscopic coverage, stellar mass and redshift estimates are high reliable. Moreover their results are compatible with Fontana et al. (2004) and Bundy et al. (2005) findings. While observations indicate very low evolution of the number densities progressing from the lowest to the highest redshift, in the model prediction a significant amount of stellar mass in high-mass objects is assembled at relatively low redshift, ($z \gtrsim 0.5$). A deeper comparison with a larger set of observational data is shown in figure 5.6, up to $z \sim 3.5$. In addition to the FR06 mass function for the first redshift bins, the results from Fontana et al. (2006), hereafter F06, Drory et al. (2005) (D05), and Berta et al. (2007), (B07), are indicated. Note that the FR06 mass function in the first redshift bin is computed for the redshift interval $0.1 < z < 0.55$, so the mean redshift is lower than $z = 0.5$, for which the GECO predictions and the other observed mass functions are computed. Hence, an overprediction with respect to the other estimates is expected. Error bars in F06 and D05 take into account not only Poisson statistics, but also errors on redshift measurements and stellar mass, therefore they result larger compared with the FR06 ones. Considering the spread between different estimates of the mass function, the number density of massive galaxies in our model is roughly consistent with the observed values, although with a tendency to underpredict the data, especially at high redshift. In the highest redshift bin considered ($z \sim 3.5$) the bright-end is marginally consistent with that of F06, but much lower with respect to D05. Note that in the highest redshift bin, D05 finds more massive galaxies compared to F06. This is likely due to the lack of Spitzer observations in the D05 sample, which leads to an overestimation of stellar masses at $z > 3$ (see F06), hence their determination must be considered less reliable than the F06 one. Concerning the faint end of the mass function, the model overpredicts the number of low-mass objects at any redshift. While in the data there is a significant evolution in the number density of low mass galaxies, in the model their number keeps modest up to high redshift.

5.5 Stellar mass density

In order to have a global picture of the galaxy assembly through cosmic time, here we compute the integrated comoving stellar mass density, namely the integral of the mass function over all masses as a function of redshift. In figure 5.7 we compare our estimate (black line) with the results of F06 (blue shaded region) and of D05 (magenta shaded region). The observed value at $z = 0$ is taken from Cole et al. (2001). Note that in order to integrate the mass function down to $M = 10^8 M_\odot$, F06 extrapolate their Schechter fit, since data are not complete down this mass limit.

The model stellar mass density is clearly overpredicted at all redshifts, since, as

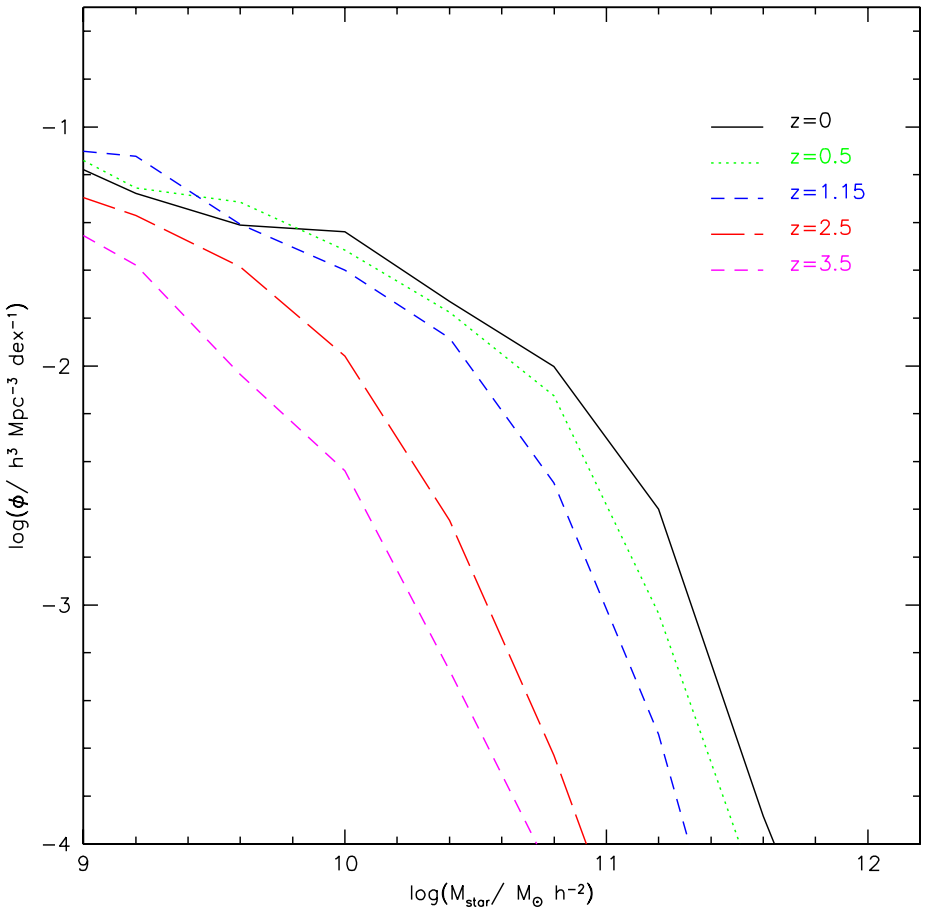

FIGURE 5.4— Stellar mass function predicted by the model at different redshifts: from $z = 0$ up to $z = 3.5$ from top to bottom.

noted in the previous section, it produces an excess of low-mass galaxies compared with data. Anyway, the evolutionary trend depicted by the model agrees with that observed, where the mass assembly proceeds at fast rate at high redshift and then slows down at recent epochs. Given the fact that the faint-end is already in place at high redshift, the assembly in the model occurs earlier than in observations.

In figure 5.8 we concentrate on the bright-end of the mass function, therefore we compute the integral using only galaxies with masses $M > 10^{11} M_{\odot}$, comparing our computation with that of F06 and B07 (red square), who derived this quantity in the same range of mass. In this case, the evolution of the massive tail of the mass function is in nice agreement with data, at least for low and intermediate redshift, up to $z \lesssim 1$. Note that at $z \sim 0.5$ our predicted stellar mass density appears higher than that

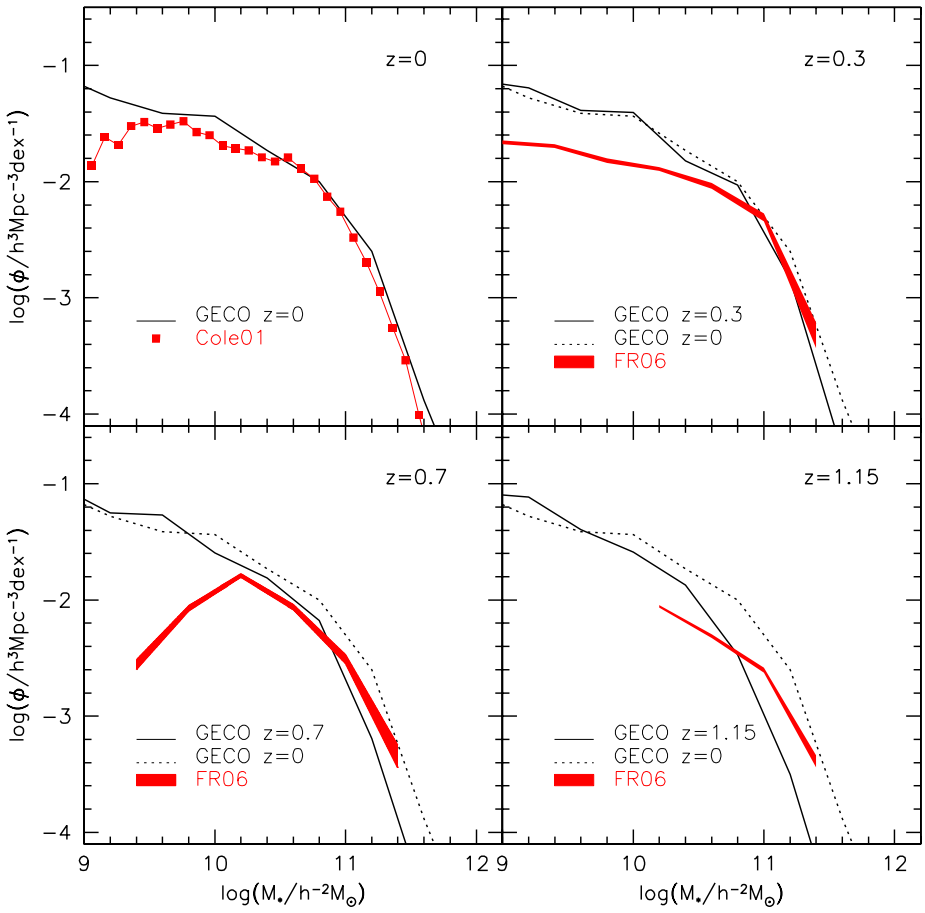

FIGURE 5.5— Comparison between GECO's mass functions at different redshifts with observations of C01 in the first panel and with F06 observations in the other panels. Red squares and solid lines represent the observed mass functions in each case, while black circles and solid line are the model predictions. The MF at z=0 are reported as black dotted line in all the panels for reference.

observed, but at this redshift the F06 data suffer of undersampling of massive galaxies, because of the small size of the volume covered.

At high redshift, the mass assembly has proceeded at a slower rate, and the corresponding stellar mass density is underpredicted, although at $z \sim 2$ it is marginally consistent with the B07 estimate. The fast assembly of high-mass galaxies can be noted even in the evolution of the mass function in figure 5.4, where the major amount of evolution occurs between z *sim*3.5 and $z \sim 1.15$.

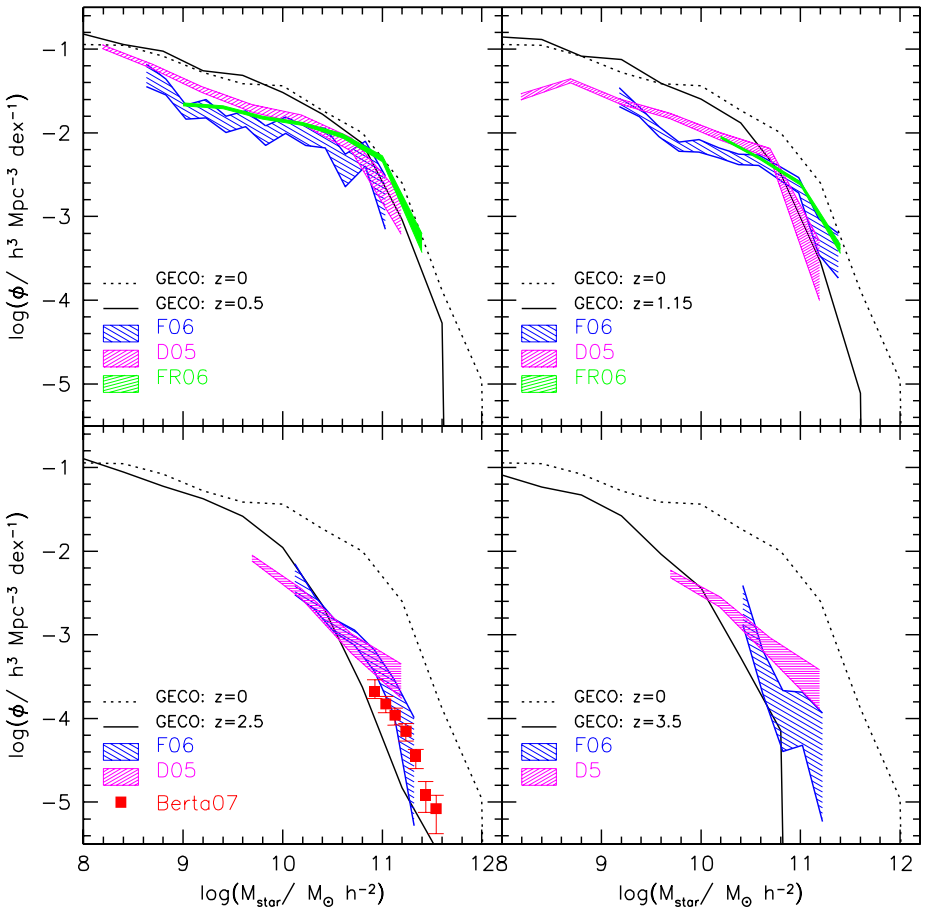

FIGURE 5.6— Comparison between GECO's mass functions at higher redshift, up to $z \sim 3.5$. The green shaded region indicates the mass function of Franceschini et al. (2006), the blue one is that of Fontana et al. (2006), while with the magenta region we show the Drory et al. (2005) estimate. Red squares at $z \sim 2$ show the results from Berta et al. (2007). GECO predictions are represented with a solid black line. The dotted line in all the panels is the GECO mass function at $z = 0$, reported as reference.

5.6 Star Formation Histories

In order to get a deeper look into the the build-up of the stellar mass of our modelled galaxies, we investigate their detailed star formation history (SFH), that is the star formation rate as a function of cosmic time.

In figure 5.9, we show as an example, the SFHs for 4 different realizations of the central galaxy of a halo with mass $5\times10^{12}\,M_{\odot}$, i.e. very similar to the Milky-Way halo. We derive SFH *a posteriori* for each galaxy present at $z = 0$, deriving its baryonic tree and summing up all the stars formed in its progenitors. We represent the star formation

occurring in the quiescent mode with a blue shaded histogram and with the red one we show the star formation during the starburst phase. The black envelope is the sum of both contributions. In each panel the halo mass and the stellar mass are indicated, together with the parameter r, that is the ratio between the bulge and the total stellar mass. It is expressed in red for Elliptical galaxies and in blue for Spirals and Irregulars, which form the late-type population. In the case of a Milky-Way like halo the majority of central galaxies are Spirals ($\sim 60\%$). SFHs are computed over 52 timesteps, that is our pre-defined grid of timesteps used for the merger tree.

We end-up with an heterogeneous mix of galaxies. In some cases the star formation history is quite smooth (see panel *d*), with a steep rise of SFR at early time followed by a smooth decrease. At early-times starbursts are very frequent, even in galaxies that at the present time have a late-type morphology. In some cases, more than one peak of quiescent star formation are present (see panel *a* and *b*), indicating that star formation has occurred in different progenitors of the final galaxy. In other cases, the starburst can occur at recent times ($z \lesssim 0.5$ in panel *c*) and is more efficient in consuming all the gas, therefore subsequently the galaxy evolves passively until $z = 0$.

In order to give an indication of the age of a galaxy we define its formation redshift as the redshift when the galaxy has formed half of its present-day stellar mass. We indicate it in figure 5.9 as a vertical dashed line. Galaxies with a smooth, quiescent star formation tend to form their stars later, while galaxies that have undergone a more bursty star formation tend to have higher formation redshifts.

In figure 5.10 we show the SFH of the central galaxy of haloes with different mass, averaged over 10 realizations of the same parent halo tree. Halo masses range from $\sim 10^{12} M_{\odot}$ up to $2{\times}10^{14} M_{\odot}$. Passing from low-mass to high-mass haloes, the starbursts become the dominant mechanism of star formation. The increasing importance of the starburst mode, together with the AGN feedback connected to it, which prevents gas to cool and inhibit further star formation, lead to a low rate of star formation at late times, and hence to higher formation redshift for galaxies living in high-mass haloes.

Since high-mass galaxies live in high-mass haloes this result indicates that stars in massive galaxies are on average older than in their less massive counterparts. Nevertheless even in massive galaxies a tail of star formation at low redshift still occurs.

This behaviour of our SFHs turns out to be in nice agreement with the '*downsizing* nature of galaxy evolution. The naive expectation in hierarchical models of galaxy formation is that, since massive haloes are assembled later than their low-mass counterpart, the most massive galaxies, hosted in the largest haloes, should assemble their stellar content at the same time. Actually, this is not the case. Indeed, '*downsizing* is an intrinsic feature of semi-analytical models. The present-day massive galaxies were formed through the assembly of a number of smaller progenitors, that at high redshift, collapsed from the highest density peak of the primordial density field. According to this scenario, also called biased galaxy formation picture (Dekel & Silk, 1986), bright and massive systems started to form stars early. This can be easily understood even within the merger tree formalism. Progenitors of high-mass haloes fall below the resolution mass imposed to the merger tree after several timesteps, so the leaves of the tree

are found at high redshift. On the contrary, smaller systems, closer to the resolution mass, employ only a few timesteps to reach the minimum mass. Since baryons are put into haloes starting from the leaves, in high mass haloes star formation takes place at early times. Moreover, at high redshift both mechanisms of star formation were more effective. Thanks to the more efficient cooling of the gas the quiescent mode of star formation occurs at enhanced rate. Moreover, the frequency of mergers at these times is high, allowing an efficient conversion of gas in stars through the mechanism of starburst.

5.7 Cosmic Star Formation Rate Density

The evolution of the comoving star formation rate density out to $z = 6$ is shown in figure 5.11. The model prediction is shown by the black histogram and is compared with data from the compilation of Hopkins (2004), for UV, optical and radio tracers, and from Rodighiero et al. (2008) for the IR tracers. Different colors encode different tracers for the SFR: blue for star formation derived from the UV continuum, green for optical tracers (O II, Hα and Hβ), red from SFR derived from the IR luminosity and magenta for data using radio tracers. The model provides a good fit to the data over most of the redshift range. At low redshift ($z \lesssim 1$) there is an indication that our model produces too stars. It is marginally consistent with UV determinations, but it is higher with respect to the recent determination of Rodighiero et al. (2008) using the Spitzer 24μm luminosity function. At very high redshift ($z \gtrsim 4$), the comparison may indicate that the star formation rate at early time is a bit low in the model. However, at this redshifts data are highly uncertain and must be taken with caution. The high level of star formation rate at high redshift found in the model was already mentioned in the previous section. On one side, the quiescent mode of star formation is highly effective, due to the high cooling efficiency in denser environment. Indeed, the peak in the quiescent mode of star formation (blue shaded histograms in figure 5.10) is always at $z \sim 2$. On the other side, at high redshift the star formation mainly occurs in starbursts, triggered by the high rate of mergers, which strenght the SFR at early cosmic times. The exhaustion of cold gas available explains the sharp decline at low redshift.

In figure 5.12 the contribution to the total star formation rate density (black histogram) is splitted according to the mass of the host halo: the dashed red histogram shows the contribution from galaxies living in high-mass haloes ($M > 3 \times 10^{12} M_{\odot}$), while the green dashed histogram shows the one from galaxies living in less massive haloes. The time dependence of the star formation rate in the two cases is similar: a slow increase at high redshift, with a strong decline at low redshift. Nevertheless the peak of star formation activity in the high-mass haloes is shifted at higher redshift: $z \sim 2 - 4$ compared with $z = 1 - 3$ in less massive haloes.

We confirm the results found in the previous Section: galaxies residing in high-mass haloes form their stars at early epochs, and then their star formation rapidly slow-down, while galaxies in less massive system form stars at an enhanced rate even

at recent times ($z \lesssim 1$).

5.8 Star Formation and Mass Assembly

Although in the previous Section we show that massive systems form their stars at earlier times then less massive objects, the time of mass assembly may be very different from the formation time, if stars are formed at high redshift in a number of distinct progenitors that assemble at recent times. In figure 5.13-5.15 we compare the star formation history with the "assembly history" for single realizations of different parent haloes. In the upper panel we show the SFH with the same notations of figures 5.9-5.10, while in the bottom panels we show the mass assembled in the main progenitor at each timestep. Red histograms indicate the amount of stars added to the bulge in a given timestep, while blue histograms show the stars added to the disk. Although in a few cases the assembly is very similar to the star formation, indicating that star formation took place mainly in the main progenitor, in general the two paths are very different. Usually the assembly of bulges, due to mergers, is related to starbursts, although in some cases, mainly when the merger occurs at low redshift, the mass assembly is not associated to any event of star formation (see figure 5.15*b*). This means that gas is already consumed, and a great part of the final mass is assembled into the main progenitor in a *dry merger* (see figure 5.14*b*).

This leads to very different formation times for the process of star formation and mass build-up. We define the redshift of assembly as the redshift when half of the final stellar mass is assembled in one single objects and we show it in the figures. By definition the assembly redshift is always less than the formation redshift, they equal each other when all the stars are formed in the main progenitor (see figure 5.13*a*).

In figure 5.16 we show the mean formation redshift (upper panel) and assembly redshift (lower panel) for central galaxies as a function of the halo mass. The mean formation redshift shows a clear trend with halo mass: galaxies living in high-mass haloes (that are the most massive galaxies) have higher formation redshift compared with galaxies in smaller haloes. At variance with the formation redshift, the assembly redshift shows a lower dependence on the halo mass, even though galaxies in high-mass haloes on average have higher assembly redshift but with a high scatter. Nevertheless, formation redshifts in high-mass haloes are always much greater than the corresponding assembly redshift: for $M_h > 10^{14} M_\odot$ (where we find galaxies with $M_* > 10^{11} geco_s fhav M_\odot$) the mean formation redshift is $z_{form} \sim 2-3$, while half of the present-day stellar mass is assembled at redshift $z_{ass} \sim 1$. We argue that this late assembly of stellar mass, mainly due to dry mergers occurring at low redshift, is the major reason of the evolution in the bright-end of the mass function between $z = 1$ and $z = 0$.

5.9 Summary

In this Chapter we have presented the results of our new semi-analytic model GECO. After the calibration of the model over observations in the local universe, such as the

local stellar mass function, the black-hole bulge mass relation and the relative contribution of bulges and disks to the total stellar mass content, we have discussed the predictions of the model for the high-redshift universe. We found a good agreement with the cosmic star formation history of the universe over a wide range of redshift. At the earliest cosmic times ($z \gtrsim 4$) the model seems to form less stars compared with the observations, but uncertainties in the data are very large to get conclusions. Analysing the detailed star formation history galaxy by galaxy, we found that on average galaxies living in high-mass haloes form their stars earlier than systems in the low-mass counterpart. Hence our results show that a *downsizing* scenario for the galaxy formation is a natural outcome of hierarchical models of galaxy formation.

Comparing the star formation history galaxy by galaxy with their assembly history, we found that the two processes follow rather different timescales, and the assembly redshift can be much lower than the formation redshift, because of the occurrence of late dry mergers in high-mass systems. This late assembly may explain the trend found in the mass function, where we predict an amount of evolution for the bright-end higher than the observed one. Therefore although the *downsizing* in star formation is qualitatively reproduced in our model, the *downsizing* in mass assembly still remains an open question.

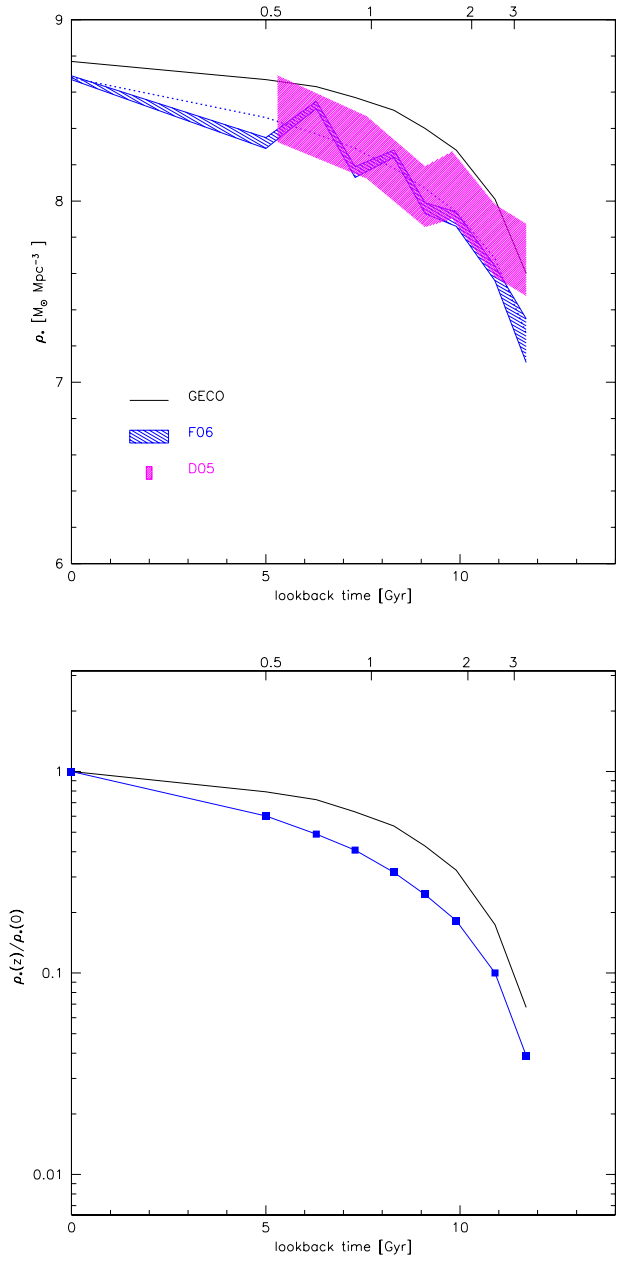

FIGURE 5.7— *Upper panel*: total stellar mass density as a function of cosmic time. The GECO's prediction is derived from the integration of the mass functions of figures 5.5 - 5.6 and is shown by the black line. Blue shaded region represents the data with error bars from F06, while the blue dashed line is the integration of their data of the Schechter fit. Magenta shaded region shows the stellar mass density of D05. *Lower panel*: stellar mass density normalized to the value in the local universe. The model (black line) is normalized by the value of the integral at z=0, while the F06 density (blue line) is divided by the integral of the Cole et al. (2001) mass function.

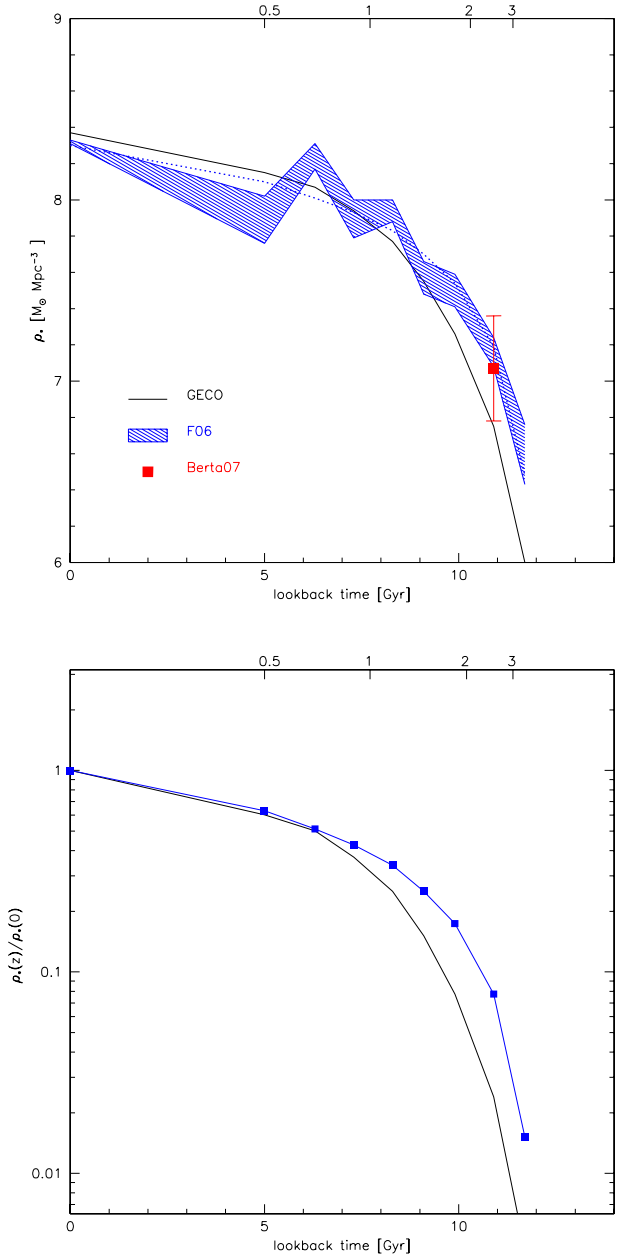

FIGURE 5.8— Stellar mass density computed for massive galaxies: $M > 10^{11} M_\odot$. Black line refers to the model, while blue shaded region and dashed line show the F06 data as in figure 5.7. The red square at $z \sim 2$ is the estimate of Berta et al. (2007).

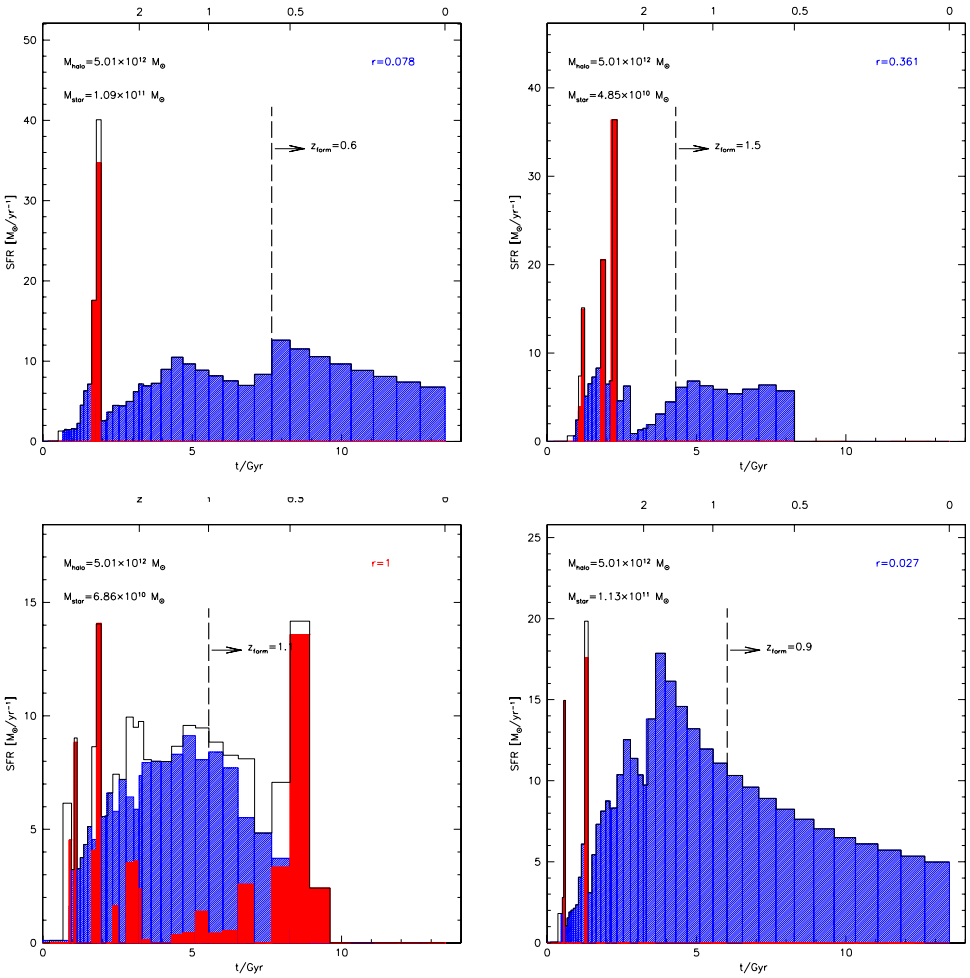

FIGURE 5.9— SFHs for different realizations of the central galaxy of a Milky-Way like halo, having mass equal to $5 \times 10^{12} M_{\odot}$. Blue shaded histograms show the star formation occurring in quiescent mode, the red ones represent the bursty mode, while the black envelope is the total SFR. The vertical dashed line indicates the formation redshift of the galaxy.

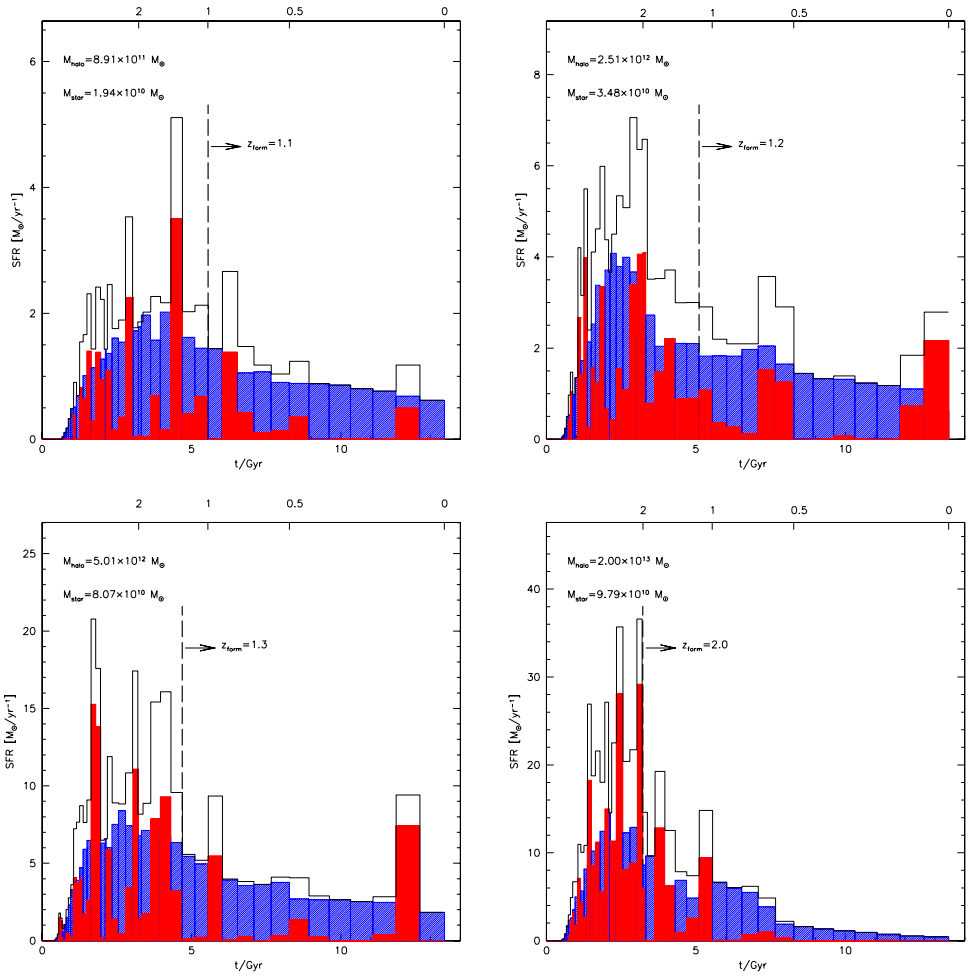

FIGURE 5.10— SFHs for different halo masses averaged over 10 realizations.

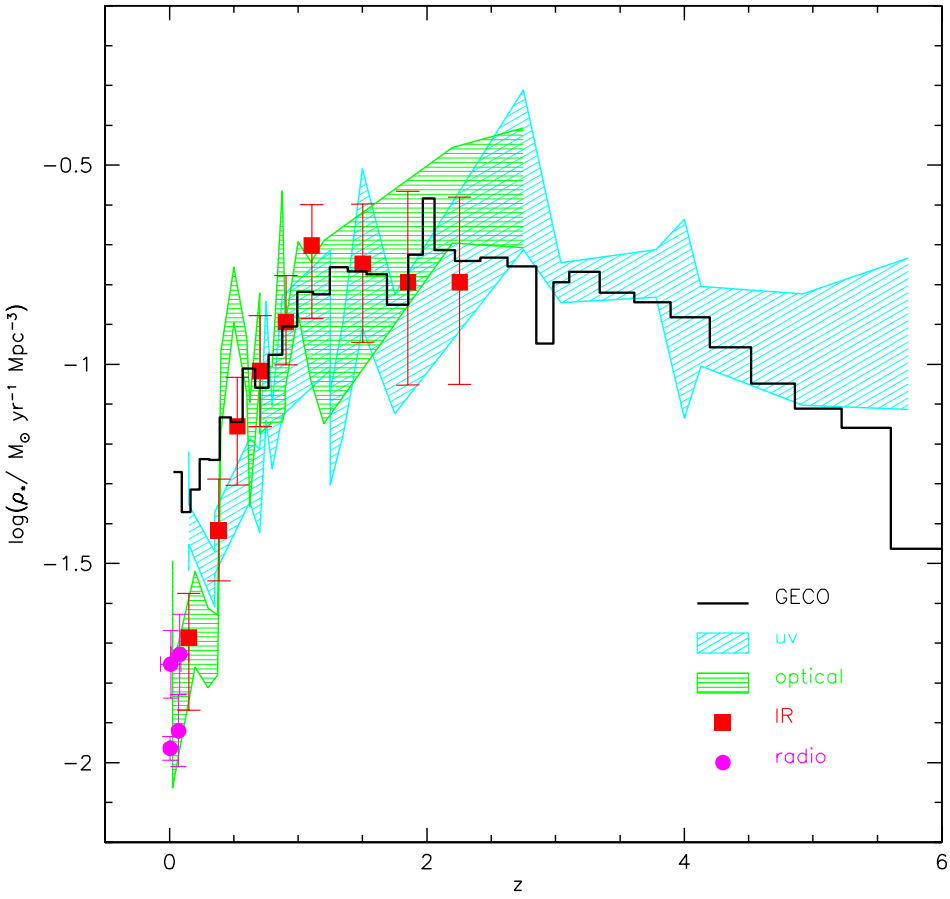

FIGURE 5.11— SFR density as a function of redshift (Madau plot). Solid black line shows the GECO predictions. The shaded area and coloured points are the SFR obtained from observations at different wavelenghts. The cyan shaded region shows the SFR derived from UV tracers, green region means that observations are in the optical, red squares in the infrared and magenta in the radio.

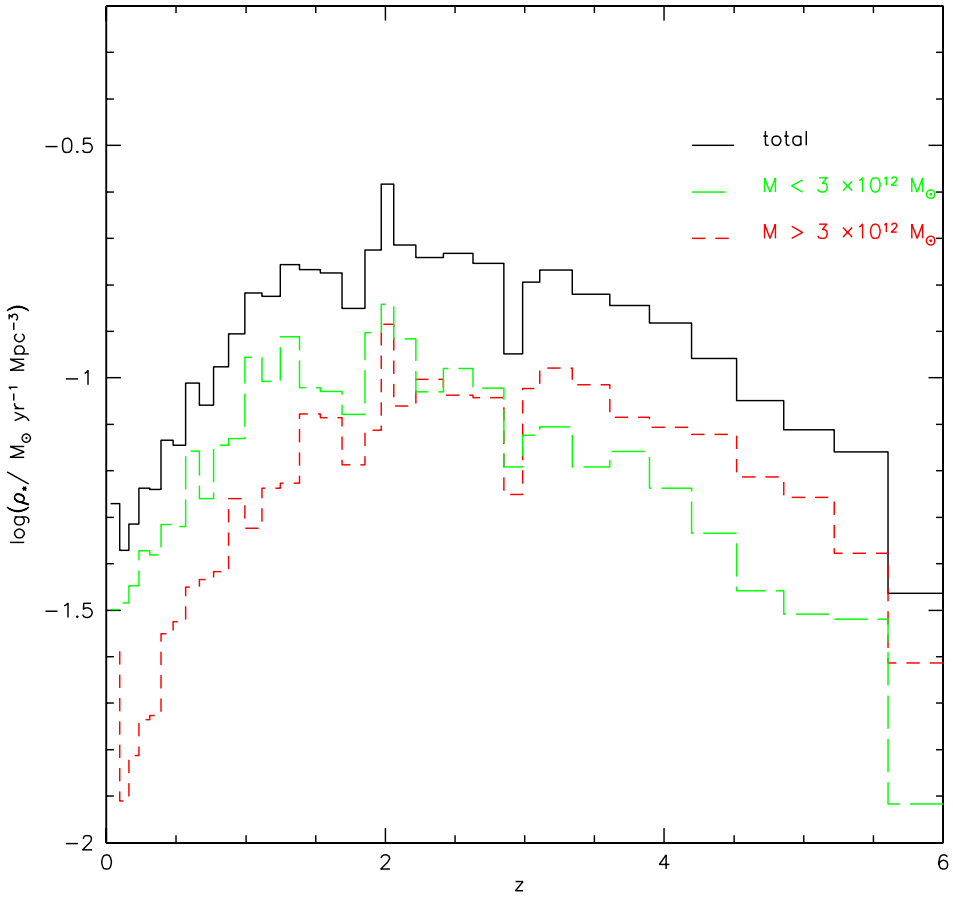

FIGURE 5.12— SFR density as a function of redshift (Madau plot). Solid black line shows the total SFR density, red short dashed shows the contribution from galaxies living in high-mass haloes ($M_h > 3\times10^{12}M_\odot$), while the green short-dashed curve represents the contribution from galaxies in less massive haloes ($M_h < 3\times10^{12}M_\odot$)

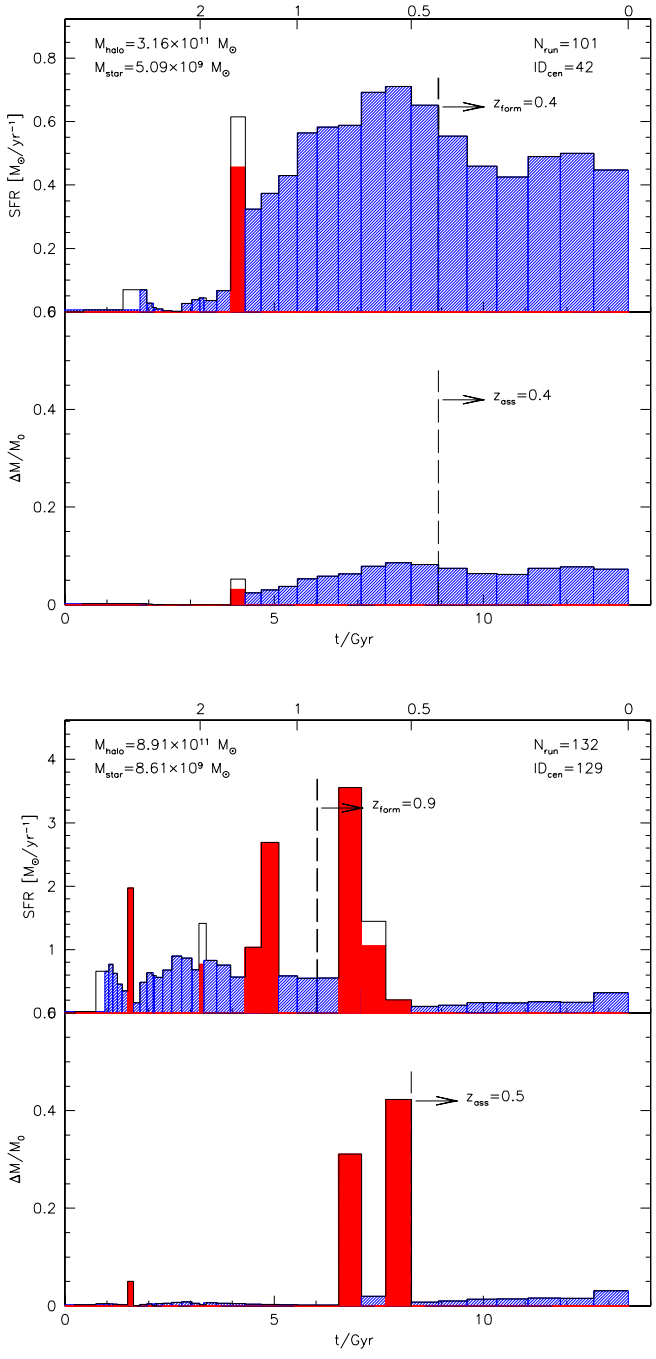

FIGURE 5.13— Comparison between star formation (upper panels) and mass assembly (lower panels) for different model galaxies, living in different haloes. In the star formation rate panel red and blue histograms represent, respectively, bursty and quiescent SF, while in the assembly panels red and blue stay for the mass assembly of bulges and disks respectively .

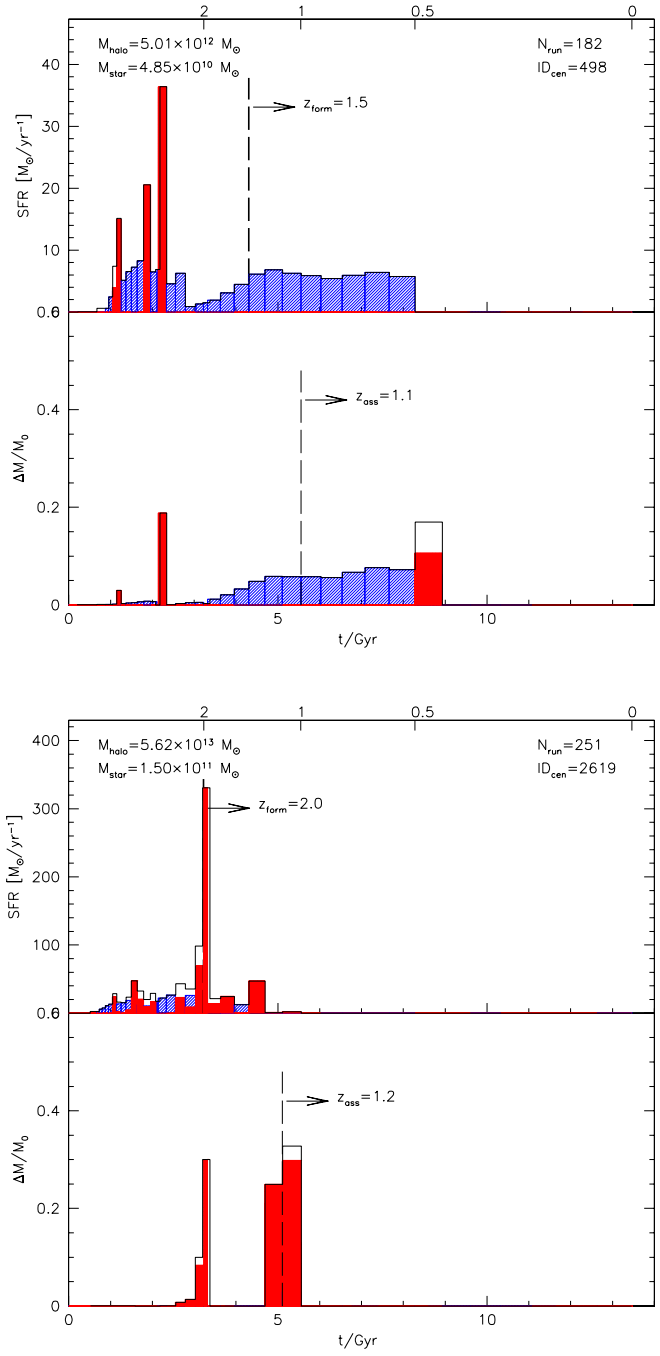

FIGURE 5.14— The same as figure 5.13 but for different halo masses.

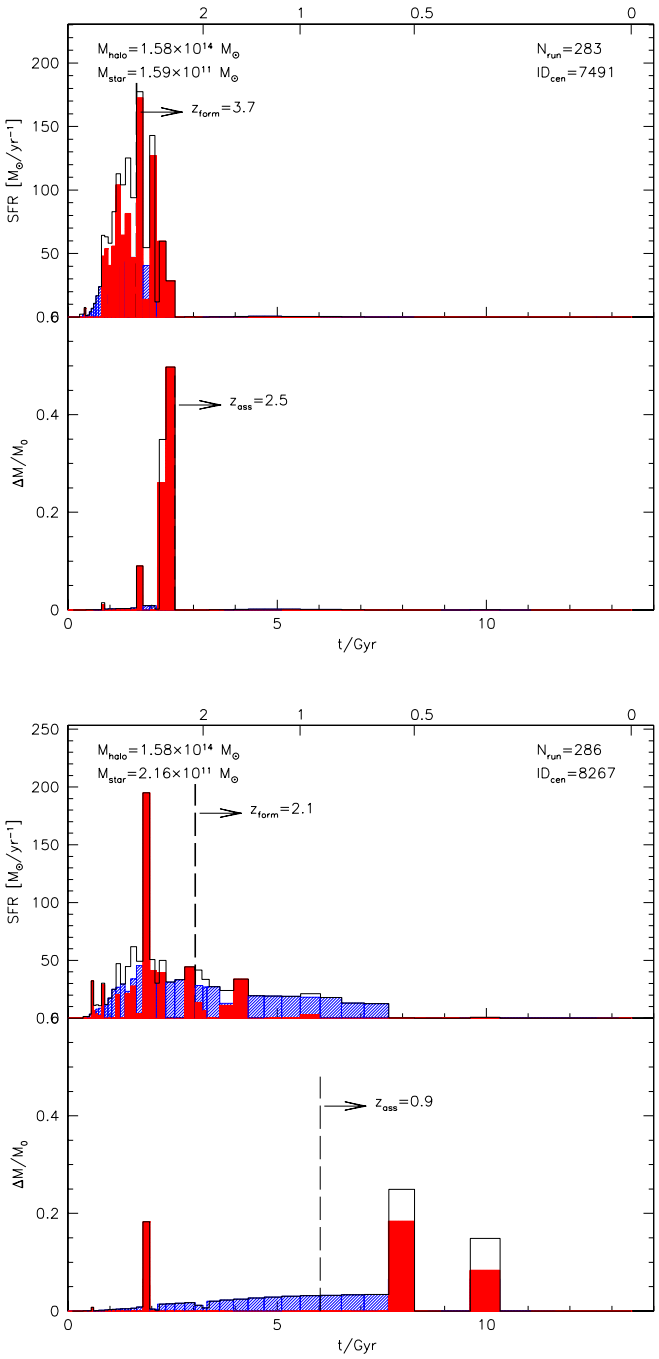

FIGURE 5.15— The same as figure 5.13 but for different halo masses.

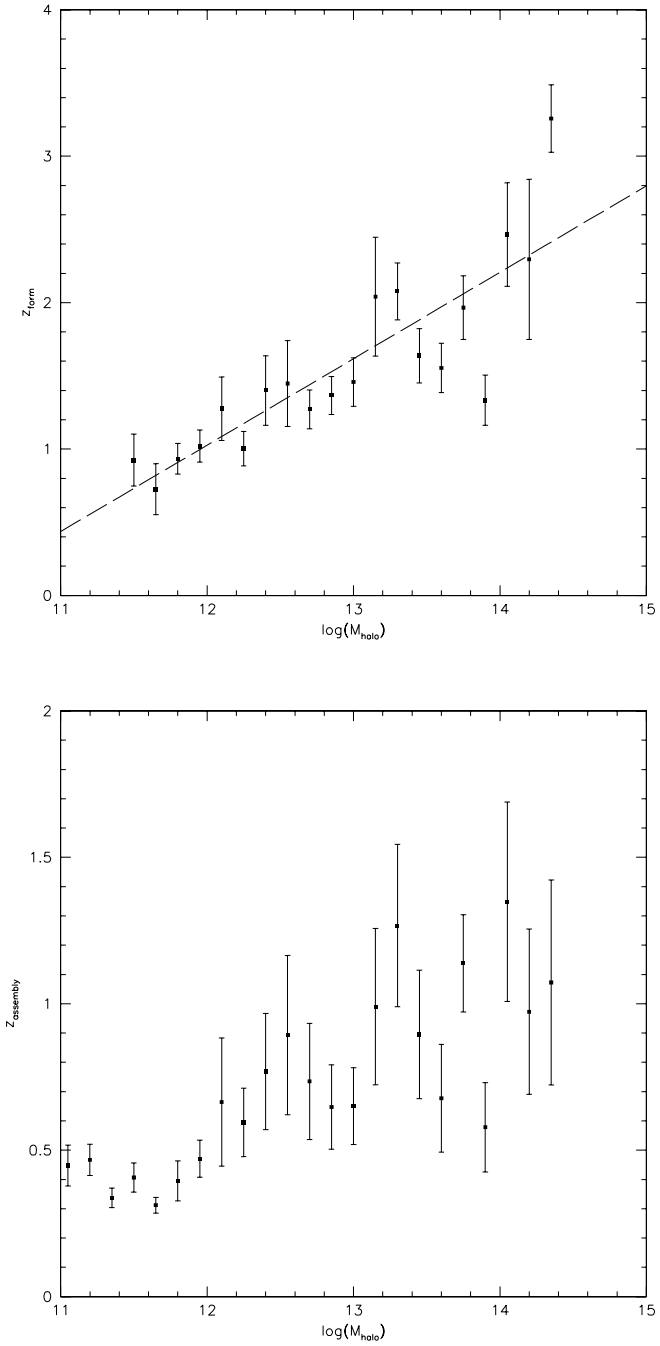

FIGURE 5.16— Mean formation redshift (upper panel) and assembly redshift (lower panel) of central galaxies as a function of their host halo mass. In the upper panel dashed line show the least square fit to the points.

6

Exploration of physical parameters of GECO

In this Chapter we study the effects of varying the different free parameters introduced in GECO. From slightly modified versions of the fiducial model, we investigate how the star formation efficiency in the quiescent and bursty mode, and the inclusion of SN and AGN feedback influence the shape of the local stellar mass function and the timescales of star formation and mass assembly.

6.1 Variations of the fiducial model

One of the major advantages of a semi-analytic model of galaxy formation is its flexibility, namely the fact that models with different recipes and different values of free parameters can be easily tested, simply switching on and off different physical ingredients. This allows to test the relative importance of a given parameter among others, and to understand the physical reason of the results obtained.

In the previous Chapter we set the free parameters by requiring a good match to the local stellar mass function. With this set of parameters we explored the behaviour of the model at high-redshift, finding a good agreement with observations. Analysing the Star Formation History galaxy by galaxy, and integrating it over all the galaxies formed in the model, we found a good match of the cosmic star formation rate density with observations at different wavelenghts over a large range of cosmic times ($z \lesssim 6$), with a peak of the star formation rate at $z \sim 1.5 - 3$ and a rapid decline at lower redshift. The assembly history of galaxies, as recovered by the evolution of the stellar mass function, turned out to be more difficult to reproduce but it resulted in a row agreement with data, when different set of observations were taken into account, although we found a slight shortage of high-mass galaxies at high redshift and an overabundance of low mass objects, which show lower evolution compared with the observed values. Another interesting feature of the model is that it naturally reproduces the apparent *downsizing* nature of galaxy formation, namely the fact that on average high-mass

galaxies formed earlier than low-mass ones.

In this Chapter, we make some changes to our fiducial model previously described, simply modifying the values of the free parameters involved, in order to understand the physical reason of the the results described above, and the relative importance of the various parameters introduced.

Here we present four different variation on the fiducial model and we summarize them in Table 6.1. In the Model 1 we turn off completely the AGN feedback, setting to zero both the radio mode and the QSO mode. In the Model 2, we increase the efficiency of the star formation in the quiescent mode (α), while in Model 3 we switch off the burst mode of star formation. Finally, in Model 4 we test the effect of the SN feedback, lowering the SN efficiency, ϵ_{SN}. In the following we test how these variations on the model affect the stellar mass function in the local universe and at high redshift, an hence the stellar mass density and the Madau plot. We also checked how galaxies living in different haloes contribute to the total star formation rate density, as a test of *downsizing*.

TABLE 6.1— Free parameters for different models.

	α	f_b	ϵ_{SN}	f_{BH}	k_{AGN}
Fiducial Model	0.01	0.75	0.5	0.005	1×10^{-6}
Model 1 (No AGN)	0.01	0.75	0.5	**0**	**0**
Model 2 (High SF)	**0.1**	0.75	0.5	0.005	1×10^{-6}
Model 3 (No burst)	0.01	**0**	0.5	0.005	1×10^{-6}
Model 4 (Low SN)	0.01	0.75	**0.1**	0.005	1×10^{-6}

6.2 Model 1: no AGN

In this model we switch off the feedback from AGN, setting both the efficiencies in the radio and in the QSO mode to zero. We can see the effects of such variation on the local stellar mass function in figure 6.1. In the left panel, the total SMF is presented for the model without AGN feedback (solid green line) and for the fiducial model (black dashed line). From the comparison we can deduce how the presence of the AGN influences only the bright part of the mass function, reducing the presence of high mass objects by ~ 0.2 dex. Nevertheless the amount of the decrease is quite small, given the fact that the values for the efficiencies must lead to a good agreement of the bh-bulge relation and hence can not be set to arbitrary high values. In the other panels of figure 6.1 the mass function of disks (upper panel) and bulges (lower panel) are shown. The AGN feedback mainly affects the bulge mass function, in the bright-end, while the disks mass function is only slightly overproduced in the the absence of AGN feedback with respect to the fiducial model at intermediate masses. Hence, the difference between the total SMF of the fiducial case and that of Model 1, is mainly due the increase of the bulge mass function, confirming that the dominant mechanism

of AGN accretion is through the QSO mode, that is effective only during starbursts and hence affects the bulge masses.

In figure 6.2 we show the evolution of the stellar mass function for intermediate redshifts ($z = 0.3 - 1.15$). In panel *a* the evolution for the mass function of the model without AGN feedback are shown. The mass function evolves in the same way as in the fiducial case (see figure 5.4), with a continuous decrease in the abundance of high-mass objects at increasing redshift and the faint end almost unchanged. In panel *b-c-d* the model mass functions are compared with the fiducial model and with the observation of FR06. Given the overabundance of high-mass galaxies by ~ 0.2 dex observed at all the redshift, the high-mass tail of the mass function at high redshift turns out to be in closer agreement with the FR06 observations with respect to the fiducial model.

In figure 6.3 we compare the stellar mass density (SMD) in the Model 1 and in the fiducial model, integrating over all the galaxies (total stellar mass density, upper panel) and integrating only for galaxies with $M \geq 10^{11} M_{\odot}$, (lower panel). At all cosmic times, the SMD for the model without AGN feedback is greater than the fiducial model, and the difference is higher when only the high-mass end is integrated, since only the bright-end is overpredicted. It is interesting to note that at high redshift ($z \gtrsim 2$), the difference between the two models decreases, meaning that the importance of the AGN feedback in reducing the stellar mass increases as cosmic time increases. This is confirmed even by the cosmic star formation rate density, shown in figure 6.4. Clearly the star formation is higher if no AGN feedback is introduced in the model, and the difference between the model without (solid green line) and with (dashed black line) AGN feedback increases at low redshift. Such dependence of the effect of feedback on redshift can be understood in terms of accretion onto BH (eq. 4.15-4.16). The amount of gas accreted onto the black-hole depends on the circular velocity of the halo hosting the galaxies, that increases as cosmic time increases. In the case of radio mode the dependence on redshift is enforced even by the dependence on the black hole mass. In the lower panel of figure 6.4 the star formation rate density of the Model 1 is splitted in the contribution given by high-mass systems (red long-dashed line) and low-mass ones (light green short-dashed line). As already found in the fiducial model, here we confirm how high-mass galaxies are more active in forming stars at high redshift, while low-mass systems continue to form stars down to later epochs, demonstrating how the *downsizing* phenomenon reproduced in our model is not due to the presence of AGN.

Hence, studying the effect of the presence of AGN feedback in the model we concluded that it has the effect of reducing star formation mainly in high-mass objects and in the starburst mode, affecting mainly the bulge mass function. Nevertheless the amount of reduction in the stellar mass is not extremely high, and perhaps less than previously claimed (Croton et al. 2007; Bower et al. 2006). As deduced from the stellar mass density and from the star formation rate density, the effect of the AGN feedback is higher at low redshift ($z \lesssim 2$), when both the halo potential well hosting the galaxy, and the black-hole mass are higher. Finally we confirm even in this model that galaxies are found to evolve in a *downsizing* way.

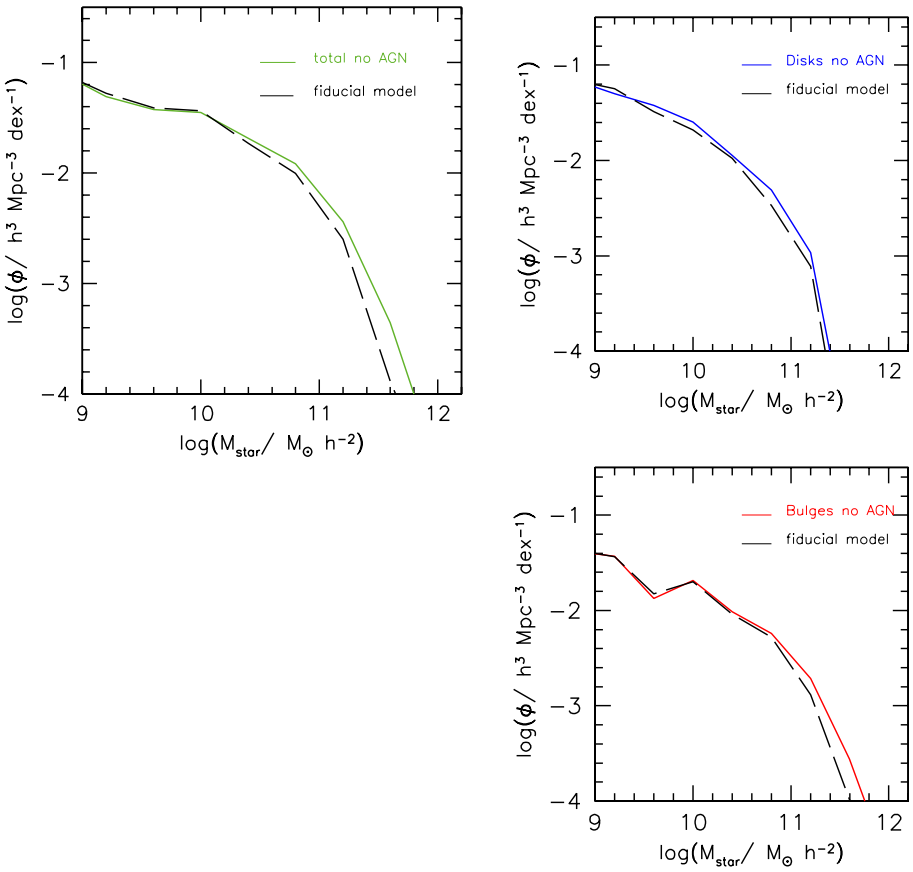

FIGURE 6.1— Comparison between the local stellar mass function for the model without AGN feedback and the fiducial model. In the upper-left panel the total SMF for the model without AGN is shown by the green solid line, while the black dashed line represents the fiducial model. In the right-upper panel and in the right-lower one the mass function of the disk and of the bulge component, respectively, are indicated with the solid (blue and red) lines. The dashed black line is again the prediction of the fiducial model.

6.3 Model 2: High SF

In this section we analyse the importance of the star formation efficiency, α, in the quiescent mode. Since the fiducial value for this parameters is set to lowest possible value, in the Model 2 we test its importance by increasing it of an order of magnitude. The effect on the local stellar mass function seen in figure 6.5 is extremely high: increasing α both the characteristic stellar mass, and the abundance of high mass objects increase. Looking at the disk and bulge mass function separately, we notice that the major effect is in increasing the mass of the disks. This is a direct consequence of the enhanced

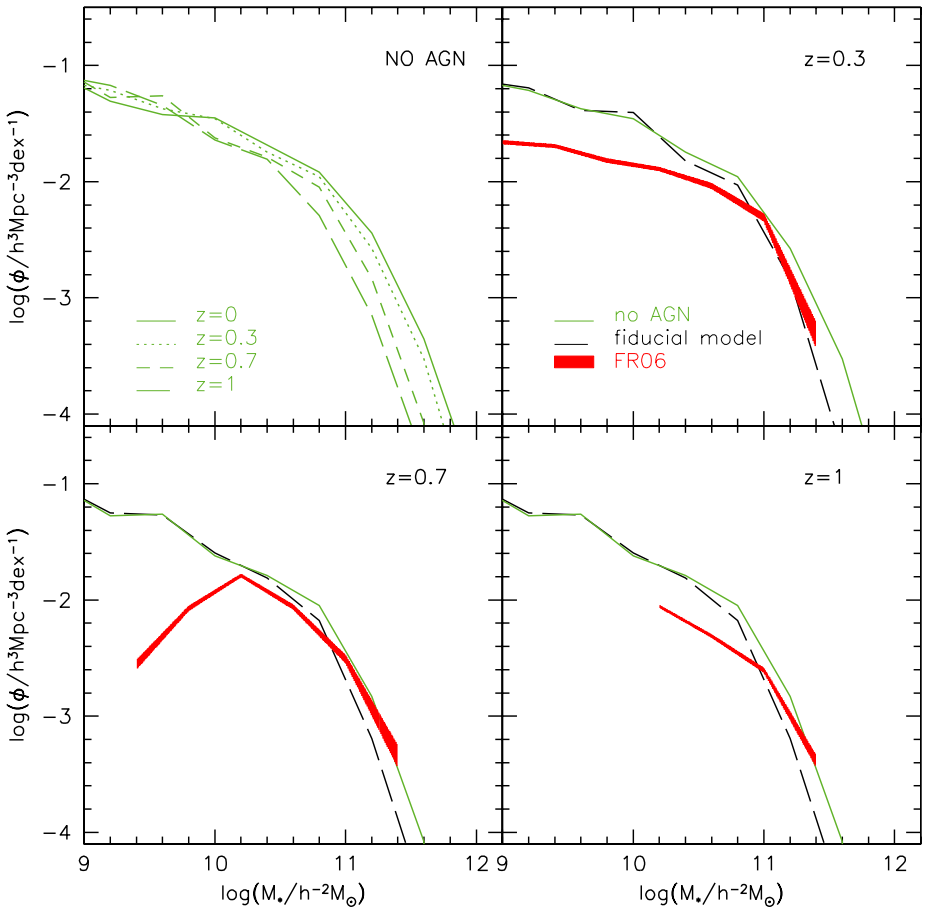

FIGURE 6.2— Evolution of the stellar mass function in the model without AGN feedback. In the first panel the mass function at different redshift for this model are indicated. In the other panels the evolved mass function (green lines) are compared with the observations of Franceschini et al. (2006) (red shaded region) at the corresponding redshift and with the fiducial model (dashed black line).

star formation efficiency, because in the quiescent mode of star formation, stars are added to the disk component. However, even the bulge mass function is influenced, with an increase of high mass bulge and a decrease of low-mass ones. We argue that the increased disk masses lead to mergers between higher mass systems which end up with a massive remnant (that in the case of major mergers are made only by bulge) at the expenses of low-mass systems.

The mass function evolution, shown in figure 6.6, shows the same evolutionary path seen in the fiducial model, but with a slight higher amount of evolution in the high mass end (here ~ 0.4 dex in the bright-end, ~ 0.3 dex in the fiducial model). The

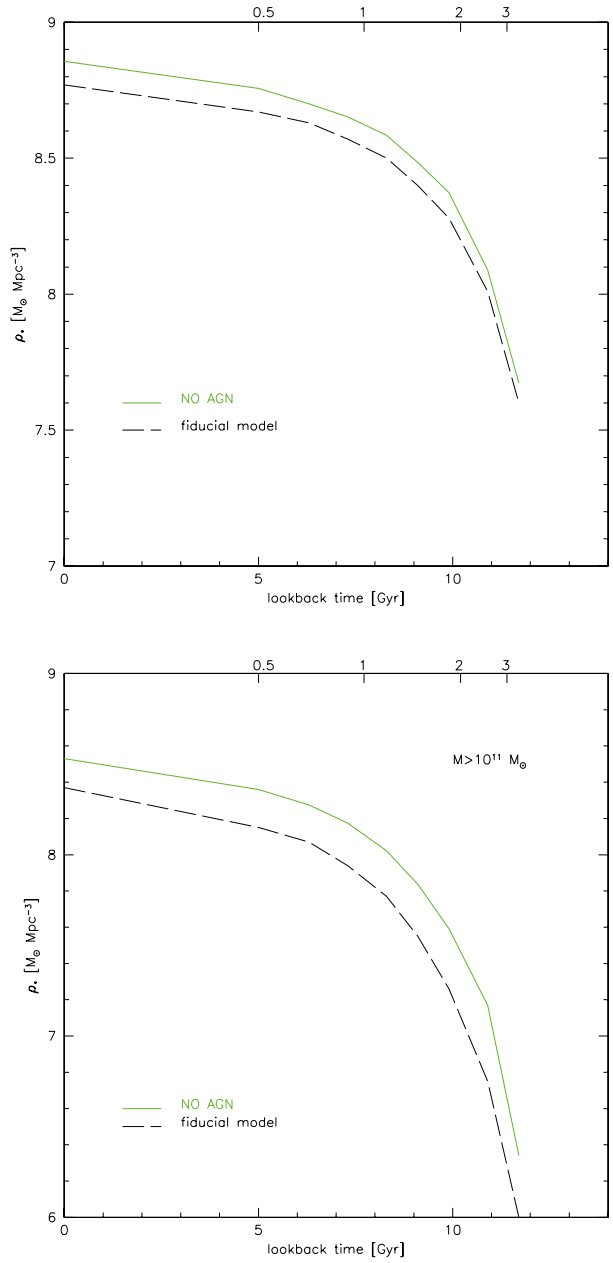

FIGURE 6.3— Comparison between the stellar mass density for the model without AGN feedback (green line) and the fiducial model (dashed line). In the upper panel the total stellar mass density is shown, while in the lower panel the mass density as obtained from the integration of the high-mass end of the mass function ($M \geq 10^{11} M_\odot$) is indicated.

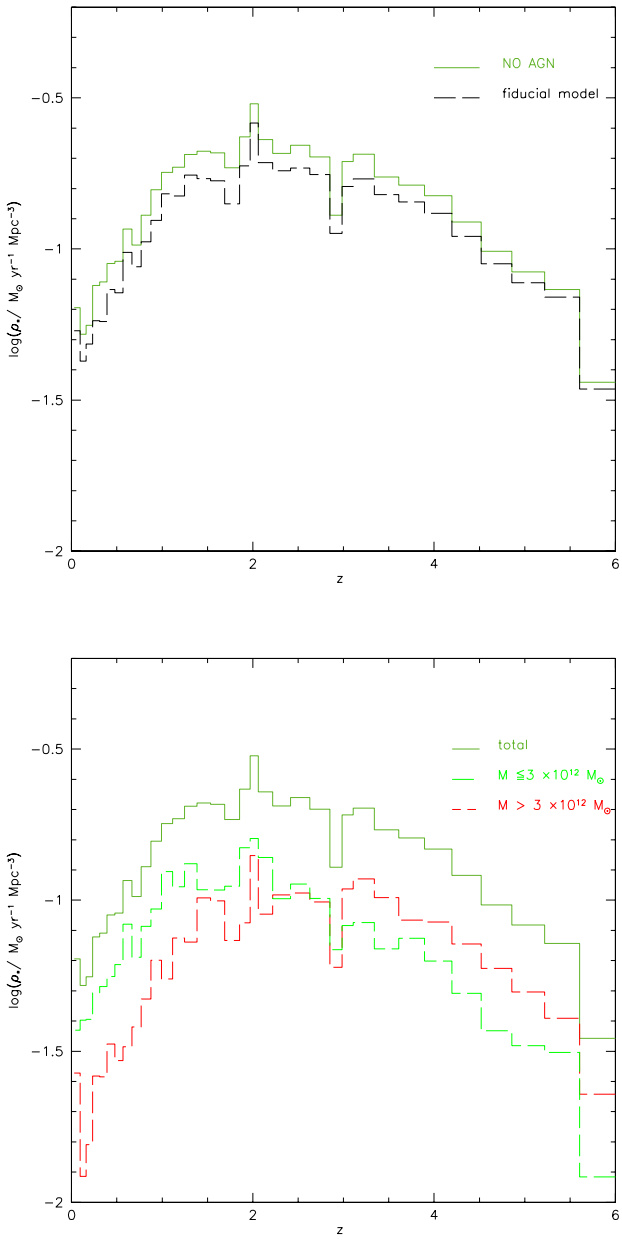

FIGURE 6.4— *Upper panel*: comparison between the comoving star formation density as a function of redshift for the model without AGN feedback (green solid line) and that of the fiducial model (black dashed line). *Lower panel:* the total star formation density for this model is splitted in the contribution for galaxies living in high-mass haloes (red long-dashed line) and in low-mass ones (light green, short-dashed line).

comparison of the stellar mass density in the two models (figure 6.7) shows that in the case of enhanced star formation, the mass assembly proceeds faster at high redshift and then slows down at recent cosmic time. Half of the total present-day stellar mass density in this model is in place at $z \sim 2$, while in the fiducial case it is assembled at $z \sim 1.5$. The accelerated evolution in the Model 2 is confirmed even in figure 6.8, where at high redshift the difference between the two models decreases at late cosmic times. Moreover, in this case, the decline in the SFR between $z \sim 1.5$ and $z = 0$ is much more drastic than that found in the fiducial model. In the lower panel of the same figure we show that even in this case the *downsizing* in star formation is reproduced.

The effect of increasing the star formation rate is therefore to increase the stellar content both in the disks and in the bulges at all redshifts. The star formation and mass assembly in this case proceed faster at high redshift, and then slow-down at low redshift, because the fast consumption of gas at high redshift, due to the enhanced star formation efficiency, leads quite soon to the exhaustion of gas.

6.4 Model 3: no burst

In the model 3 we turn off the star formation in the starbusrt mode, allowing only the quiescent star formation. From figure 6.9 we notice that the total stellar mass function keeps unchanged. Since the starburst mode is no more effective, the only mechanism for the formation of bulges is that of major mergers, when all the stars in the merging disks are added to the bulge component. This leads to a slight underprediction of the bulge mass function compared to the fiducial case, and to an overprediction of disks, even if the differences are small.

Looking at the high redshift mass function in figure 6.10, one can notice that at $z \sim 1$ the mass function in the model without burst is somehow underpredicted with respect to the fiducial model. Given that at $z = 0$ the two models leads to nearly identical SMF, this means that the amount of evolution is slightly higher without the inclusion of the starburst of star formation. This hints at a faster evolution at low redshift and it is confirmed looking at the stellar mass density of figure 6.11. When no burst is included in the model the present-day stellar mass density is assembled later with respect to the model where bursts are allowed. The star formation rate density confirms this trend. In figure 6.12, the comparison between the model with (fiducial model) and without (model 3) burst indicates that the starburst enhances the star formation at high redshift. Down to $z \sim 2$, the star formation in the model without burst keeps higher, and then it equals and then overcomes the star formation of the fiducial model at $z \lesssim 1$. The bottom panel of figure 6.12 indicates that *downsizing* is still reproduced in Model 3, in fact high-mass systems ceases to form stars earlier than low-mass objects, although at high redshift the two star formation paths are almost indistinguishable, at variance with the fiducial model, where the star formation in high-mass systems is much higher at earlier epochs (see figure 5.12).

Therefore, although the local stellar mass function is well matched in both models, the inclusion of the starburst mode of star formation leads to quite different predictions

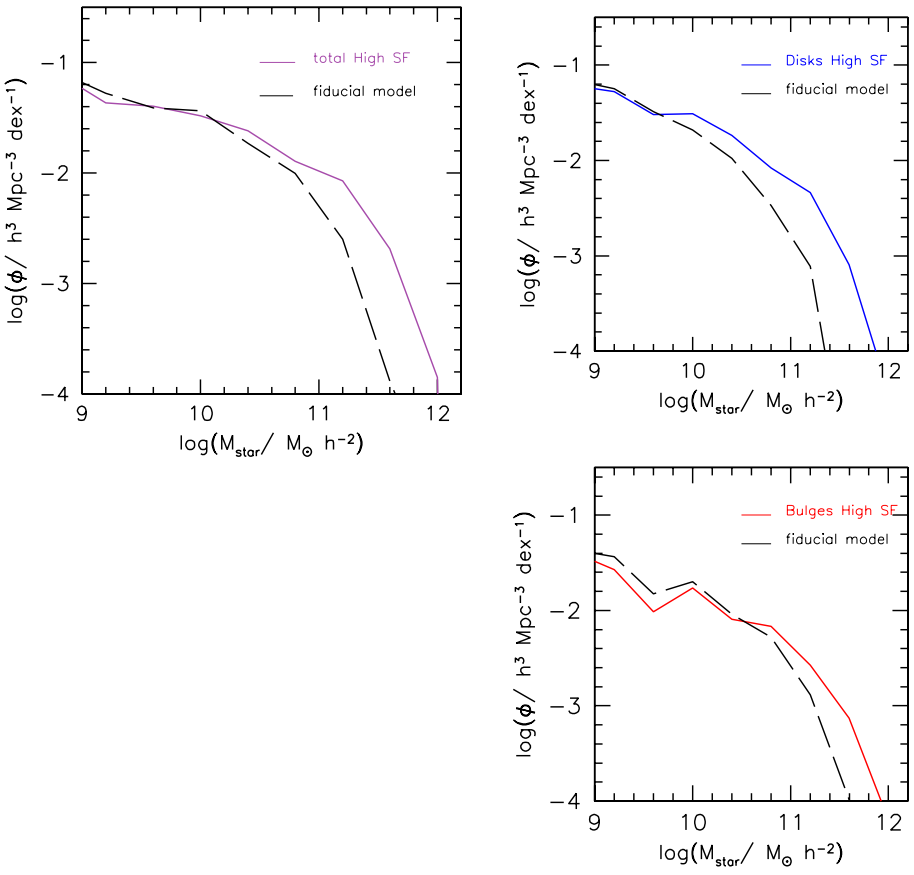

FIGURE 6.5— Comparison between the local stellar mass function for the model with high SF efficiency and the fiducial model. In the upper-left panel the total SMF for the model with high SF efficiency is shown by the green solid line, while the black dashed line represents the fiducial model. In the right-upper panel and in the right-lower one the mass function of the disk and of the bulge component, respectively, are indicated with the solid (blue and red) lines. The dashed black line is again the prediction of the fiducial model.

about the high-redshift universe, with an earlier epoch of star formation and mass assembly when starbursts are included. Indeed, starbursts are more effective at high redshift, when mergers are more frequent, and a larger amount of cold gas is available. As cosmic time increases, the major channel of star formation is the quiescent one, hence the star formation in both cases depends above all on the star formation efficiency α.

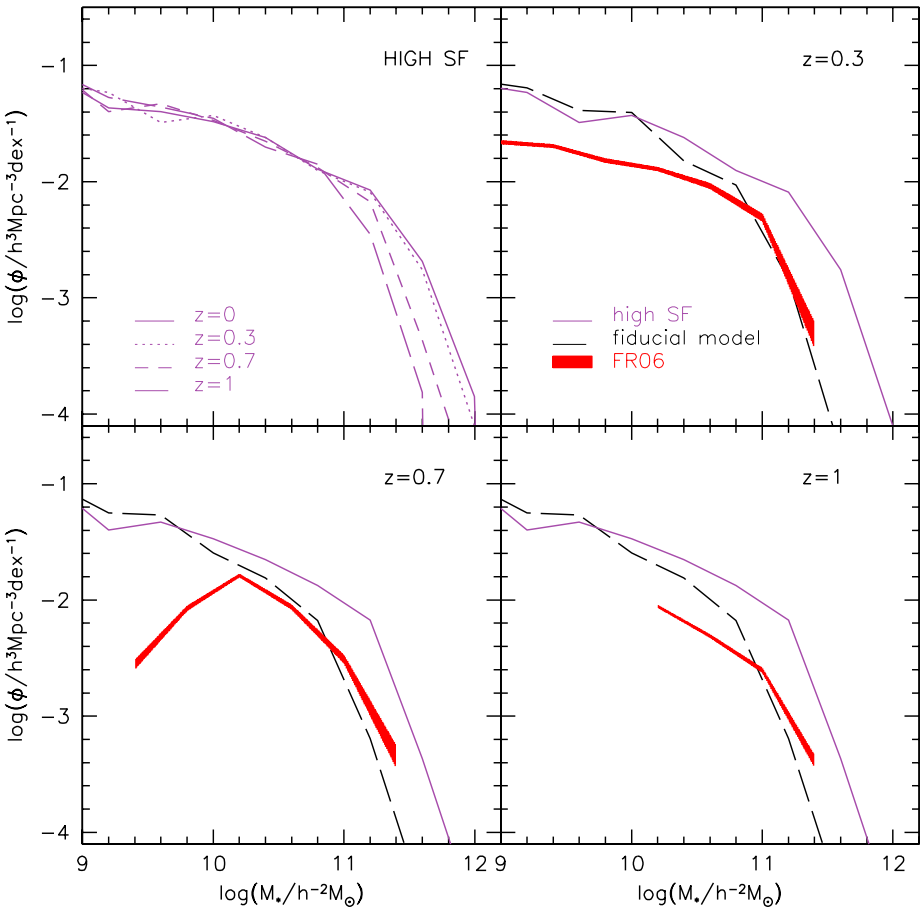

FIGURE 6.6— Evolution of the stellar mass function in the model with high SF efficiency. In the first panel the mass function at different redshift for this model are indicated. In the other panels the evolved mass function (green lines) are compared with the observations of Franceschini et al. (2006) (red shaded region) at the corresponding redshift and with the fiducial model (dashed black line).

6.5 Model 4: low SN feedback

The last model that we explored is a model with a low value for the SN feedback efficiency ϵ_{SN}. As discussed in Chapter 4, SN feedback is effective only in galaxies living in low-mass haloes, since the amount of gas reheated by this form of feedback is inversely proportional to V_c^2 (see eq. 4.14). As a consequence of this, lowering the SN feedback efficiency has the main effect of increasing the faint-end of the local mass function, as shown by panel *a* of figure 6.13. Nevertheless, even the high-mass systems are overabundant with respect to the fiducial case. The reason for that is clear from the behaviour of the disk and bulge mass functions. SN feedback is effective in reducing

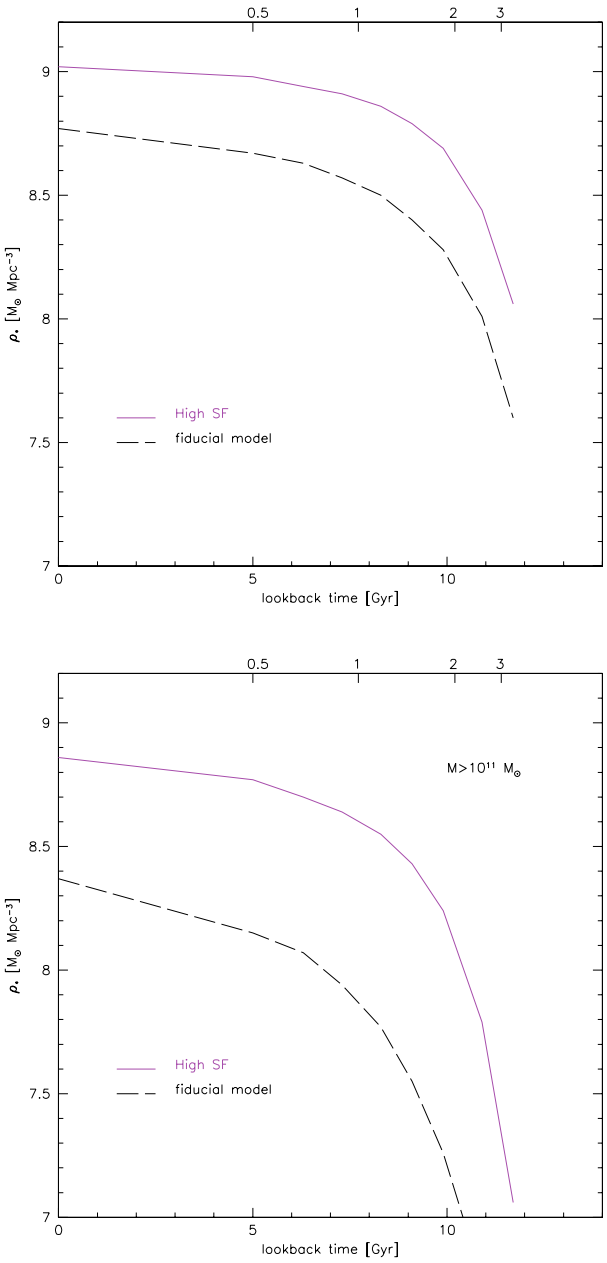

FIGURE 6.7— Comparison between the stellar mass density for the model with high SF efficiency (green line) and the fiducial model (dashed line). In the upper panel the total stellar mass density is shown, while in the lower panel the mass density as obtained from the integration of the high-mass end of the mass function ($M \geq 10^{11} M_{\odot}$) is indicated.

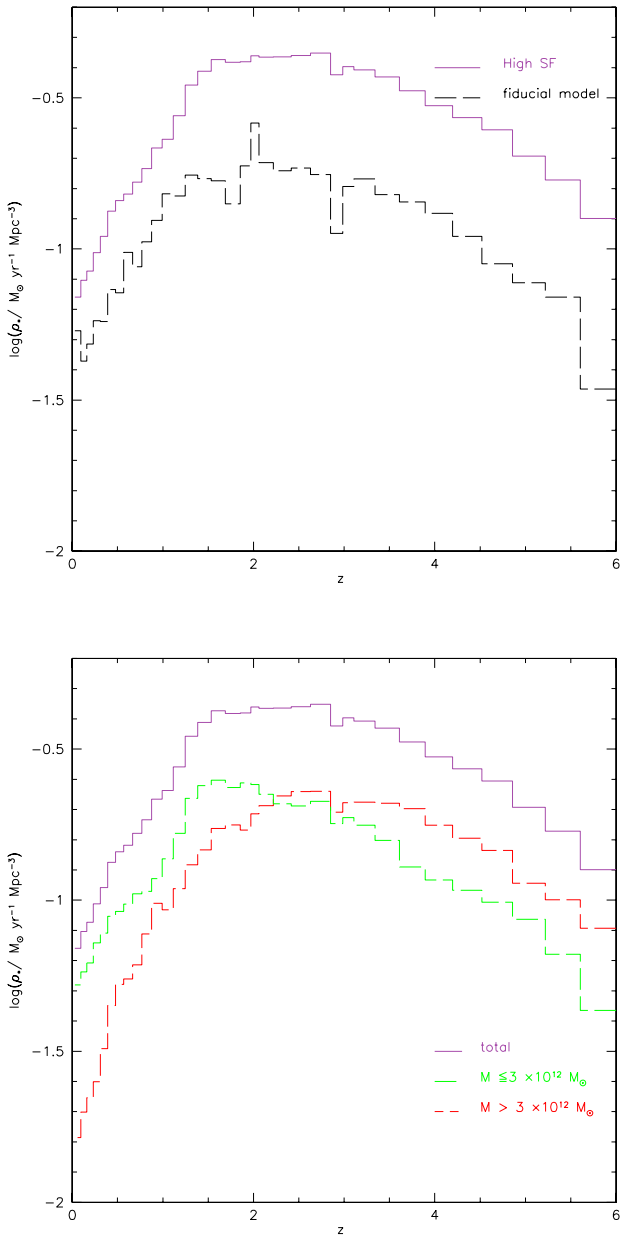

FIGURE 6.8— *Upper panel*: comparison between the comoving star formation density as a function of redshift for the model with high SF efficiency (green solid line) and that of the fiducial model (black dashed line). *Lower panel:* the total star formation density for this model is splitted in the contribution for galaxies living in high-mass haloes (red long-dashed line) and in low-mass ones (light green, short-dashed line).

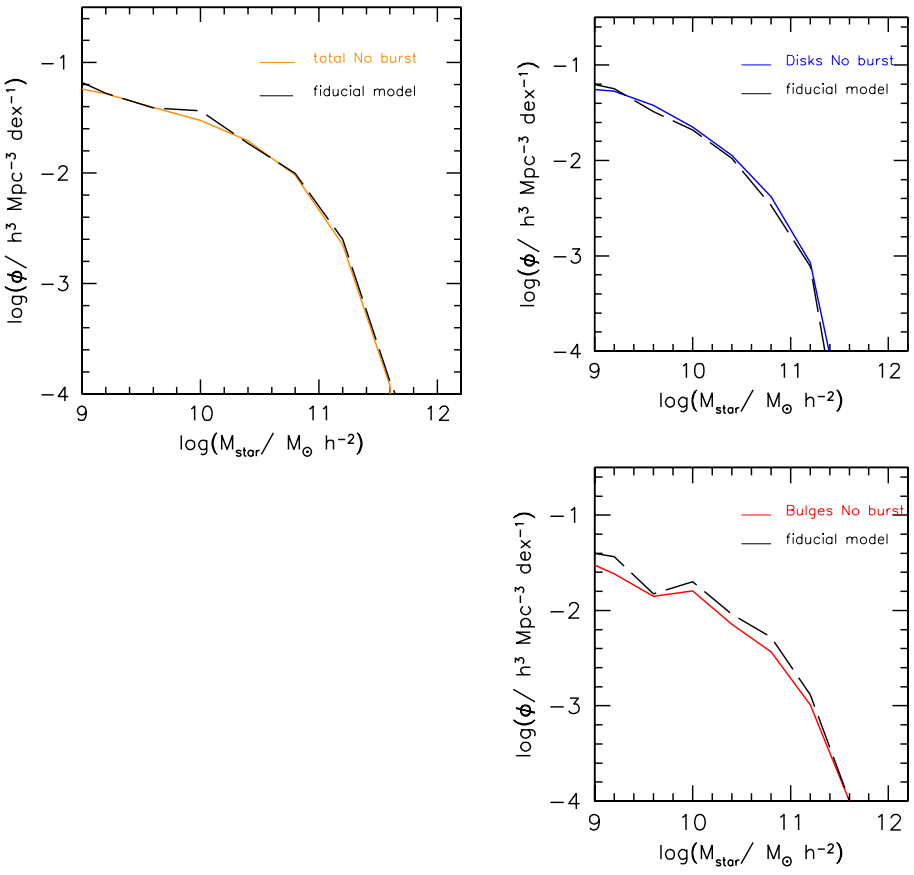

FIGURE 6.9— Comparison between the local stellar mass function for the model without bursts and the fiducial model. In the upper-left panel the total SMF for the model without bursts is shown by the green solid line, while the black dashed line represents the fiducial model. In the right-upper panel and in the right-lower one the mass function of the disk and of the bulge component, respectively, are indicated with the solid (blue and red) lines. The dashed black line is again the prediction of the fiducial model.

the quiescent star formation, and hence the mass of the disk component. Therefore it affects only the faint-end part of the disk mass function (panel *b*). Concerning the bulge mass function (panel *c*), a reduced SN feedback lead to mergers between higher mass disks, that end up with a massive spheroid, hence increasing the bright-end of the bulge mass function and, at the same time, that of the total mass function, that at high masses is dominated by the bulges.

The evolution of the mass function, as shown by figure 6.14, is similar to that of the fiducial model. In particular the faint-end of the mass function keeps higher compared

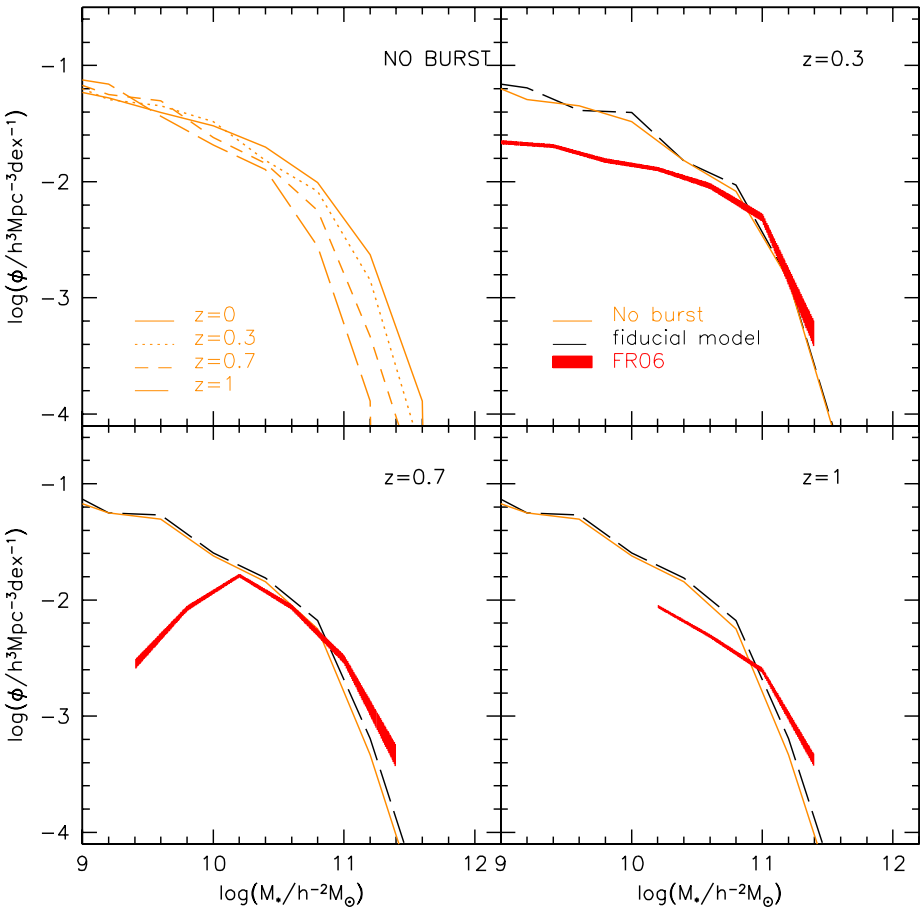

FIGURE 6.10— Evolution of the stellar mass function in the model without bursts. In the first panel the mass function at different redshift for this model are indicated. In the other panels the evolved mass function (green lines) are compared with the observations of Franceschini et al. (2006) (red shaded region) at the corresponding redshift and with the fiducial model (dashed black line).

to the fiducial model, and hence to the observations, at all the redshifts probed here. Because of the overabundance of both low-mass and high-mass galaxies in Model 4, the stellar mass density of this model is higher than the fiducial case, mainly at low redshift, indicating a faster mass assembly (figure 6.15). Indeed the star formation rate density, shown in figure 6.16, indicates that the SFR of galaxies with a low value of SN feedback, is always higher compared with the fiducial case, especially at low redshift. Even in this last model explored, the *downsizing* nature of star formation is still reproduced, as indicated by the different timescales of star formation for high-mass and low-mass systems (lower panel of figure 6.16).

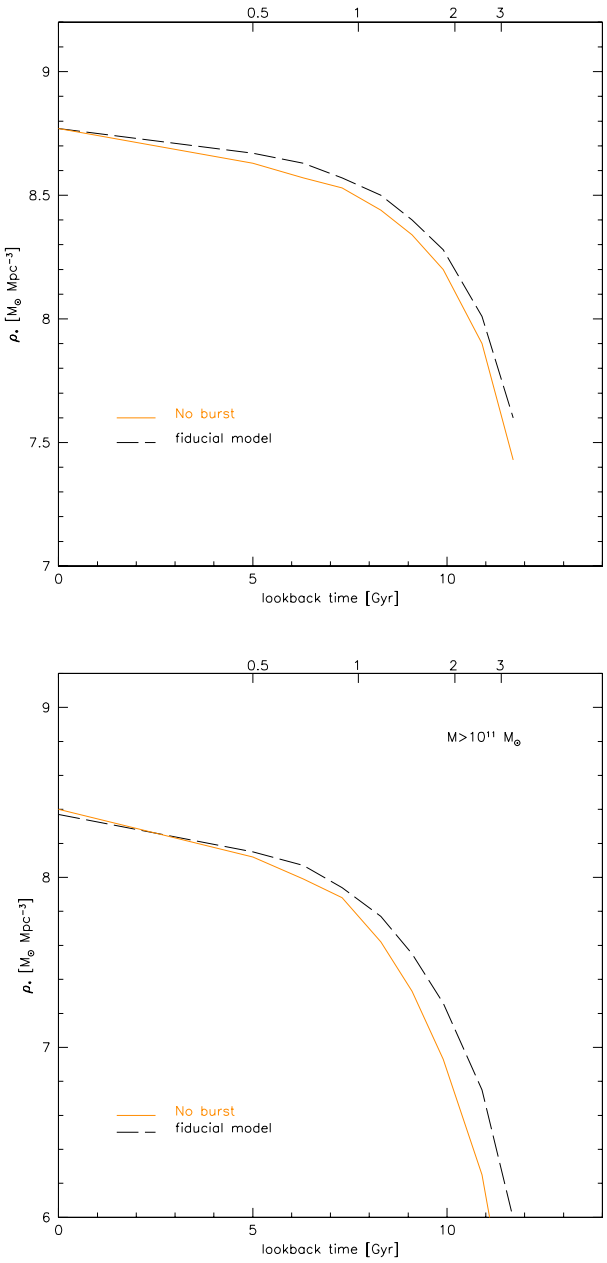

FIGURE 6.11— Comparison between the stellar mass density for the model without bursts (green line) and the fiducial model (dashed line). In the upper panel the total stellar mass density is shown, while in the lower panel the mass density as obtained from the integration of the high-mass end of the mass function ($M \geq 10^{11} M_{\odot}$) is indicated.

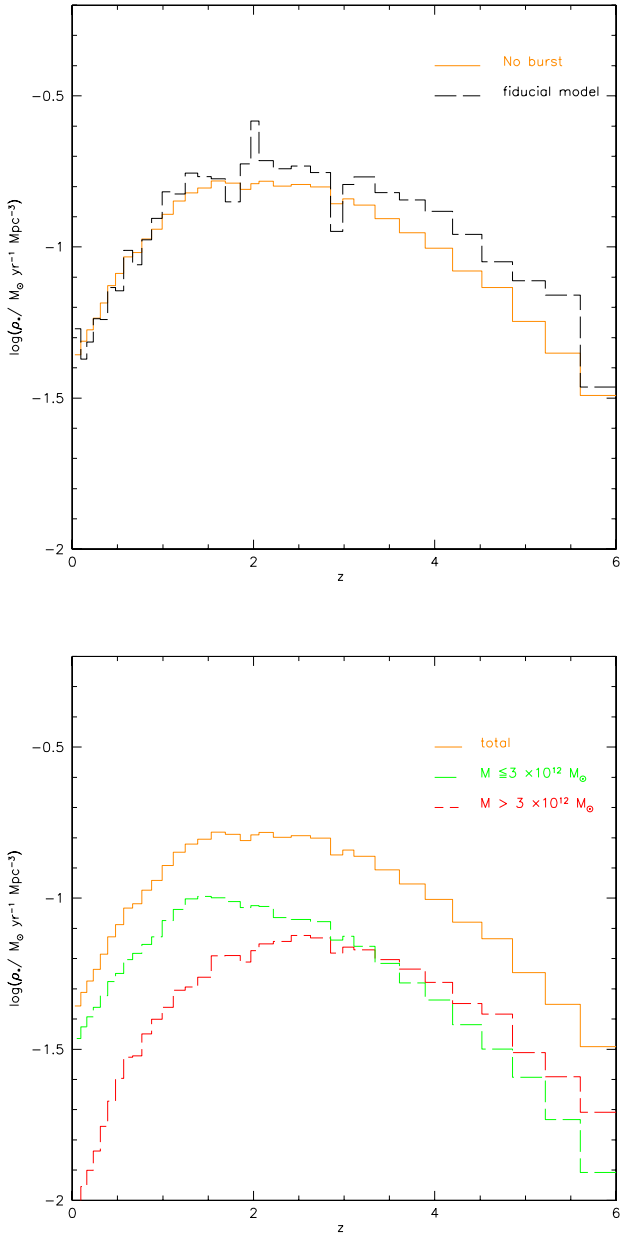

FIGURE 6.12— *Upper panel*: comparison between the comoving star formation density as a function of redshift for the model without bursts (green solid line) and that of the fiducial model (black dashed line). *Lower panel:* the total star formation density for this model is splitted in the contribution for galaxies living in high-mass haloes (red long-dashed line) and in low-mass ones (light green, short-dashed line).

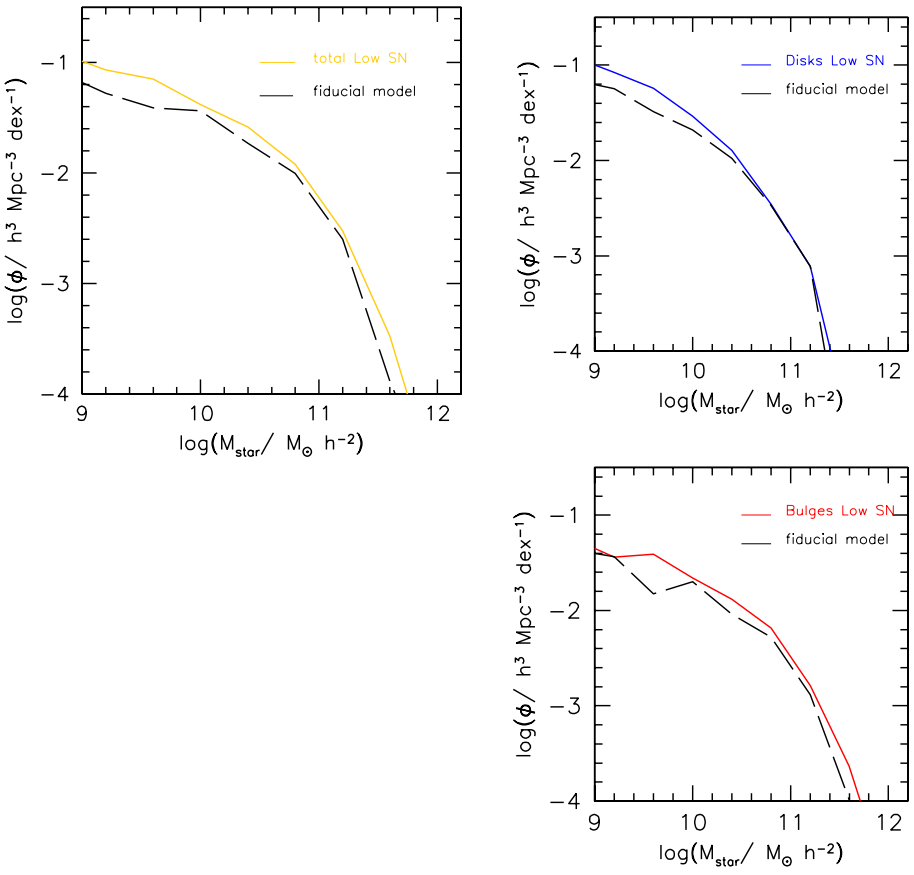

FIGURE 6.13— Comparison between the local stellar mass function for the model with low SN feedback and the fiducial model. In the upper-left panel the total SMF for the model with low SN feedback is shown by the green solid line, while the black dashed line represents the fiducial model. In the right-upper panel and in the right-lower one the mass function of the disk and of the bulge component, respectively, are indicated with the solid (blue and red) lines. The dashed black line is again the prediction of the fiducial model.

6.6 Summary

In this Chapter we investigated the importance of the different free parameters introduced in GECO, namely the efficiency in the star formation in the quiescent and bursty mode, and that of the feedback from SN and from AGN. We build 4 models, obtained from a slight variation from the fiducial model described in Chapter 5. In order to understand their effect, we first compare the resulting local stellar mass function with that of the fiducial case, and then a set of results concerning the high redshift universe,

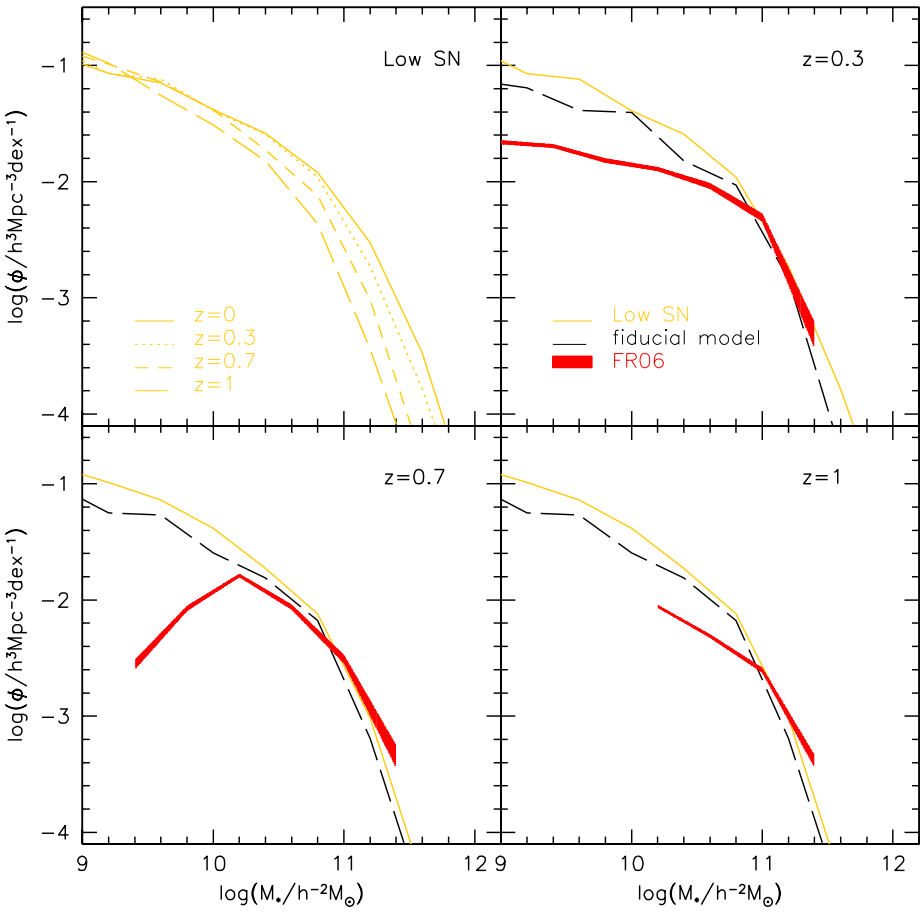

FIGURE 6.14— Evolution of the stellar mass function in the model with low SN feedback. In the first panel the mass function at different redshift for this model are indicated. In the other panels the evolved mass function (green lines) are compared with the observations of Franceschini et al. (2006) (red shaded region) at the corresponding redshift and with the fiducial model (dashed black line).

that are the evolution of the stellar mass function, the stellar mass density and the star formation rate density as a function of redshift.

The local mass function is shaped by all the parameters introduced above. Switching off the AGN feedback (Model 1) results in an excess of the bright-end mass function, mainly because of an excess of bulges. The same overabundance is seen in the case of enhanced star formation (Model 2) , even if in this case both disks and bulges are more massive compared with the fiducial model. The suppression of starbursts (Model 3) has no effect on the total mass function, but the contribution from the disks is now more important than that of the bulges. Finally, the effect of SN feedback is

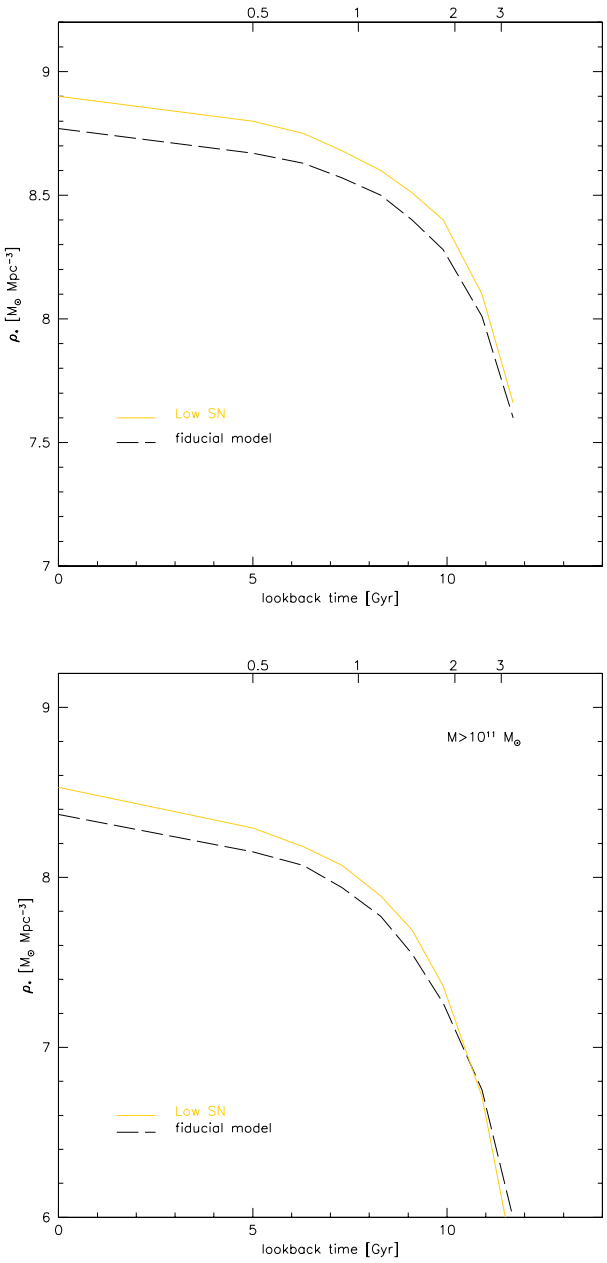

FIGURE 6.15— Comparison between the stellar mass density for the model with low SN feedback (green line) and the fiducial model (dashed line). In the upper panel the total stellar mass density is shown, while in the lower panel the mass density as obtained from the integration of the high-mass end of the mass function ($M \geq 10^{11} M_\odot$) is indicated.

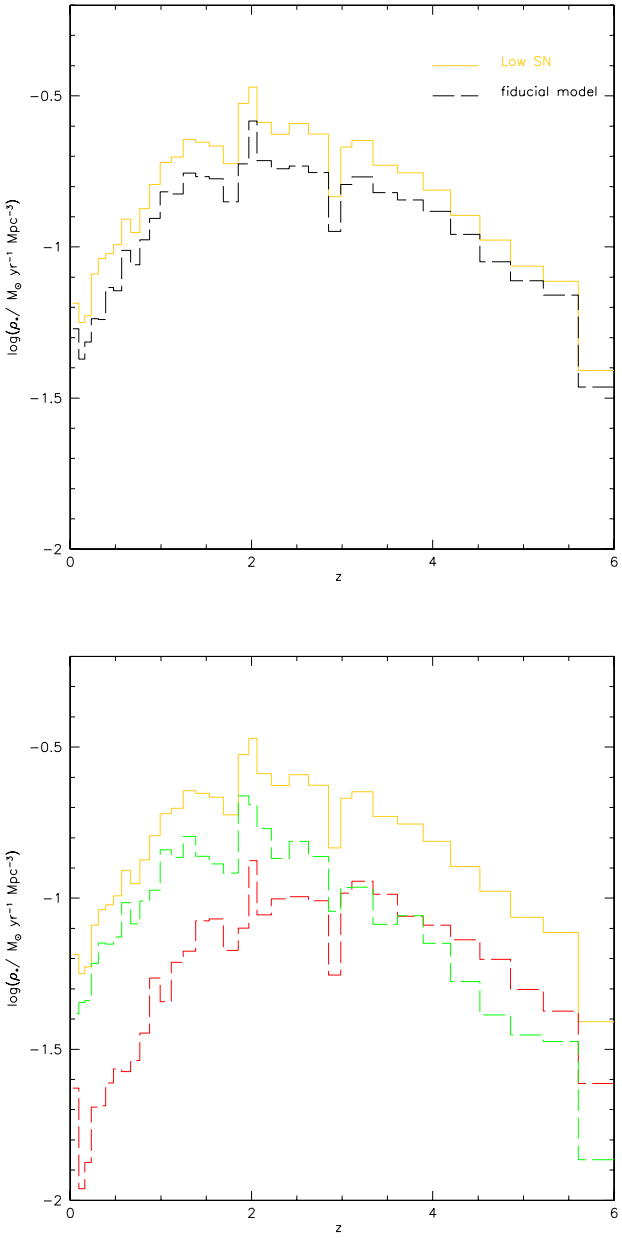

FIGURE 6.16— *Upper panel*: comparison between the comoving star formation density as a function of redshift for the model with low SN feedback (green solid line) and that of the fiducial model (black dashed line). *Lower panel:* the total star formation density for this model is splitted in the contribution for galaxies living in high-mass haloes (red long-dashed line) and in low-mass ones (light green, short-dashed line).

investigated lowering the SN feedback efficiency (Model 4), that leads to an excess of low-mass systems (mainly disks) and a slight overabundance of bright objects (mainly bulges).

The evolution of the mass function in all the models probed leads to similar evolutionary paths. A modest evolution of the high-mass tail between $z \sim 1$ and the present-day, and little evolution of the faint-end. Anyway, the timescales for star formation and mass assembly can be quite different among different models. For example in the case of suppression of starburst (Model 3) the star formation is delayed with respect to the fiducial model. On the contrary, if the quiescent star formation is enhanced (Model 2) star formation is increased mainly at high redshift, leading to an earlier mass assembly of galaxies.

Moreover, in all the models probed here, we find that star formation proceeds in a *downsizing* fashion, as indicated by the different path in the Madau plot followed by galaxies living in haloes with different mass.

7

Colour bimodality in COSMOS

In this Chapter we present a study on the galaxy bimodality with COSMOS/zCOSMOS data. Taking advantage of the huge amount of data provided by COSMOS we study the build-up of the rest-frame colour-mass relation with redshift, up to $z \lesssim 1$. The high-precision spectroscopic data, within the zCOSMOS collaboration, provide us also the opportunity to investigate the dependence of this build-up on the environment for a subsample of galaxies in the COSMOS field.

7.1 Description of the Survey

The Cosmic Evolution Survey (COSMOS) is the largest HST survey ever undertaken – imaging with the ACS camera an equatorial field with area $\sim 2deg^2$ with single-orbit I-band exposures to a point source depth of I_{AB} =28 mag and 50% completeness for galaxies $0.5''$ in diameter at I_{AB} = 26.0 mag (Scoville et al. 2007).

The COSMOS field is a $1.4^\circ \times 1.4^\circ$ square, centered at RA = 10:00:28.6 , DEC = +02:12:21.0. Its large areal coverage is motivated to sample the largest structures existing in the local universe since smaller area coverage leads to severe cosmic variance. Moreover it allows to sample a volume in the high redshift universe approaching that sampled locally by the Sloan Digital Sky Survey (SDSS). Figure 7.1 shows the results of a ΛCDM simulation for $z = 1$ and $z = 2$ (Frenk et al. 2000). The grey scale represents the dark matter distribution, while coloured dots are the galaxies living inside them, simulated with the SAM technique, where the size encodes the magnitude expected in the I-band. The large area of the COSMOS field allows to sample the largest expected structures ($M \sim 2 \times 10^{14} M_\odot$), while other field, such as GOODS and HDF, that are shown for reference, sample much lower scales.

Since the COSMOS field is located near the celestial equator, it ensures visibility by all astronomical facilities. Extensive multi-λ ground and space-based observations of this field have been gathered, spanning the entire spectrum from X-ray, UV, optical/IR, mid-infrared, mm/submm and to radio with extremely high sensitivity imaging

and spectroscopy. This full spectrum approach is required to probe the coupled evolution of young and old stellar populations, starbursts, the ISM (molecular and ionized components), AGN and dark matter.

The extensive allocations on Subaru, CFHT, UKIRT and NOAO have provided extremely deep photometry for 12 bands from U to K_s, enabling accurate photometric redshift measurements, integrated colours and colour selection of populations for essentially all objects detected in the $2deg^2$ ACS field. The photometry catalogs from these data contain over 2 million objects at <27 mag (AB) in the U to K_s bands (Mobasher et al. 2007).

COSMOS is designed to probe the correlated evolution of galaxies, star formation, active galactic nuclei (AGN) and dark matter with large-scale structure (LSS) up to $z \sim 6$ (Scoville et al. 2007) The scientific goals of the survey address nearly every aspect of observational cosmology over the majority of the Hubble time, out to z ~ 6 :

- the assembly of galaxies, clusters and dark matter on scales up to $\geq 2\times10^{14}M_{\odot}$;
- reconstruction of the dark matter distributions and content using weak gravitational lensing at z < 1.5;
- the evolution of galaxy morphology, galactic merger rates and star formation as a function of LSS environment and redshift;
- evolution of AGN and the dependence of black hole growth on galaxy morphology and environment;
- the mass and luminosity distribution of the earliest galaxies, AGN and intergalactic gas at z = 3 to 6 and their clustering.

Since COSMOS is the largest contiguous area ever imaged by HST it is destined to represent the reference field for future studies of observational cosmology.

7.1.1 zCOSMOS

A large spectroscopic program (zCOSMOS) at VLT/VIMOS instruments in the COSMOS field is being undertaken as an ESO large program (~ 600 hours of observations) in order to provide spectra and redshifts for ≥ 30000 galaxies (Lilly et al. 2007). The survey consists of two parts: the *zCOSMOS-bright* and the *zCOSMOS-deep* catalogues. The bright sample is a magnitude limited sample selected to have $I_{AB} < 22.5$ and observed with the medium resolution grism, allowing the measurements of ~ 20000 galaxies up to $z \lesssim 1.2$. The deep sample is focused on higher redshift galaxies, with the goal of observing at lower resolution ~ 12000 galaxies in the range $1.4 < z < 2.5$ selected according to colour selection criteria: the *BzK* technique (Daddi et al. 2004) and the ultraviolet selection of Steidel et al. (2004).

Data reduction is carried out using the VIPGI software package, VIMOS Pipeline with Graphical Interface, (Scodeggio et al. 2005; Garilli et al. 2008). VIPGI undertakes standard processing of identification of objects in the slits, bias subtraction,

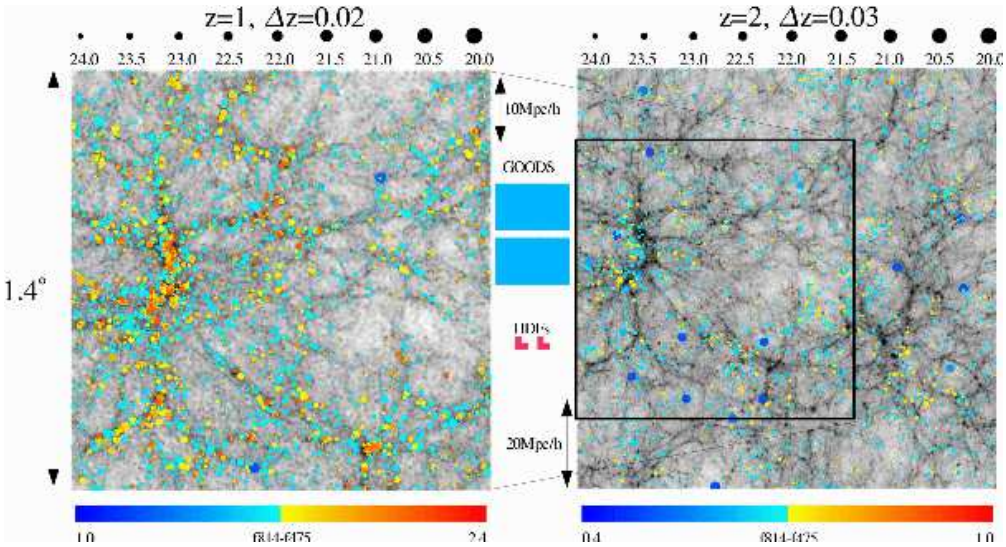

FIGURE 7.1— Λ-CDM simulation results for $2deg^2$ at z = 1 and 2, illustrating the scales of voids and wall regions and the 'expected' correlation of galaxy evolution with environmental density (Frenk et al. 2002). The gray-scale indicates the dark matter distribution and the symbols show magnitudes of galaxies computed for I-band. The depth of the redshift slice is $\Delta z = 0.02$ (50 Mpc at z = 1). Also shown are the HDF and GOODS field sizes. (Taken from Scoville et al. 2007)

flux and lambda calibration of the spectra, sky-lines subtraction, extraction of the one-dimensional spectra. Redshift are then measured in a multi-step process. A first measurement is made in a completely automatic way with KBRED and EZ softwares (Scaramella et al. 2007), based on cross-correlation with template spectra coupled with continuum fitting and principal-component analysis. This automatic step is followed by a visual inspection of every object to assess the validity of the automatic redshift. If the automatic procedure fails a new redshift is assigned by hand based on the wave-lenght of recognized features. Together with redshift a confidence class is assigned to each spectrum, which indicates the percentage of confidence in the measurement. This measurements are then repeated independently by a second person, followed by a "reconciliation" of the results. The duplication of the measurements and the final cross-check ensure the highest possible quality control on redshift.

In order to assess the accuracy of redshift measurements, 116 objects of the bright-sample were observed twice, and the whole reduction process with all its steps was made independently by different pairs of institutes. At the end the the measurements have been compared. Out of the 116 repeated objects, 90 were assigned the same redshift, and were used to determine an empirical estimate of the redshift accuracy, that turned out to be of $55kms^{-1}$.

The major goal of the spectroscopic survey is to understand the connection between the cosmic evolution of galaxies and the environment in which they live. A specific science goal is to derive measurements of the local density of each galaxy

with high precision, in order to correlate several galaxy properties with the environment. A second goal is the analysis of galaxy spectra to derive galaxy diagnostics, such as star formation, classification of AGN, stellar population ages, metallicities.

7.2 Data

In the present work we exploit the unique data set provided by the COSMOS/zCOSMOS survey to investigate the build-up of the colour-mass relation in the redshift range $0.2 - 1$ and its dependence on environment.

In particular we make use of the photometric multi-band catalogue with photometric redshift and stellar mass (Capak et al. 2007; Ilbert et al. 2008?) and the morphological information from the ACS imaging (Scarlata et al. 2007; Cassata et al. 2007). Concerning the spectroscopic subsample of galaxies, we make use of the 10*k* catalogue, available within the zCOSMOS collaboration, that includes a sample of $\sim$ 10000 galaxies with secure redshift up to $z \sim 1$. Measurements of absolute magnitude and stellar mass are described in Bolzonella et al. (2008), while ACS morphologies are described in Tasca et al. (2008).

7.3 Colour bimodality in COSMOS

We analyzed the colour-stellar mass relation for rest-frame optical $U - V$ colours. We choose the $U - V$ colour because it optimally brackets the Balmer break at 4000Å, that is a tracer of the past star formation activity of galaxies. Hence, this choice of colour allows to separate red and blue galaxies better than others.

In figure 7.2 we show the colour-mass relation for four bin of redshift, ranging from $z = 0.2$ up to $z = 1$. We realized that in the photometric catalogue used, stellar mass and absolute magnitudes are reliable up to the observed magnitude $I_{AB} = 24$, so we cut our sample to this magnitude, where even the morphological catalogue is complete. We end up with $\sim$ 20000 galaxies for redshift bin, as indicated in the panels. We compute the number density of points on a grid in the diagram and divide it in five percentiles of densities. We plot points according to the density interval they belong to: blue for the highest density region, followed by red, magenta, green and then cyan for the lowest density bin. Given the high number of points in the diagram, the density levels help us in finding the most populated regions in the colour-mass plane. We can distinguish two peak of density in each panel in the red and in the blue part of the diagram. Although at low redshift the red peak is well revealed in a red sequence, at higher redshift, the sequence tightens resembling more a cloud, but keeping well distinct from the blue one.

In the next section we will better quantify the transformations of the colour-mass relation during cosmic time, but here we can anticipate some trends, well visible from figure 7.2. As mentioned above, the red sequence becomes tighter as redshift increases, with the disappearance of the the faint-end part of the sequence. The effect is partly due to a selection effect, because faint galaxies at high redshift fall below the magnitude cut adopted and are not observable. Nevertheless, looking at the lowest redshift bin, a

second red peak in the red sequence in the low-mass end seems to be forming between $z \sim 0.5$ and $z \sim 0.3$. Moreover, while at low redshift the two sequences (or clouds) appear to be parallel, the blue sequence at high redshift becomes steeper and steeper. Even in this case, a selection effect may affect the diagram, as we will discuss below.

In figure 7.3 the colour-mass diagram is shown, with points coloured according to their morphology. Red points represent early-type galaxies and blue points represent late-type ones. The division in morphological types highlights the colour bimodality: the red sequence appears dominated by ellipticals, while the blue sequence is largely populated by late-type galaxies. In the small box in the right-hand of each panel, the colour distribution for each corresponding diagram is illustrated, with red and blue histogram representing, respectively, the early and late type population, while the black is for the total population. Coloured lines show the fit to the two sequences. Dashed lines represent the least square fit to the points, when the two populations are divided according to their colour: red for $U - V > 2$ and blue for $U - V < 2$. Solid lines represent a more robust fit, that we will describe in the following section, that is best-suited for representing the blue sequence, while, by visual inspection, it seems not to well describe the red sequence population, so in this case we will keep the least square value.

7.4 The build-up of the colour-mass relation with redshift

7.4.1 The faint-end of the Red Sequence

We analyze here the galaxy distribution on the red sequence. Several recent studies (Tanaka et al., 2005, De Lucia et al., 2006, Koyama et al., 2007) have demonstrated the existence of a deficit of faint red galaxies at high redshift compared with local observations, both in clusters and in the field. The faint end of the red sequence seems to be formed at relatively low redshift, while the bright end is already formed at $z \sim 1$, in agreement with the '*downsizing* scenario.

Throughout this work we prefer to consider the colour-mass diagram instead of the colour-magnitude one, and in this section we compute the relative contribution of the massive over low-mass objects, but we will speak about luminous-to-faint ratio, for analogy with other works. In order to define luminous and faint galaxies we equally divide the range of masses covered by red sequence galaxies in the highest redshift bin. In order to choose the minimum mass on the RS, we have to quantify the mass completeness of the sample, that is the mass above which virtually all masses, given the observed distribution, are included in the sample.

The flux limit in the I band imposed, translates at different redshifts into different lower luminosities and into a broad mass cut at each redshift that reflects the scatter in the Mass-Luminosity relation. We quantify this effect in the same way as done for instance in the VVDS survey (Meneux et al. 2007) and we illustrate the method in figure 7.4. We divide the redshift range in intervals of $\Delta z = 0.1$. In each redshift bin we compute the maximum absolute magnitude in the V band, V_{max}, detected at that distance, as the magnitude below which we find 95% of galaxies (dashed line in

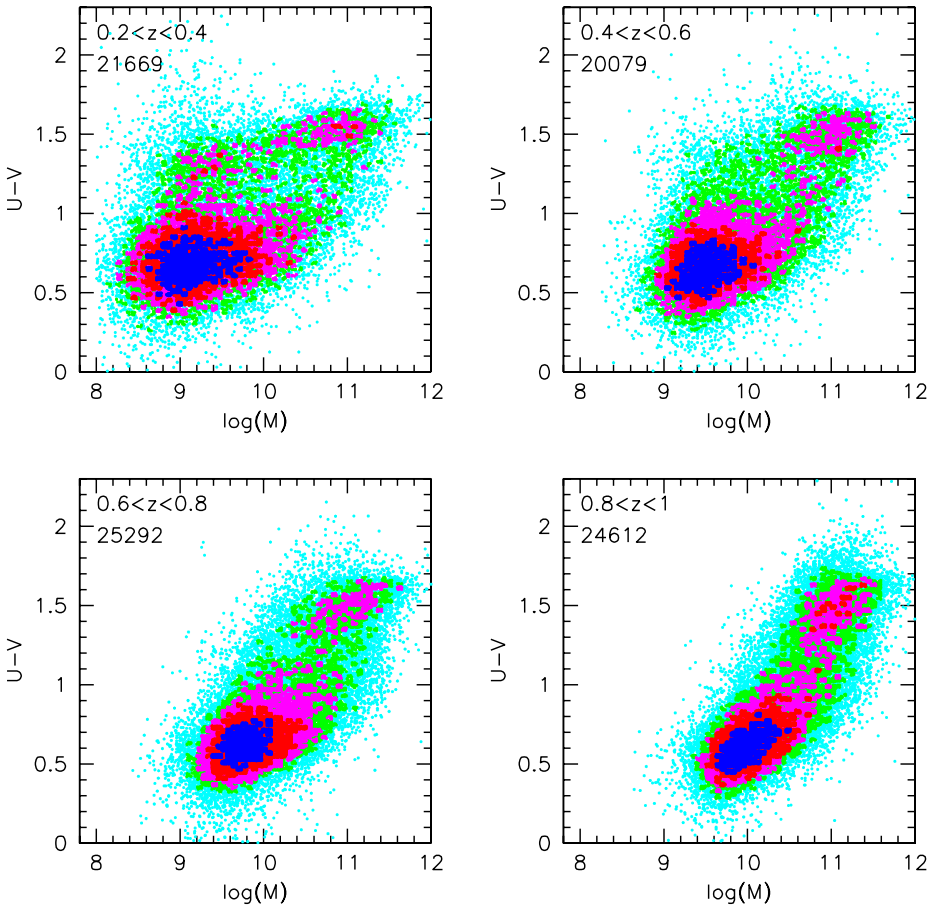

FIGURE 7.2— Rest-frame colour-mass relation for 4 redshift bin, ranging from $z = 0.2$ up to $z = 1$. Points are coloured according to the level in the number density they belong to (see text for further details).

panel *a* of figure 7.4). In the magnitude-stellar mass plot (panel *b* in the same figure) we consider a magnitude interval given by $[V_{max} : V_{max} + 0.3]$, that is the minimum interval which provides the statistics needed to compute mean and variance of the mass distribution. In panel *c* we show the mass distribution in this interval, and we take as completeness mass the value given by the mean of the distribution plus 1σ (right dashed line), which means that above this mass the sample is complete at better than 84%. In figure 7.5 we show the completeness V magnitude and stellar mass as a function of redshift (red points). We derive a completeness mass with logarithmic value of $log(M) = 10.7$ for $z = 0.9$, that is the mean redshift of our highest density bin, and of $log(M) = 10.4$ for $z = 0.7$.

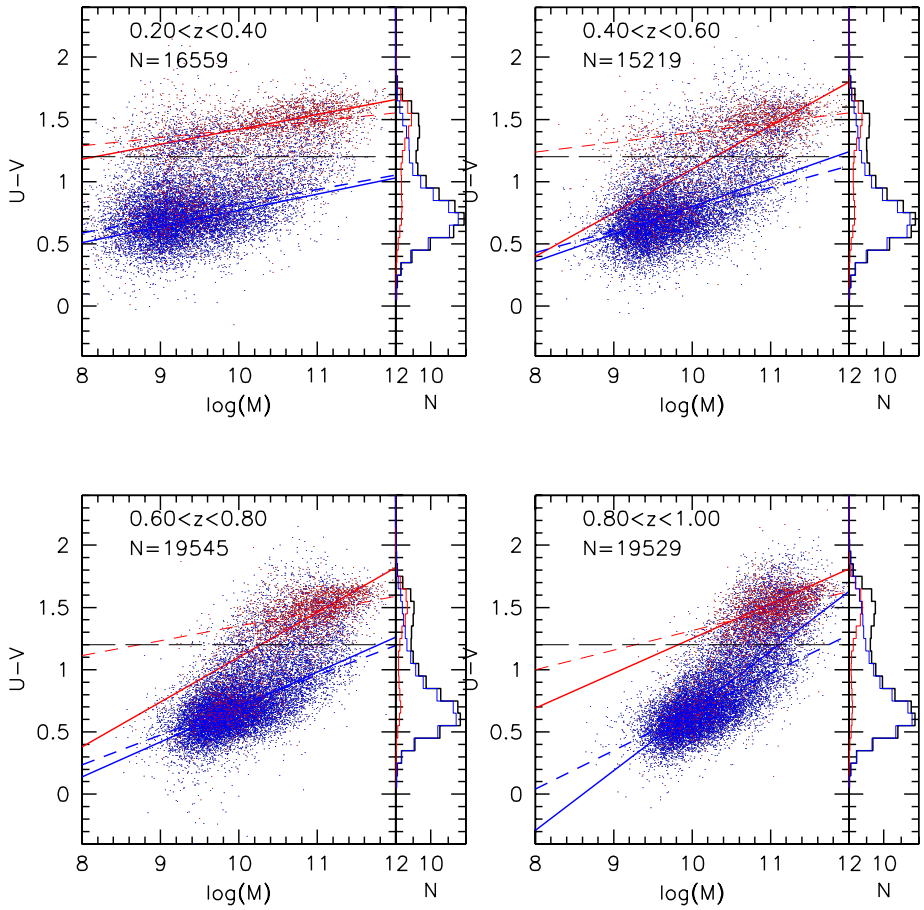

FIGURE 7.3— Colour-mass diagram at different redshift, red points stay for early-type galaxies and blue points for late-type. Red and blue lines are the fits to the red and blue sequence respectively, dashed for least square fit, and solid for a bidimensional Gaussian fit to the region with the highest density of points.

We compute the evolution of the faint end in two cases: from $z \sim 0.9$ to $z \sim 0.3$ (the lowest redshift bin), and from $z \sim 0.7$ to $z \sim 0.3$. In the first case, the minimum mass on the RS is given by $log(M) = 10.7$, that, dividing the range of mass above this limit into two equal parts, means that we have to use as a limit mass, discriminating between faint and luminous red galaxies, the value $log(M) = 11.25$. In the second case we use as a minimum mass $log(M) = 10.4$, that translates into a discriminating mass of $log(M) = 11.1$. We keep the same mass interval to define faint and luminous in all redshift bins. Therefore we compute the ratio between the number in the luminous and in the faint part of the RS at each redshift, and we illustrate them in figure 7.6 as a function of redshift. Errorbars are computed using Poisson statistics, with the

recipes valid for small numbers of Gehrels (1986). The evolution between $z = 0.7$ and $z = 0.3$, derived using the second definition of faint and luminous (faint are defined as galaxies in the range $10.4 < log(M) < 11.1$ and luminous have $log(M) > 11.1$), clearly shows that the faint-to-luminous ratio increases with redshift, indicating that the effect of progressive population of the faint-end of the sequence at low redshift, visible in figure 7.2, is real and not due to an artifact due to incompleteness effects. Considering the evolution between $z = 0.9$ and $z = 0.3$, and hence defining faint and luminous on the basis of the range of masses covered by RS galaxies at this high redshift (faint are defined as galaxies in the range $10.7 < log(M) < 11.25$ and luminous the ones with $log(M) > 11.25$) results in a lower amount of evolution, mainly in the highest redshift bin. We argue that this is due to the fact that at $z \sim 0.9$ we are probing only the high-mass part of the RS, that was already formed at earlier cosmic epochs, while the low-mass part is being progressively populated at $z \lesssim 0.7$.

7.4.2 Evolution of the Blue Sequence slope

As noted above, the slope of the blue sequence (BS) appears to increase with redshift. The high-mass end of the BS seems to reddens at high redshift, while the low-mass end becomes bluer. The key point is to understand if this effect is real or is due to the incompleteness of the sample, which varies with redshift and colour. Because of the magnitude cut adopted in the I band ($I_{AB} < 24$), blue galaxies are more easily observed than red galaxies with the same mass. In fact, at the considered redshifts, the selection in the observed I band translates in a selection in the rest-frame blue luminosity, where, by definition, blue galaxies are more luminous than their redder counterpart with the same mass. As a consequence, the minimum mass observed for blue galaxies is much smaller than the one for red galaxies. This translates in a diagonal cut in the colour-mass diagram which can enforce the slope to take higher values than real ones.

In order to compute the slope of the sequence in a more robust way, without be affected by such incompleteness, we consider only the regions of the diagram with the highest densities of points, since incompleteness is likely to affect only the outer regions of the sequence. We compute the fit to the sequence using a bidimensional Gaussian fit to the points distribution, using the IDL routine GAUSS2DFIT, which fits the points distribution with an ellipse. It returns the center of the distribution, the values of the axis, which are the widths of the Gaussian in the two orthogonal directions, and the position angle of the ellipse. In order to have convergence of the fit, it is needed a Gaussian-like distribution where the entire peak is contained out to at least 5 to 8 half-width. In figure 7.7 we show the results of the fit procedure for the blue sequence. Here we define blue sequence galaxies as late-type galaxies having a raw cut in colour: $U - V < 1.4$. Selecting BS galaxies only according to their colour results in a distribution with an horizontal cut, which is not desirable for the computation of the fit, because even the wings of the Gaussian distribution are required for the convergence. On the other hand, selecting only late-type systems may result in two peaks in the distribution which can give a wrong fit. The ellipses which

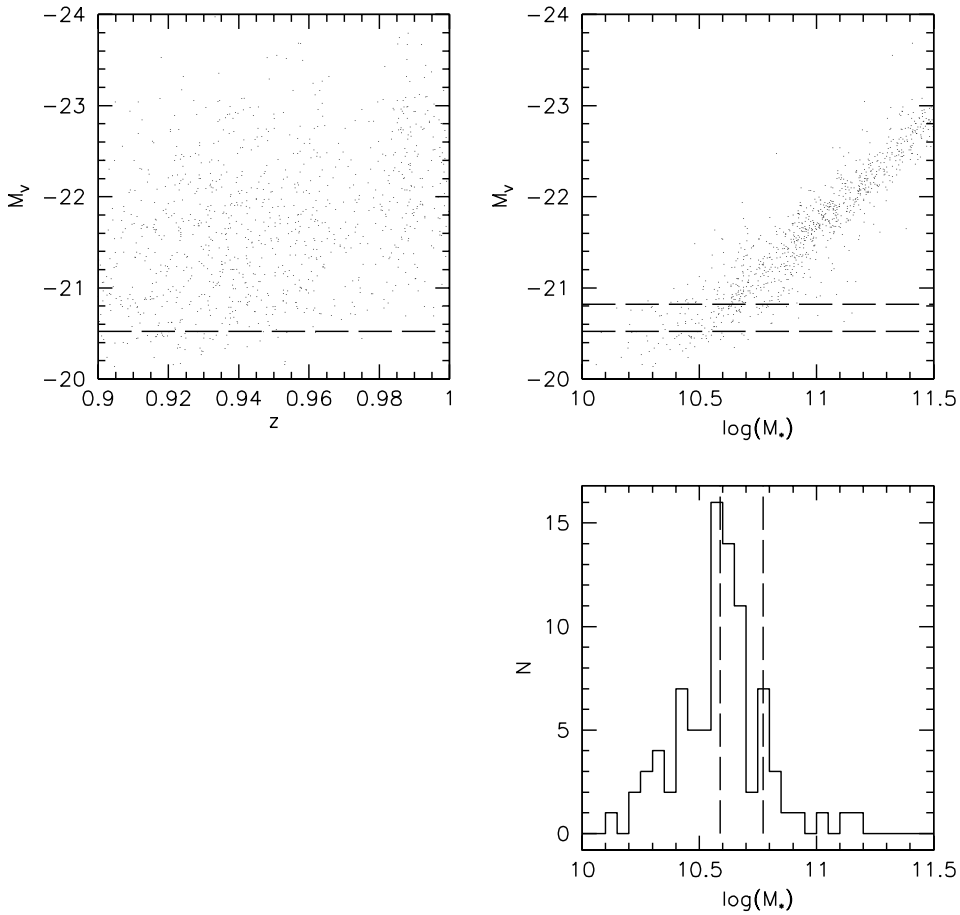

FIGURE 7.4— Example of the computation of the completeness limit of the survey in the redshift range 0.9-1. The top-right panel shows the absolute V magnitude versus redshift, the horizontal dashed line shows the magnitude limit, defined as the maximum magnitude below which we find 95% of the galaxies. The top-left panel shows the magnitude-stellar mass relation, where the two dashed lines indicate the range where points are selected in order to compute the stellar mass distribution in the bottom panel. The two dashed lines in the mass distribution represent respectively the mean of the distribution (left) and the mean plus 1σ (right). The last value is taken as completeness mass in the redshift range adopted.

fit the sequence are reported for the two highest density levels. Their major axis are taken as the slope of the sequence. Fit to the second level not always converges, and in that cases it is not reported.

In figure 7.8 we show the fit results for the red sequence (RS). Even here, RS galaxies are defined according to both morphology and colour criteria: they are defined as early-type galaxies with $U - V > 1$. In this case, the resulting fit is quite sensitive to the selection criterion adopted. Moreover, at high redshift, the RS resembles more

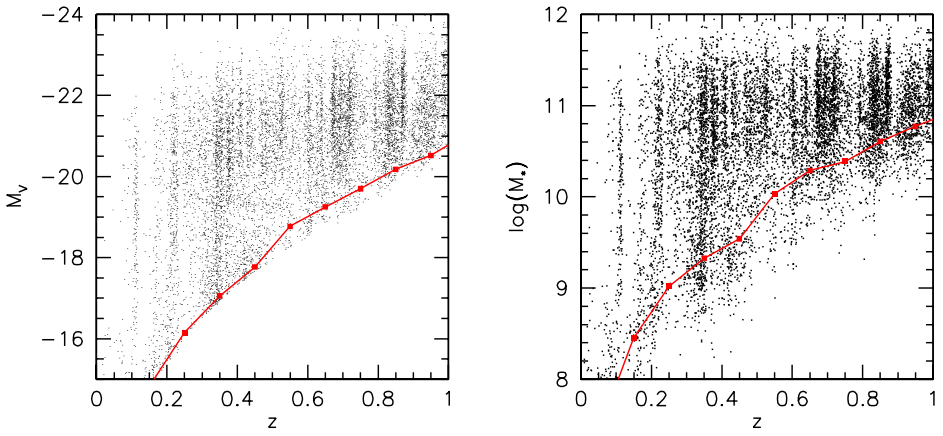

FIGURE 7.5— V magnitude (left panel) and mass (right panel) versus redshift for the COSMOS sample used. Red points show the the magnitude and mass completeness value computed in a redshift interval of 0.1 around the redshift indicated by the points.

a symmetric cloud than a sequence, due to the tightening, and hence the major axis of the ellipse is not well defined. For these reasons, we prefer to adopt as best-fit for the RS the value given by the least square fit, that in figure 7.3 seems to reproduce the red galaxies reasonably well at all redshifts considered.

We summarize the results of this section in figure 7.9 where we show the evolution of the slope as a function of redshift for the two sequences. The values for the slope of the BS (blue squares) are given by the two-dimensional Gaussian fit (figure 7.7) and errorbars are computed with a bootstrap resampling. We resampled the high-density region of the BS 100 times with replacement, we repeat the fitting procedure and we take the dispersion of the biweight estimator as our confidence interval. The value for

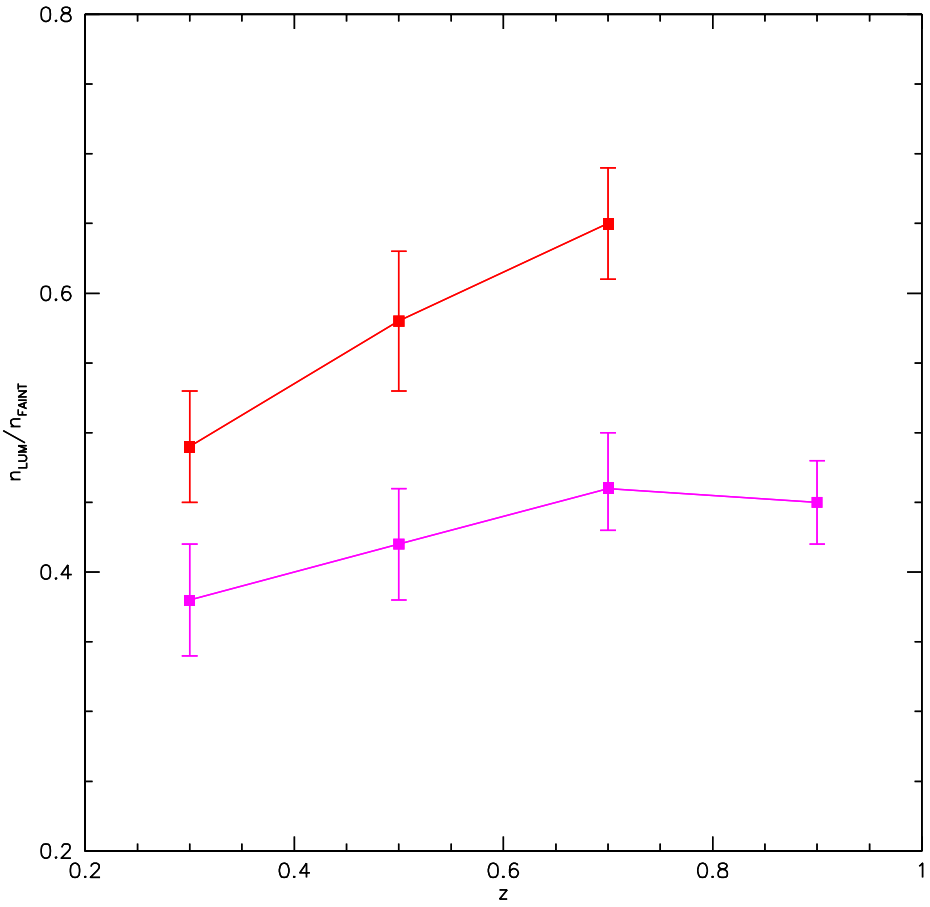

FIGURE 7.6— Evolution with redshift of the luminous to faint ratio in the case of luminous and faint defined at z=0.7 (red) and at z=0.9 (magenta). See text for further details.

the RS slopes are that given by the least square fit (figure 7.3) with the associated error. As already noted by a visual inspection of the colour-mass relation, the blue sequence steepens as redshift increases. By computing the best-fit for the BS using only points in the central region of the sequence, we can rule out to be affected by the variable incompleteness with colour. It is the first time that this effect is observed. A possible interpretation is in terms of a differential evolution of galaxies on the blue sequence. High-mass galaxies that at high redshift live on the blue sequence, quickly move to the RS as their star formation stops. As time goes on, galaxies progressively less massive exhaust their fuel and stop to form stars, becoming red sequence galaxies. This leads to a depauperation of the high-mass end of the blue sequence and to a population of the red-sequence even in the low-mass part. Consequently, the so called “green-valley”,

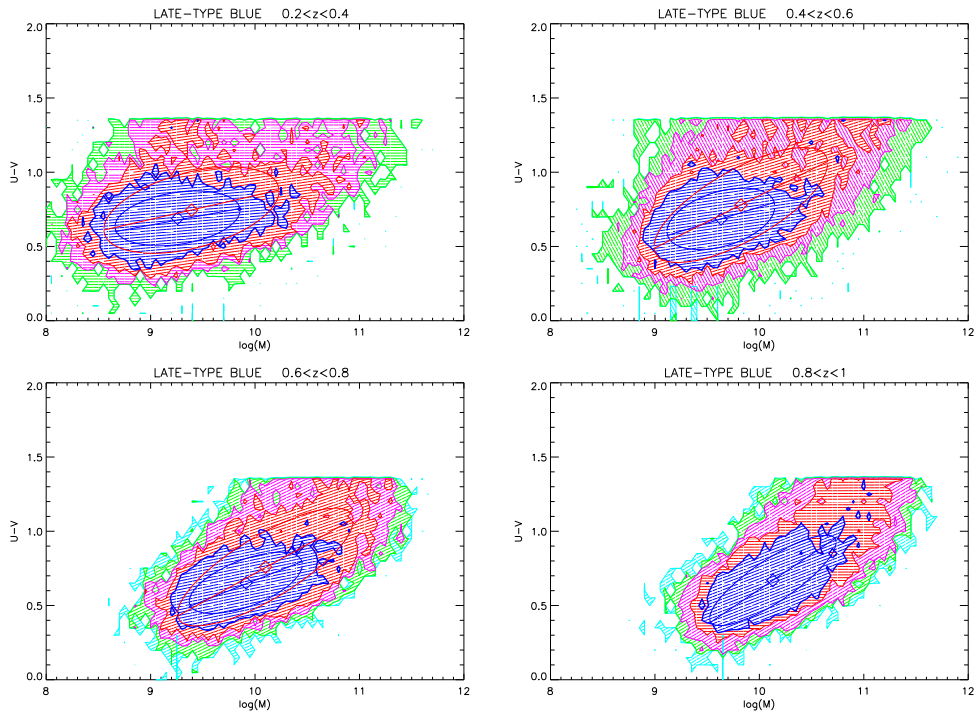

FIGURE 7.7— Contour plots for the blue sequence at different redshifts. Blue sequence galaxies are selected as late-type galaxies with a raw cut in colour ($U - V < 1.4$). Overplotted are the ellipses which fit the point distribution for different densities of points (blue stays for the highest level of density, and red for the second). The semi-major axis of the ellipse is taken as the slope of the sequence.

namely the minimum in the colour distribution between the red and the blue peak, is well visible in the low-redshift bins, while it is still populated by blue sequence galaxies at high redshift. This differential evolution of galaxies on the BS may also explain the build-up at low redshift of the faint end of the RS discussed in the previous section.

7.5 Dependence of the colour-mass diagram on the environment

Taking advantage of the high-precision spectroscopic redshift of zCOSMOS subsample, we can investigate here, the dependence of the colour-mass relation with environmental density. We use as environment tracer, the local density estimator, computed using the 5 nearest neighbours of the galaxy (Kovac et al. 2008) . In particular we take the overdensity $1 + \delta_5$, where δ_5 is the ratio between the local density and the mean density, and divide the sample in quartiles of overdensity.

In Figures 7.10-7.13 the colour-mass relation for different density bins is shown. The bimodality is present in each bin of overdensity for all the redshifts, but the relative abundance of the two populations changes with the density, with the RS becoming more populated with respect to the BS moving toward high density environments.

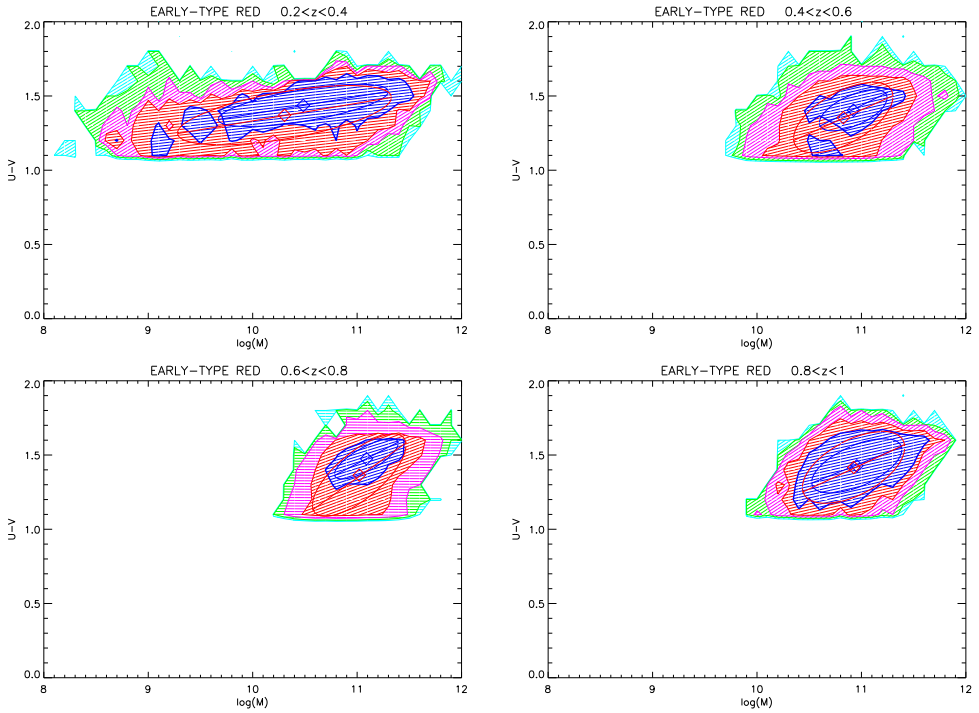

FIGURE 7.8— Contour plots for the red sequence at different redshifts. Red sequence galaxies are selected as early-type galaxies with a raw cut in colour ($U - V > 1$).

This effect is evident looking at the bottom-right panels. The median colour of the global population increases with $log(1+\delta_5)$ for all the redshift bin but the highest one.

It is interesting to note that considering early-type and late-type galaxies separately the median colour has no or slightly dependence on environment. Only in the lowest redshift bin (0.2-0.4) the median colour of the early-type galaxies slightly increases with local density, but it is due to an high level of contamination of early-type with blue colours at this redshifts.

We confirm the result already found by Cassata et al. (2007) using photometric redshifts in a sub-area of the COSMOS field at $z \sim 0.7$. Analyzing the apparent V-z' colour-magnitude and colour-mass relations they showed how the colour distribution of the two morphological classes are nearly independent on local density. Taking advantage of the higher precision of spectroscopic redshifts we can here use more accurate local densities and can confirm that their findings are not an artifact due to photometric redshift but are real.

7.6 Summary

We have analyzed the build-up of the colour-mass relation with redshift using the dataset provided by the COSMOS/zCOSMOS surveys. Confirming previous find-

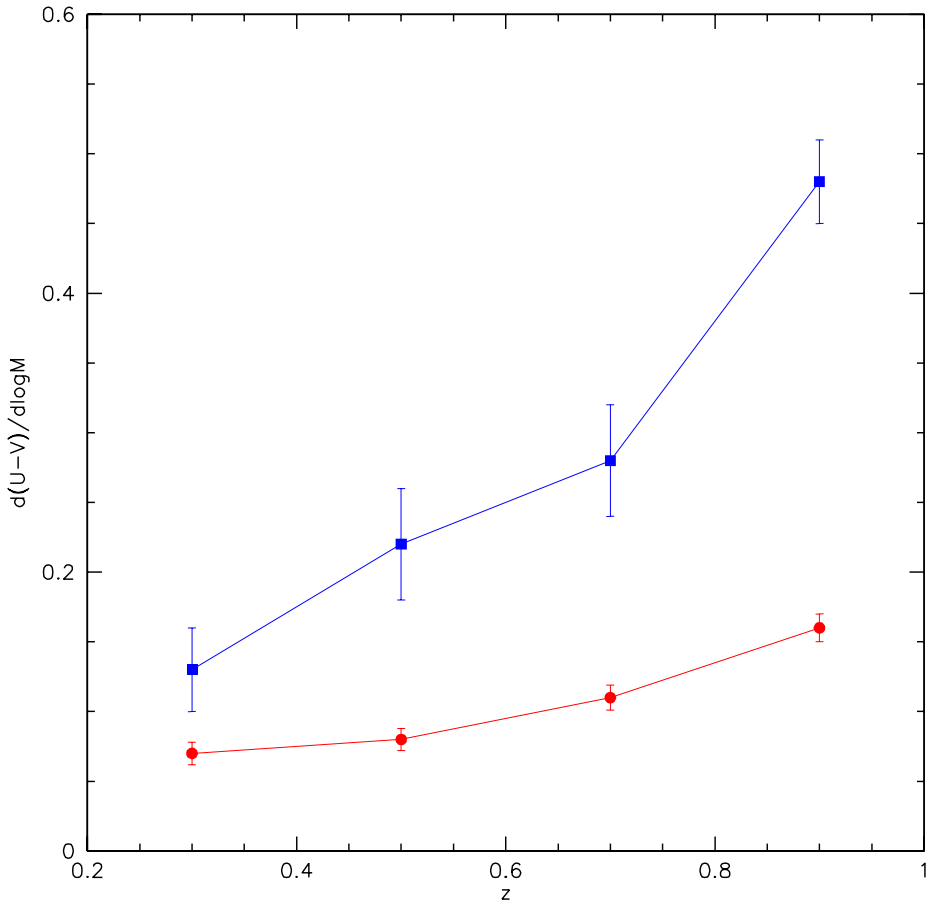

FIGURE 7.9— Evolution of the slope of the BS (blue squares) and RS (red circles) as a function of redshift.

ings, we show that colour bimodality is already in place at $z \sim 1$, with the red sequence and the blue sequence well visible. Nevertheless we observe an evolution of the colour-mass diagram with cosmic time. The faint-end of the red sequence builds up at progressively low redshift. Taking into account incompleteness of the sample and defining faint galaxies having $10.4 < log(M) < 11.1$, and luminous galaxies with $log(M) > 11.1$, we find an evolution of the faint-to-luminous ratio in the redshift range $0.7 - 0.3$. Concerning the blue sequence, analyzing the region of the diagram with the highest density of points, in order to avoid to be biased by incompleteness effects, we find that its slope clearly increases with redshift. We suggest that this effect is due to a differential evolution of blue sequence galaxies with mass, where high-mass galaxies are the first to leave the BS and to reach the RS, according to the observation of the

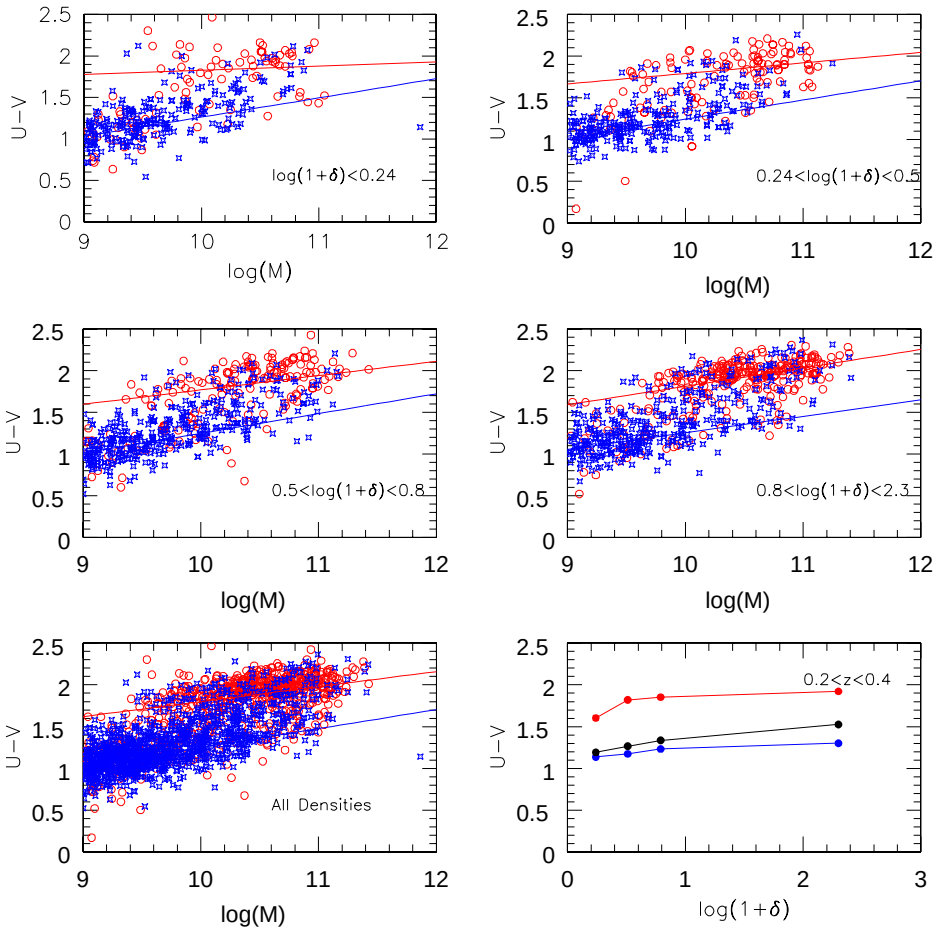

FIGURE 7.10— Colour-mass diagram as a function of density for galaxies in the redshift bin 0.2-0.4. In the first four panels the global population has been divided in quartiles of density, as shown by the labels. In the bottom-left panel the colour-mass diagram for all the galaxies in this redshift bin is reported. In the bottom-right panel the median colour of all galaxies (black), early-type (red) and late-type (blue) is plotted as a function of overdensity. Solid lines represent the least square fit to the two sequences.

population of the faint red sequence at low redshift.

We also exploited zCOSMOS data to study the effect of the environment on the colour-mass relation. Thanks to the high-precision redshift measurements, environment can be traced with high precision through a local density estimator. We find that, as density increases, red sequence is more and more populated, but apart from that the other features of colour-mass relation are nearly unvaried, in particular the median colour of the early and late type populations, which trace respectively the red and the blue sequence population, does not change with environment.

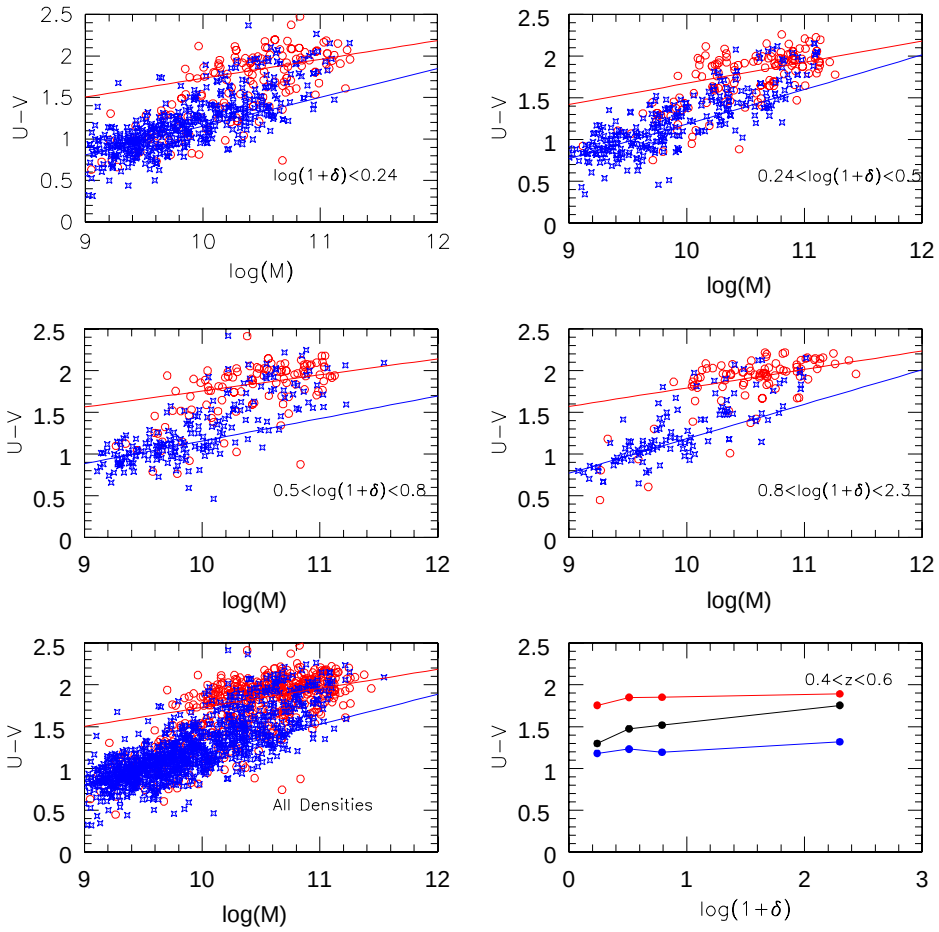

FIGURE 7.11— The same as in Figure 7.11 but for the redshift bin 0.4-0.6.

The galaxy colour bimodality constitutes a further powerful test for hierarchical models of galaxy formation, as it points to the existence of two different classes of galaxies, presumably originated and evolved in a very different way and in different cosmic epochs. Some of the semi-analytical models existing in literature results to be in good agreement with the colour bimodality observed at low and intermediate redshift (Menci et al. 2006; Menci et al. 2008), demonstrating how this feature of galaxy evolution can be taken into account and explained even in hierarchical models.

In this Thesis, we have already demonstrated in the previous chapters, that our semi-analytical model of galaxy formation is able to reproduce in a natural way the different evolutionary paths followed by galaxies with different mass. We tested this analyzing the SFHs of galaxies residing in haloes with different mass, showing that galaxies in the most massive haloes, that actually are the most massive galaxies, formed their

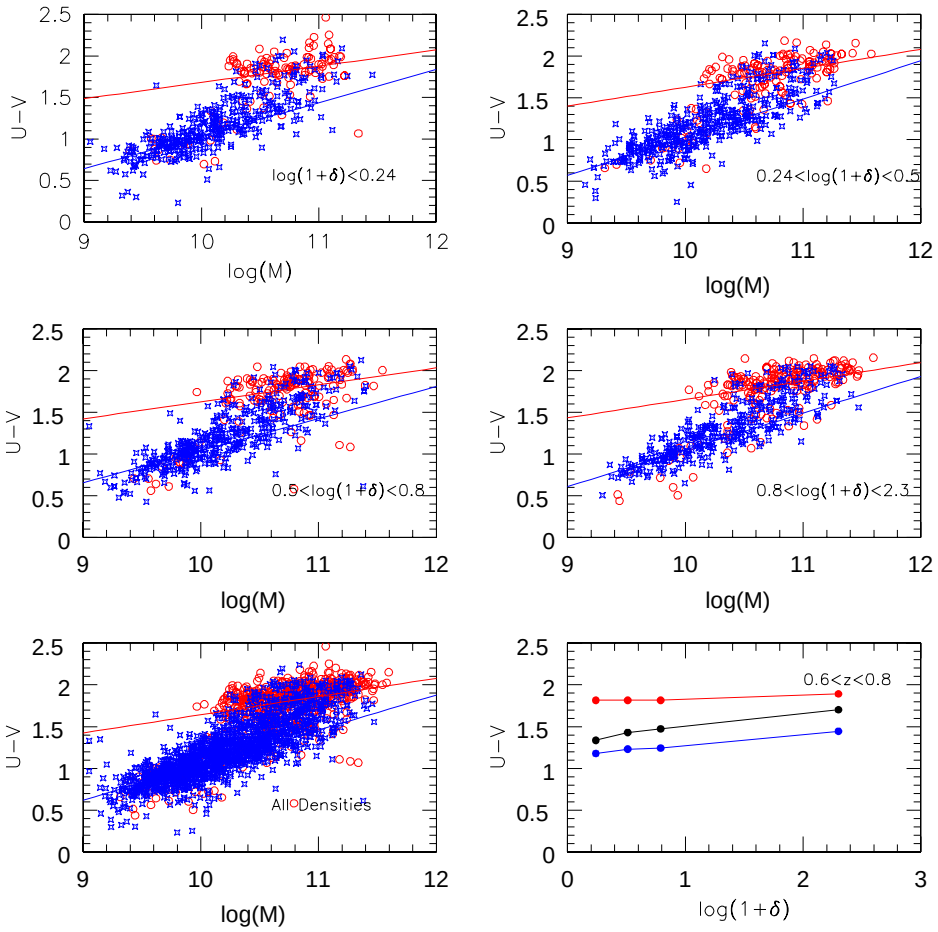

FIGURE 7.12— The same as in Figure 7.10 but for the redshift bin 0.6-0.8.

stars on shorter timescales at higher redshift. Since colour traces the ratio between the past star formation history of a given galaxy and its present stellar mass, these systems should be even redder than low-mass systems, belonging to the RS. In fact, it is now clear that in galaxies living in the RS, star formation has been quenched (Bower et al. 1998; Blanton et al. 2006) and in order to stay there the star formation rate must keep low. On the contrary, the BS is made by an eterogeneous mix of galaxies, showing a wider range of SFR, metallicities and dust content.

By the light of the results obtained with our semi-analytic model, we can attempt a first qualitatively interpretation of the existence of the bimodality here observed. The most massive galaxies that we find nowadays, has formed and assembled the bulk of their stars at high redshift ($z > 2$), when the cooling was more efficient and mergers very frequent. The early exhaustion of cold gas in these systems and the subsequent

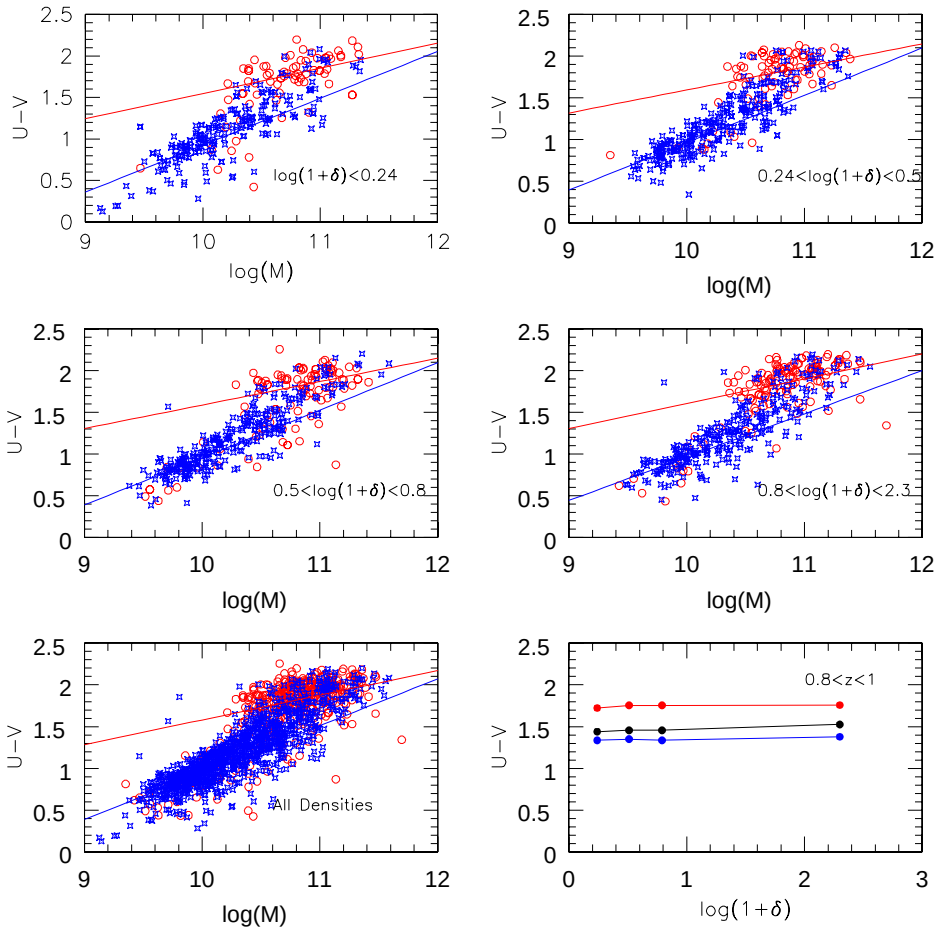

FIGURE 7.13— The same as in Figure 7.10 but for the redshift bin 0.8-1.

decrease in the star formation rate lead them to move quite soon from the BS to the RS and evolve passively hereafter. Objects with progressive low stellar mass move to the RS at later cosmic times, with the consequence of populating the faint-end of the RS at low redshift and to depauperate the high-mass end of the BS. For these reasons, we expect our model to reproduce qualitatively the existence of the colour segregation in the colour-mass diagram, and to recover the build-up of the faint-end of the RS. In the next future, we will proceed to interface the code to a spectro-photometric synthesis model in order to get galaxy colours and make a quantitative comparison between the model and the data here presented. This will constitute a strong constraint on the epoch of galaxy assembly to our modelled galaxies and to the relative role of the different mechanisms of star formation and feedback involved. Moreover, it will be extremely interesting to try to compare the evolution of the BS slope observed in COSMOS with

the model, in order to understand, from a theoretical point of view, the origin of such feature.

8

Conclusions and Future Work

8.1 Summary and Conclusions

In this Thesis we addressed different theoretical and observational aspects related to the galaxy formation process, mainly focusing on the epochs of mass assembly and star formation. On one side we faced the problem from a theoretical point of view, with the development of a new semi-analytic model of galaxy formation (GECO, Galaxy Evolution COde), which couples a Monte Carlo representation of the merging hierarchy of DM haloes with analytical prescriptions for the physics of baryons. On the observational side, we exploit the COSMOS dataset, in order to address another major issue of galaxy properties, that is the colour distribution of galaxies, with the twofold aim to deeply understand galaxy evolution and to set new constraints to hierarchical models of galaxy formation, that we want to reproduce with GECO in the next future.

We start in Chapter 1 with an overview of the observations that shape our understanding of how galaxies formed and assembled their mass through cosmic time. We focus on that observational results that we tried to interpret and reproduce in this Thesis from a theoretical point of view in the following Chapters. We discuss recent findings on the determination of both local and high-redshift stellar mass function, since our model is set to reproduce the galaxy stellar mass content at $z = 0$. Several finding are discussed in the context of the "downsizing" scenario of galaxy formation, according to which the formation epoch of a galaxy anti-correlates with its stellar mass. One of the aim of the Thesis was to demonstrate that this observational feature is indeed intrinsic, even if counter intuitive, in hierarchical models of galaxy formation, although it is difficult to reproduce from a quantitative side. A further issue discussed is the observed colour bimodality, namely the segregation of galaxies in two regions in the colour-magnitude (or colour-mass) plane, with a red and blue sequences well separated. Since colour measures the ratio of the present star formation rate over the total stellar mass in a given galaxy, it is one of the most challenge feature to be reproduced in semi-analytical model of galaxy formation, and this will constitute our goal for the future.

In order to set the basis upon which our model is based, in Chapter 2 we describe the cosmological background and the current vision of the universe and its matter content, as depicted, in particular, by recent determinations from CMB observations. The framework of the hierarchical growth of structure is presented, both in the linear and non-linear regime. Hence, the powerful formalism of the the PS and EPS theories is analysed, since it constitutes the basis of our Monte Carlo approach for building the merging hierarchy of dark matter haloes.

Indeed, in Chapter 3, we describe how to build a Monte Carlo merger tree. Our algorithm for splitting haloes in progenitors is based on the approach proposed by Sheth & Lemson (1999), but developed in a independent way and extended to the ΛCDM power-spectrum. It is also improved to take into account different shapes of the barrier, which parametrise the spherical and the ellipsoidal collapse models. As a check for the full consistency of the algorithm, the mean statistical quantities, such as the conditional and unconditional mass function, are recovered and compared with the theoretical expectations. In the case of the spherical collapse the comparison shows that our model is fully consistent with the EPS predictions. Some discrepancies in the conditional mass function at low redshift in the ellipsoidal model do exist, but they are not relevant when the global mass function is computed. Finally, we show a comparison between theoretical, Monte Carlo and N-body estimates for the conditional mass function, confirming the high level of agreement between the ellipsoidal collapse model and the N-body estimates. In order to implement the semi-analytical model, we make use of the classical spherical collapse model, but we plan to implement it even on the ellipsoidal case, which constitutes a valid alternative to N-body simulations.

The semi-analytic part of the model is described in Chapter 4, where the Galaxy Evolution COde (GECO) is introduced. At variance with the backward approach exploited for generating the merging hierarchy of the haloes, galaxy formation is modelled forwards in time, starting from the "leaves" of the tree. Baryons are put inside these haloes, according to the baryonic fraction observed, and then they are subject to dissipative processes. At the beginning, gas is assumed to be shocked and heated to the virial temperature of the halo. Subsequently, it can cool through radiative processes and accrete towards the centre of the halo. The cooling rate depend upon the virial temperature of the gas (and hence on the halo mass) and on the metallicity of the gas, that is here assumed to be constant and equal to one third of the solar one. Once gas has cooled, it becomes available to form stars. We allow star formation to occur in two ways. The most obvious way is in a quiescent mode, that continue as far as cold gas is available. The second mechanism is through starbursts that are triggered only during galaxy mergers (both minor and major, but with different efficiencies), and allow a much more efficient conversion of gas in stars. In order to regulate the star formation process, different kind of feedback are considered. On low-mass haloes, the feedback from photoionization and that from SN explosions, inhibits the star formation. On the other side, star formation in massive systems is regulated by the AGN feedback. This is modelled with a radio mode of feedback, that acts on the quiescent star formation, and a QSO mode, highly effective in reducing the efficiency of starbursts. Finally,

mergers between galaxies are allowed to occur. Dynamical friction drives the interaction between satellite galaxies and the central one, while random collisions occur among satellites. Both kind of mergers in our model lead to a starburst.

At variance with other models of galaxy formation, we tested our results directly on the observables involving stellar mass more then luminosities. Stellar masses are indeed the most direct outcome of the model, hence the uncertainties due to the spectrophotometric synthesis, dust extinction and Initial Mass Function can be avoided. Therefore, in Chapter 5 we present the results of the model, starting from the zero-redshift comparison. The free parameters introduced in the model, which set the efficiency of the star formation processes and that of feedback, from SN and AGN, are adjusted demanding a good match of the local stellar mass function. Therefore, GECO predicts the correct number of galaxies in each bin of masses at z=0. In particular, we set the model in order to have galaxies correctly distributed among early and late types, that imposes strong constraints on the relative balance between the quiescent and starburst mode of star formation. As a further check, we verify that the relation between the bulge and the black-hole mass is well reproduced, in order to avoid unrealistic large values for the AGN efficiencies. Even at high-redshift our modelled galaxies evolve in nice agreement with observations. We focus on two drivers of galaxy formation: the star formation process and the mass assembly. The integrated star formation rate density results in good agreement with that observed, with an high level of star formation at high redshift, a peak at $z \sim 1.5 - 3$ and then a sharp decline, although less evident than that indicated by the most recent observations. Even mass assembly, as indicated by the evolution of the stellar mass density, is predicted to be faster at high redshift, and to slow down at recent epochs. Nevertheless, the ratio between the evolution of the faint-end and the bright-end of the stellar mass function is not fairly reproduced. In fact, while the bright-end evolves too much, the faint-end is already in place at high redshift. On the contrary, different set of observations indicate a large increase in the number density of low-mass objects between $z \sim 3.5$ and the present-day and a lower rate of evolution for massive objects. Nevertheless, it is hard to try firm conclusions about the epoch of galaxy assembly even from observations. Our comparison with different set of data shows that some discrepancies among them exist, mainly at high redshift, where uncertainties in mass and redshift determinations are quite large. An other interesting feature nicely reproduced in the model is the “downsizing” nature of galaxy formation. Analysing in detail the Star Formation History (SFH) galaxy by galaxy, we found that the epoch of major activity in star formation for massive systems is always earlier than their smaller counterpart. Even the assembly epoch of massive systems, as indicated by their assembly redshift, is on average larger than for low-mass objects, although the trend is less clear then in the case of the formation redshift. Indeed, in hierarchical models of galaxy formation, the most massive systems nowadays were formed from the assembly of several progenitors, that at high redshift collapsed from the highest density peaks of the primordial density field. Therefore, they started to form stars early, in a period when both the cooling efficiency and the frequency of mergers were high, leading to a fast consumption of cold gas.

In order to get a deeper insight on how the model works, in Chapter 6 we present different tests made on GECO, with a slight variations from the fiducial model, described in the previous Chapter. The aim of such test was twofold. First, we aim to understand the effect of the free parameters and the robustness of the results obtained. Secondly, we wanted to understand the physical reasons of our findings. For each model, we compare the local stellar mass function with the fiducial model. This turned out to be influenced at the bright-end mainly by the value of the efficiency of the quiescent star formation and by the presence of the feedback from AGN. On the faint-end side, the feedback from SN acts to flatten the slope. The inclusion of starburst episodes determines the relative contribution of bulges and disks to the total mass function. The evolutionary paths of galaxies found in the fiducial model is roughly reproduced in all the other models, although in some cases the evolution turns out to be speed up at higher redshift, such as in the case of enhanced star formation efficiency, and in other cases slowed down, as in the suppression of starbursts. Even "downsizing" is recovered in all the models explored, showing that is not due to the introduction of some particular form of feedback, but is intrinsic in the approach.

Finally, in Chapter 7, we addresses a different issue on galaxy evolution, from an observational point of view. We exploit the unique dataset provided by the COSMOS/zCOSMOS survey, in order to study the build-up of the colour bimodality relation with redshift and environment. A red and a blue sequence are well visible up to the highest redshift probed, namely $z \sim 1$. Nevertheless, some changes in the colour distribution of galaxies with redshift are observed. The faint-end of the red sequence appears to be increasingly populated as cosmic time increases. Simultaneously, the blue sequence slope flattens at low redshift. We interpret this findings in terms of a differential evolution of galaxies with stellar mass. High-mass galaxies are the first to leave the BS and to move to the RS, depauperating the high-mass end of the BS and populating the RS at progressively lower masses. Moreover, the high precision spectroscopic data for a subsample of COSMOS galaxies, within the zCOSMOS project, allow us to study this processes as a function of the environment where they live. We found that the properties of RS and BS are almost unchanged between different environments, at least for $z \sim 1$, that is the highest redshift probed here. Anyway at increasingly high density environments, the RS becomes more populated with respect to the BS. A challenge goal for the future will be to understand if our semi-analytical model, which achieved a lot of success in matching different galaxy properties, is capable to capture the features observed in the galaxy colour distributions and its evolution.

8.2 Future Work

As demonstrated in this Thesis, semi-analytical models of galaxy formation are a powerful tool to investigate how galaxies formed and evolved. Here we tried a first comparison with those observations that involve stellar mass, that is a direct output of the code. The most natural extension of the code is to interface it with a spectro-photometric synthesis model, in order to get luminosities at different wavelenghts. The

first obvious exploitation of this information will be to recover the optical colour distribution of galaxies, in order to try to reproduce the colour bimodality of galaxies at low and intermediate redshift, as we observed in COSMOS. The major uncertainty in this procedure will be the treatment of dust. In particular, we aim to model in detail not only dust absorption, but also the riemission of dust, that affects the Spectral Energy Distribution at long wavelenghts. This will allow us to make several comparisons with far-IR data.

A second way of investigation will be towards a full understanding of the influence of the underlying dark matter on galaxy evolution. In particular, since we have used different kinds of merger trees, both Monte Carlo and numerical, the next step will be to understand how galaxy properties change if different paths for the merging hierarchy of haloes are assumed. Hence, we want to understand if spherical and ellipsoidal collapse lead to the same conclusions about galaxy evolution, and if it is possible to discriminate among them. Moreover, we plan to interface GECO even to N-body simulations and to analyse the differences between the MC and the numerical method. This last approach will give us the information about the spatial distribution of galaxies, which will allow to study even the clustering properties of galaxies.

List of Figures

Bibliography

Baldry I. K., Balogh M. L., Bower R. G., Glazebrook K., Nichol R. C., Bamford S. P., Budavari T., 2006, MNRAS, 373, 469

Baldry I. K., Glazebrook K., Driver S. P., 2008, arXiv, 804, arXiv:0804.2892

Baldry I. K., Glazebrook K., Brinkmann J., Ivezić Ž., Lupton R. H., Nichol R. C., Szalay A. S., 2004, ApJ, 600, 681

Balogh M. L., Baldry I. K., Nichol R., Miller C., Bower R., Glazebrook K., 2004, ApJ, 615, L101

Baugh C. M., Cole S., Frenk C. S., 1996, MNRAS, 283, 1361

Baugh C. M., Cole S., Frenk C. S., Lacey C. G., 1998, ApJ, 498, 504

Bell E. F., McIntosh D. H., Gyory Z., Trujillo I., Katz N., Weinberg M. D., 2004, AAS, 36, 678

Bell E. F., de Jong R. S., 2000, MNRAS, 312, 497

Bell E. F., McIntosh D. H., Katz N., Weinberg M. D., 2003, ApJS, 149, 289

Bell E. F., et al., 2004, ApJ, 608, 752

Benson A. J., Frenk C. S., Baugh C. M., Cole S., Lacey C. G., 2003, MNRAS, 343, 679

Benson A. J., Frenk C. S., Lacey C. G., Baugh C. M., Cole S., 2002, MNRAS, 333, 177

Benson A. J., Lacey C. G., Baugh C. M., Cole S., Frenk C. S., 2002, MNRAS, 333, 156

Benson A. J., Pearce F. R., Frenk C. S., Baugh C. M., Jenkins A., 2001, MNRAS, 320, 261

Berta S., et al., 2007, A&A, 476, 151

Bertone S., Stoehr F., White S. D. M., 2005, MNRAS, 359, 1201

Bertschinger E., 1989, ApJ, 340, 666

Binney J., Tremaine S., 1987, gady.book,

Blanton M. R., et al., 2001, AJ, 121, 2358

Bolzonella et al. 2008, in preparation

Bond J. R., Cole S., Efstathiou G., Kaiser N., 1991, ApJ, 379, 440

Bond J. R., Efstathiou G., 1984, ApJ, 285, L45

Bond J. R., Myers S. T., 1996, ApJS, 103, 1

Bond J. R., Myers S. T., 1996, ApJS, 103, 63

Bond J. R., Myers S. T., 1996, ApJS, 103, 41

Bondi H., 1952, MNRAS, 112, 195

Borel E., 1944, C&T, 60, 130

Bosma A., 1981, AJ, 86, 1791

Bosma A., 1981, AJ, 86, 1825

Bower R. G., Benson A. J., Malbon R., Helly J. C., Frenk C. S., Baugh C. M., Cole S., Lacey C. G., 2006, MNRAS, 370, 645

Boylan-Kolchin M., Ma C.-P., 2007, MNRAS, 374, 1227

Bozzetti et al. 2008, in preparation

Bundy K., Ellis R. S., Conselice C. J., 2005, ApJ, 625, 621

Bundy K., et al., 2006, ApJ, 651, 120

Capak P., et al., 2007, ApJS, 172, 99

Carroll S. M., Press W. H., Turner E. L., 1992, ARA&A, 30, 499

Cassata P., et al., 2007, ApJS, 172, 270

Cavaliere A., Colafrancesco S., Menci N., 1992, ApJ, 392, 41

Chandrasekhar S., 1943, ApJ, 97, 255

Cimatti A., Daddi E., Renzini A., 2006, A&A, 453, L29

Cimatti A., et al., 2004, Natur, 430, 184

Cole S., Aragon-Salamanca A., Frenk C. S., Navarro J. F., Zepf S. E., 1994, MNRAS, 271, 781

Cole S., Benson A., Baugh C., Lacey C., Frenk C., 2000, ASPC, 200, 109

Cole S., 1991, ApJ, 367, 45

Cole S., Kaiser N., 1989, MNRAS, 237, 1127

Cole S., Lacey C., 1996, MNRAS, 281, 716

Cole S., Lacey C. G., Baugh C. M., Frenk C. S., 2000, MNRAS, 319, 168

Cole S., et al., 2001, MNRAS, 326, 255

Cowie L. L., Songaila A., Hu E. M., Cohen J. G., 1996, AJ, 112, 839

Croton D., 2007, AAS, 211, #125.04

Croton D. J., et al., 2006, MNRAS, 365, 11

Daddi E., Cimatti A., Renzini A., Fontana A., Mignoli M., Pozzetti L., Tozzi P., Zamorani G., 2004, ApJ, 617, 746

De Lucia G., Kauffmann G., Springel V., White S. D. M., Lanzoni B., Stoehr F., Tormen G., Yoshida N., 2004, MNRAS, 348, 333

De Lucia G., et al., 2004, ApJ, 610, L77

De Lucia G., et al., 2007, MNRAS, 374, 809

De Lucia G., Springel V., White S. D. M., Croton D., Kauffmann G., 2006, MNRAS, 366, 499

Dekel A., Silk J., 1986, ApJ, 303, 39

Dressler A., 1980, ApJ, 236, 351

Drory N., Salvato M., Gabasch A., Bender R., Hopp U., Feulner G., Pannella M., 2005, ApJ, 619, L131

Efstathiou G., Frenk C. S., White S. D. M., Davis M., 1988, MNRAS, 235, 715

Eggen O. J., Lynden-Bell D., Sandage A. R., 1962, ApJ, 136, 748

Elmegreen B. G., Scalo J., 2004, ARA&A, 42, 211

Fan X., et al., 2000, AJ, 120, 1167

Ferrarese L., Merritt D., 2000, ApJ, 539, L9

Fontana A., et al., 2004, A&A, 424, 23

Fontana A., et al., 2006, A&A, 459, 745

Franceschini A., et al., 2006, A&A, 453, 397

Franceschini A., Silva L., Fasano G., Granato G. L., Bressan A., Arnouts S., Danese L., 1998, ApJ, 506, 600

Franx M., et al., 2003, ApJ, 587, L79

Franzetti P., Scodeggio M., Maccagni D., Garilli B., the VVDS collaboration, 2006, MSAIS, 9, 297

Frenk C. S., et al., 1999, ApJ, 525, 554

Gao L., De Lucia G., White S. D. M., Jenkins A., 2004, MNRAS, 352, L1

Gao L., White S. D. M., Jenkins A., Stoehr F., Springel V., 2004, MNRAS, 355, 819

Garilli B., et al., 2008, A&A, 486, 683

Gavazzi G., Scodeggio M., 1996, A&A, 312, L29

Gebhardt K., et al., 2000, ApJ, 539, L13

Giallongo E., Menci N., Poli F., D'Odorico S., Fontana A., 2000, ApJ, 530, L73

Giocoli C., Tormen G., van den Bosch F. C., 2008, MNRAS, 386, 2135

Gunn J. E., Gott J. R. I., 1972, ApJ, 176, 1

Guzzo L., et al., 2008, Natur, 451, 541

Häring N., Rix H.-W., 2004, ApJ, 604, L89

Hatton S., Devriendt J. E. G., Ninin S., Bouchet F. R., Guiderdoni B., Vibert D., 2003, MNRAS, 343, 75

Helly J. C., Cole S., Frenk C. S., Baugh C. M., Benson A., Lacey C., Pearce F. R., 2003, MNRAS, 338, 913

Hogg D. W., et al., 2002, AJ, 124, 646

Hopkins A. M., 2004, ApJ, 615, 209

Hubble E. P., 1936, RNeb,

Jenkins A., Frenk C. S., White S. D. M., Colberg J. M., Cole S., Evrard A. E., Couchman H. M. P., Yoshida N., 2001, MNRAS, 321, 372

Jiang C. Y., Jing Y. P., Faltenbacher A., Lin W. P., Li C., 2008, ApJ, 675, 1095

Juszkiewicz R., Sonoda D. H., Barrow J. D., 1984, MNRAS, 209, 139

Kauffmann G., White S. D. M., 1993, MNRAS, 261, 921

Kauffmann G., White S. D. M., Guiderdoni B., 1993, MNRAS, 264, 201

Kauffmann G., Colberg J. M., Diaferio A., White S. D. M., 1999, MNRAS, 307, 529

Kauffmann G., Colberg J. M., Diaferio A., White S. D. M., 1999, MNRAS, 303, 188

Kauffmann G., Haehnelt M., 2000, MNRAS, 311, 576

Kauffmann G., et al., 2003, MNRAS, 341, 54

Kennicutt R. C., Jr., 1998, ApJ, 498, 541

Kereš D., Katz N., Weinberg D. H., Davé R., 2005, MNRAS, 363, 2

Kibble T. W. B., Turok N. G., 1986, RSPTA, 320, 565

Kodama T., Arimoto N., 1997, A&A, 320, 41

Kodama T., Arimoto N., Barger A. J., Arag'on-Salamanca A., 1998, A&A, 334, 99

Kolb E. W., Turner M. S., 1990, eaun.book,

Kovac et al. 2008, in preparation

Koyama Y., Kodama T., Tanaka M., Shimasaku K., Okamura S., 2007, MNRAS, 382, 1719

Lacey C., Cole S., 1994, MNRAS, 271, 676

Lacey C., Cole S., 1993, MNRAS, 262, 627

Larson R. B., 1975, IAUS, 69, 247

Lilly S. J., et al., 2007, ApJS, 172, 70

Lilly S. J., Le Fevre O., Hammer F., Crampton D., 1996, ApJ, 460, L1

Madau P., Ferguson H. C., Dickinson M. E., Giavalisco M., Steidel C. C., Fruchter A., 1996, MNRAS, 283, 1388

Madau P., Pozzetti L., 2000, MNRAS, 312, L9

Madgwick D. S., et al., 2003, ApJ, 599, 997

Madgwick D. S., et al., 2002, MNRAS, 333, 133

Mamon G. A., 1992, ApJ, 401, L3

Mandelbaum R., Tasitsiomi A., Seljak U., Kravtsov A. V., Wechsler R. H., 2005, MNRAS, 362, 1451

Martin C. L., 1999, ApJ, 513, 156

Menci N., Cavaliere A., Fontana A., Giallongo E., Poli F., Vittorini V., 2004, ApJ, 604, 12

Menci N., Fontana A., Giallongo E., Salimbeni S., 2005, ApJ, 632, 49

Menci N., Cavaliere A., 2002, ASPC, 253, 429

Meneux B., Heinis S., Le Fèvre O., Milliard B., Guzzo L., Arnouts S., Pollo A., 2007, ASPC, 379, 318

Mihos J. C., Hernquist L., 1996, ApJ, 464, 641

Mihos J. C., Hernquist L., 1994, ApJ, 425, L13

Mo H. J., Mao S., White S. D. M., 1998, MNRAS, 295, 319

Mobasher B., et al., 2007, ApJS, 172, 117

Navarro J. F., Frenk C. S., White S. D. M., 1995, MNRAS, 275, 56

Neistein E., van den Bosch F. C., Dekel A., 2006, MNRAS, 372, 933

Netterfield C. B., et al., 2002, ApJ, 571, 604

Ostriker J. P., Peebles P. J. E., Yahil A., 1974, ApJ, 193, L1

Pérez-González P. G., et al., 2008, ApJ, 675, 234

Peebles P. J. E., 1993, ppc..book,

Peebles P. J. E., 1980, lssu.book,

Perlmutter S., Turner M. S., White M., 1999, PhRvL, 83, 670

Press W. H., Schechter P., 1974, ApJ, 187, 425

Renzini A., 2006, ARA&A, 44, 141

Riess A. G., et al., 1998, AJ, 116, 1009

Rodighiero et al. 2008, in preparation

Roos N., Norman C. A., 1979, A&A, 76, 75

Rubin V. C., Ford W. K. J., . Thonnard N., 1980, ApJ, 238, 471

Sanders D. B., Mirabel I. F., 1996, ARA&A, 34, 749

Scarlata C., et al., 2007, ApJS, 172, 406

Scodeggio M., et al., 2005, PASP, 117, 1284

Scoville N., et al., 2007, ApJS, 172, 1

Sheth R. K., 1995, MNRAS, 276, 796

Sheth R. K., 1996, MNRAS, 281, 1277

Sheth R. K., Lemson G., 1999, MNRAS, 305, 946

Sheth R. K., Mo H. J., Tormen G., 2001, MNRAS, 323, 1

Sheth R. K., Tormen G., 2002, MNRAS, 329, 61

Silk J., 1968, Natur, 218, 453

Somerville R. S., 2001, ASPC, 230, 477

Somerville R. S., Kolatt T. S., 1999, MNRAS, 305, 1

Somerville R. S., Primack J. R., 1999, MNRAS, 310, 1087

Spergel D. N., et al., 2007, ApJS, 170, 377

Springel V., Yoshida N., White S. D. M., 2001, NewA, 6, 79

Steidel C. C., Shapley A. E., Pettini M., Adelberger K. L., Erb D. K., Reddy N. A., Hunt M. P., 2004, ApJ, 604, 534

Strateva I., et al., 2001, AJ, 122, 1861

Sutherland R. S., Dopita M. A., 1993, ApJS, 88, 253

Tasca et al. 2008, in preparation

Tanaka M., Kodama T., Arimoto N., Okamura S., Umetsu K., Shimasaku K., Tanaka I., Yamada T., 2005, MNRAS, 362, 268

Thomas D., Maraston C., Bender R., Mendes de Oliveira C., 2005, ApJ, 621, 673

Toomre A., Toomre J., 1972, BAAS, 4, 214

Toomre A., 1977, egsp.conf, 401

Tormen G., 1997, MNRAS, 290, 411

Trujillo I., Conselice C. J., Bundy K., Cooper M. C., Eisenhardt P., Ellis R. S., 2007, MNRAS, 382, 109

Tully R. B., Mould J. R., Aaronson M., 1982, ApJ, 257, 527

Warren M. S., Quinn P. J., Salmon J. K., Zurek W. H., 1992, ApJ, 399, 405

West M. J., Dekel A., Oemler A. J., 1987, ApJ, 316, 1

White S. D. M., Efstathiou G., Frenk C. S., 1993, MNRAS, 262, 1023

White S. D. M., Rees M. J., 1978, MNRAS, 183, 341

White S. D. M., Frenk C. S., 1991, ApJ, 379, 52

Yoshida N., Stoehr F., Springel V., White S. D. M., 2002, MNRAS, 335, 762

Zel'Dovich Y. B., 1970, A&A, 5, 84

Zentner A. R., 2006, EAS, 20, 41

Zhang J., Ma C.-P., Fakhouri O., 2008, MNRAS, 387, L13

Zwicky F., 1933, AcHPh, 6, 110